Science
AAAS

Supplementary Materials for

Dealuminated Beta zeolite reverses Ostwald ripening for durable copper nanoparticle catalysts

Lujie Liu *et al*.

Corresponding authors: Jiabi Ma, majiabi@bit.edu.cn; Xiaoming Cao, xmcao@ecust.edu.cn; Liang Wang, liangwang@zju.edu.cn; Feng-Shou Xiao, fsxiao@zju.edu.cn

Science **383**, 94 (2024)
DOI: 10.1126/science.adj1962

The PDF file includes:

Materials and methods

Dimethyl oxalate (98%, Aladdin); $Cu(NO_3)_2 \cdot 3H_2O$ (98%, Sinopharm Chemical Reagent Co., Ltd.); $NH_3 \cdot H_2O$ (25.0–28.0%, Sinopharm Chemical Reagent Co., Ltd.); HNO_3 (65–68 wt%, Yonghua Chemical Co., Ltd.); methanol (≥99.5%, Sinopharm Chemical Reagent Co., Ltd.); ethanol (≥99.7%, Sinopharm Chemical Reagent Co., Ltd.); ethylene glycol (>99%, Aladdin); 1,4-dioxane (≥99.5%, Sinopharm Chemical Reagent Co., Ltd., internal standard); paraformaldehyde (95%, Aladdin); silica sol (40 wt%, Sigma-Aldrich); H_2 (99.999%), CO (99.99%), and N_2 (99.999%) supplied by Hangzhou Jingong special gas Co. Ltd.; ZSM-5 (Si/Al ratio at 13–18, atomic ratio, Zhuoran Environmental Protection (Dalian) Co., Ltd.); Silicalite-1 (denoted as S-1, Nankai University Catalyst Co., Ltd.); Beta (Si/Al ratio at 13, atomic ratio, Nankai University Catalyst Co., Ltd.); CuO powder (average size of 40 nm, 99.5%, Macklin); CeO_2 (average size of 20–50 nm, 99.5%, Aladdin). Tetraethyl orthosilicate (TEOS), tetrapropylammonium hydroxide (TPAOH, 40 wt%), and diethoxydimethylsilane (DEMS) were obtained from Shanghai Cairui Chemical Technology Co. Ltd. Sodium aluminate ($NaAlO_2$) was obtained from Sino-Pharm Chemical Reagent Co. Ltd.

Catalyst preparation

Synthesis of dealuminated Beta zeolite (Beta-deAl)

The dealumination of commercial Beta zeolite was performed through a classical route (*50, 51*). 3.0 g of commercial Beta zeolite (Si/Al ratio at 13) was dispersed in 150 mL of aqueous nitric acid solution (13 M) under stirring at 80°C. After stirring for 12 h, the mixture was cooled to room temperature, and the solid was separated by filtrating and washing with a large amount of deionized water until pH of the filtrate at 7.0. By inductively-coupled plasma (ICP) analysis with a Perkin-Elmer 3300DV emission spectrometer, the atomic ratio of Si/Al of the Beta-deAl was ~1250. The Beta-deAl employed in this work was the one with Si/Al ratio at 1250 unless noted.

Synthesis of Cu/Beta-deAl

As a typical run for the synthesis of the Cu/Beta-deAl with Cu content at 3.0 wt%. 0.23 g of $Cu(NO_3)_2 \cdot 3H_2O$ was dissolved in aqueous ammonia solution (0.75 g of $NH_3 \cdot H_2O$ diluted with 100 mL of deionized water). After stirring for 10 min, 1.94 g of the Beta-deAl support was added into the solution, and stirred vigorously at 80°C for another 6 h. Then, the sample was filtrated, dried at 100°C overnight, and calcined at 400°C for 3 h with a heating rate of 1°C/min to obtain the catalyst. Before the catalytic tests, the Cu/Beta-deAl sample was pre-reduced with hydrogen at 400°C for 3 hours. The Cu/Beta-deAl catalyst with Cu content at 20 wt% was prepared by the same procedures except using 1.52 g of $Cu(NO_3)_2 \cdot 3H_2O$, 5.00 g of $NH_3 \cdot H_2O$, and 1.60 g of Beta-deAl support. The Cu/Beta-deAl in this manuscript was the sample with Cu content at 3.0 wt% unless specially noted (e.g. Cu/Beta-deAl-18% with Cu loading content at 18 wt%).

Synthesis of hydroxyl-modified S-1 and ZSM-5 and siliceous Beta zeolite

Hydroxyl-modified S-1 zeolite (S-1-OH) was synthesized using DEMS and TEOS as silica sources (*52*). As a typical run, 80 mL of ethanol was added to 100 mL of a water solution containing 6 mL of aqueous ammonia under stirring. Then, 3.75 g of TEOS and 0.30 g of DEMS were added, stirring at room temperature for another 8 h. After distilling under a vacuum to remove water and ethanol and drying at 100°C for 12 h, the solid powder of amorphous silica modified with methyl groups (SiO_2-Me) was obtained. After grinding 0.5 g of TPAOH and 0.6 g of SiO_2-Me at room temperature for 10 min, the mixture was transferred into an autoclave for solvent-free

crystallization at 180°C for 72 h to give the methyl-modified S-1 zeolite (*53*). After calcination at 550°C in air for 4 h, the methyl groups in the zeolite were transformed into hydroxyl groups, which was denoted as S-1-OH. Similarly, ZSM-5-OH was synthesized from similar procedures except for addition of 0.082 g of $NaAlO_2$ in the solvent-free crystallization. The siliceous Beta zeolite (Beta-Si) was resulted from direct synthesis rather than dealumination of aluminosilicate Beta zeolite.

Synthesis of Cu/S-1, Cu/ZSM-5, Cu/S-1-OH, Cu/ZSM-5-OH, and Cu/Beta

These zeolite-based catalysts were synthesized from very similar procedures of the Cu/Beta-deAl except for using commercial zeolites of S-1, ZSM-5, and Beta and self-prepared zeolites of S-1-OH, ZSM-5-OH, and Beta-Si as supports.

Synthesis of Cu/SiO_2

The Cu/SiO_2 catalyst with Cu content at 3 wt% was prepared from the method reported by Ma and co-workers (*29*). As a typical run, 0.57 g of $Cu(NO_3)_2{\cdot}3H_2O$ was dissolved in aqueous ammonia solution (10 g of $NH_3{\cdot}H_2O$ diluted with 120 mL of deionized water) and stirred for 10 min, followed by the addition of 12.12 g of silica sol. After stirring for 6 h at room temperature, the mixture was heated to 80°C and aged for 2 h to evaporate the excess ammonia. Then, the mixture was transferred into a reactor and hydrothermally aged at 200°C for 12 h. After filtrating, washing with water, drying at 100°C overnight, and calcining at 400°C for 4 h, the Cu/SiO_2 catalyst was obtained. It was pre-reduced with hydrogen at 400°C for 3 h before the catalytic tests in DMO hydrogenation. ICP results suggest that the Cu content on SiO_2 or zeolite supports was between 2.9 and 3.3 wt%.

Methanol vapor treatment for the catalysts

The methanol treatment of the catalysts was performed in a fixed bed reactor. As a typical run, the catalyst (40–60 meshes) was pre-reduced at 400°C for 3 h in pure H_2 flow (30 mL/min) and then cooled to desired temperature (typically, 200°C) for further treatment. Methanol was introduced into the reactor by a pump with a feeding rate at 0.03 mL/min, where hydrogen was used as a carrier gas with feeding rate at 15 mL/min. In the controlled experiments for comparison, the water, N_2, CO, or H_2 was fed into the reactor instead of methanol to test their influence on the sintering of Cu NPs.

Formaldehyde vapor treatment for the catalysts

The procedure of formaldehyde vapor treatment was basically the same as methanol treatment. The formaldehyde steam was produced by thermal decomposition of paraformaldehyde at 80°C using nitrogen as a carrier gas with a feeding rate at 15 mL/min.

Methanol-triggered migration of Cu from bulky Cu powder

0.03 g of commercial CuO powder was physically mixed with 5.0 g of Beta-deAl zeolite or amorphous SiO_2, and then made into granules with sizes at 40–60 meshes. These granules were localized in the center of the reaction tube, pre-reduced with hydrogen at 400°C for 3 h, and cooled down to 200°C. Then the methanol was introduced into the reactor with a feeding rate of liquid methanol at 0.1 mL/min and hydrogen as a carrier gas with a feeding rate at 10 mL/min.

Study in methanol-triggered gas-phase migration of Cu

0.2 g of commercial CuO powder, 0.5 g of Beta-deAl or SiO_2, and 0.5 g of CeO_2 were localized in a fixed-bed reactor in different layers, and each layer was separated from others by the quartz wool (fig. S46). The mixed beds were reduced at 400°C for 2 h by 10% H_2/Ar flow, and further treated by methanol vapor at 400°C for 12 h with a feeding rate of liquid methanol at 0.1 mL/min and hydrogen as a carrier gas with a feeding rate at 25 mL/min.

Catalyst characterization

XRD characterization

XRD patterns were collected on a Rigaku D/MAX 2550 diffractometer using CuKα radiation (λ = 0.154 nm) with a scanning angle (2θ) range of 5° to 80° at 10°/min. The in situ XRD characterization was performed on a Rigaku SmartLab diffractometer using CuKα radiation (λ = 0.1.54 nm) equipped with an in situ cell. The scanning rate was 10°/min characterizing the range of 10-80°. In a typical experiment, 0.1 g of Cu/Beta-deAl sample was localized in the cell, and reduced at 400°C for 3 h by H_2 (30 mL/min). Then, the sample was cooled down to the desired temperature (e.g. 200°C), and methanol was injected (feeding rate of aqueous methanol at 0.03 mL/min, which was streamed in the cell because of the high temperature) with H_2 as a carrier gas. The XRD patterns were collected every 30 minutes under the given conditions until the diffraction intensity for Cu species were not changed.

SVUV-PIMS characterization

300 mg of CuO powder was physically mixed with 600 mg of Beta-deAl powder, and the samples were made into granules with sizes at 40-60 meshes. In the tests, after pre-reducing the sample at 400°C for 2 h in pure H_2 flow (30 mL/min) and cooling down to 350°C, methanol (0.03 mL/min) was fed into the reaction system using Ar as a carrier gas. The temperature used here was higher than the standard temperature (200°C) for the treatment for Cu/Beta-deAl catalyst for enhancing escape rate of the intermediate that benefits the detection. The data were collected from 350°C to 450°C and the background signals were subtracted.

Gas-phase-reaction ToF-MS characterization

A homemade time-of-flight mass spectrometry (ToF-MS) was used to examine the ion/molecule reactions. The ions of interest were generated by laser ablation of a copper disk (99.999%) in 0.1% O_2 seeded in a He carrier gas with a backing pressure of four standard atmospheres. A 532 nm (second harmonic of Nd^{3+}: yttrium aluminum garnet) laser with an energy of 5–12 mJ/pulse and a repetition rate of 10 Hz was used. The Cu^{2+} ions are then mass-selected by a quadrupole mass filter and enter a linear ion trap (LIT) reactor, where they were confined and thermalized by collisions with a pulse of He gas and then interact with a pulse of different kinds of reactant gases for a period of time. It has been proved that the ions were thermalized close to room temperature before reactions (*47, 48*). The ions ejected from the LIT were detected by reflection ToF-MS.

Some other characterizations

STEM images were obtained on a FEI Tecnai G^2 F20 S-TWIN equipped with a high angle energy dispersive X-ray (EDX) detector at an acceleration voltage of 200 kV. To observe very small Cu NPs, STEM images were obtained on FEI Titan G2 80-200 ChemiSTEM. The samples after usage or treatment were dried, dispersed in ethanol and then introduced on Mo or Au grids. About 200–250 particles were counted to calculate the mean size and standard deviation of Cu NPs by the software OriginPro, ver. 2021 (OriginLab Corp.) using statistics functions. SEM characterization

was performed using a Hitachi SU-8010 electron microscopy. N_2 sorption isotherms of the catalysts were obtained by a Micromeritics TriStar II 3020 surface area and pore analyzer. The specific surface area (S_{BET}) was calculated using the Brunauer–Emmett–Teller (BET) method. Thermogravimetric (TG) profiles were acquired using SDT Q600. The samples were dried under vacuum for 10 h, and further dried at 300°C overnight in nitrogen prior to measurement in order to remove the water or other organic compounds adsorbed on catalyst surface after catalysis. About 11-12 mg of sample was employed for the measurement at 30 to 800°C in air with a temperature ramping rate of 10°C/min. The gaseous products for the sample after the methanol treatment (by N_2 as carrier gas) were collected in a bag, and analyzed by mass spectrometer (SRD200M, TILON) in flowing Ar (5 mL/min, *m/z* at 2, 28, 30, 40, 44).

FT-IR characterizing the zeolite silanols under vacuum

The samples were heated to 400°C for 1 h under Ar atmosphere to remove water contained in the cell and catalyst surface. After cooling to room temperature, the cell was connected to a vacuum pumping system until the pressure was lower than 10^{-5} mbar, then the spectra were recorded. For characterization of silanol species, the spectra were collected at 150°C.

X-ray absorption fine structure (XAFS)

XAFS spectra at Cu *K*-edge (E_0 = 8979 eV) were collected at BL11B beamline of Shanghai Synchrotron Radiation Facility (SSRF). The XAFS data were recorded under a fluorescence mode with standard Lytle ion chamber. The energy was calibrated according to the absorption edge of pure Cu foil. All the samples were prepared in glove box under N_2 atmosphere to avoid exposure to air. The data were extracted, and the profiles were fitted according to Athena and Artemis codes.

Catalytic tests

The hydrogenation of DMO was performed in a stainless steel fixed-bed flow reactor with an inner diameter of 10 mm. Typically, 0.5 g of catalyst (40–60 meshes) was diluted with 2 g of quartz sands (40–60 meshes) to maintain a height of 20 mm for catalyst bed into the center of the reactor, and additional quartz sands were placed into the reactor to maintain the catalyst bed. The catalysts were pre-reduced at 400°C for 3 h in pure H_2 flow (30 mL/min). The DMO solution (10 wt% in methanol) was then pumped into the reactor using a LC-20AD$_{XR}$ pump (Nexera XR, Shimadzu) at varied feeding rates (0.01-0.05 mL/min) to result in liquid hour space velocity (LHSV) on the basis of DMO at 0.4–3.7 h^{-1} (LHSV at room temperature). For the comparison of performances of each catalyst before and after the methanol treatment at 400°C (Fig. 2D in the main text), the LHSV at 3.0 h^{-1} was used for evaluating the Cu/SiO_2-C and 1.8 h^{-1} for Cu/Bete-deAl because of their distinguished Cu contents. Considering that methanol is the feedstock for DMO synthesis (*28, 29*) and the product of DMO hydrogenation, methanol vapor is usually used as carrier for DMO hydrogenation (*21, 28-32, 42*). Therefore, we performed the reactions with methanol cofeeding.

After reaction, the products were collected by a cold bath and analyzed offline by a gas chromatography (FULI 9790) equipped with a Stabilwax-DA column (60 m × 0.53 mm × 0.5 μm) and a flame ionization detector (FID). The liquid products were quantified by using 1,4-dioxane as an internal standard. These products were further identified by GC–MS (QP2010SE, Shimadzu). The gaseous products were also analyzed using on-line gas chromatography equipped with thermal conductivity detector, where the C_2 products was negligible. Ethanol and C_3/C_4 oxygenates were the main by-products. The conversion and selectivity were measured by testing more than five

times, and the experimental error bounds were within ±1.5%. The conversion, selectivity, and yield were calculated as follows:

$$\text{Conversion (\%)} = [1-\frac{\text{Amount of remaining DMO (mol)}}{\text{Amount of DMO in the feed (mol)}}] \times 100\%$$

$$\text{Selectivity of product (\%)} = \frac{\text{Product (mol)} \times n_{carbon}}{(\text{Converted DMO (mol)} \times n_{carbon})} \times 100\%$$

$$\text{Yield of product (\%)} = \text{Conv. \%} \times \text{Sel. \%}$$

Computational Methods

Density Functional Theory (DFT) calculation

All the total energies were obtained from the periodic DFT calculations implemented in Vienna *ab initio* Simulation Package (VASP) (*54, 55*). The Bayesian Error Estimation Functional with the vdW-DF2 nonlocal correlation energy and potential (BEEF-vdW) was used to describe the exchange-correlation interaction. The calculated adsorption energy of CO molecules on the Cu(111) fcc site is -0.67 eV, in agreement with the reported experimental value of -0.70 eV (*56*). The cut-off energy of plane-wave basis set was 450 eV. The Cu/Beta-deAl was modeled using the Cu_{13} cluster over the exposed Beta-deAl(101) surface in a slab of 29.1 × 12.6 × 22.4 Å. The SiO_2 surface was modeled using the *p*(3×2) hydroxyl (100) surface with the vacuum thickness of 10 Å along the z direction. The bottom two Si-O layers were fixed while the other layers and adsorbates were relaxed during the optimization. The Γ-point was used for the first Brillouin zone integration. The geometry structures of the intermediates were optimized using the conjugate gradient method, while the transition state was searched using the constrained optimization method based on the L-BFGS algorithm (*57*). The convergency criterion was set as 0.05 eV/Å for the forces. The vibrational frequencies were also calculated based on the numeric difference and Harmonic oscillator approximation to verify the transition state with only one imaginary frequency along the reaction coordination. The free energy was further calculated with the zero-point energy, internal energy, and entropy correction by the partition function based on Boltzmann distribution at 473 K (*58*). To ensure the thermodynamic consistency, the energies of the gaseous molecules were corrected with the proposed values from Studt et al. (*59*).

Crystal Orbital Hamilton Population (COHP)

COHP analysis was carried out using LOBSTER package (*60-62*). The -COHP was applied in order to be compatible with Crystal Orbital Overlap Population (COOP) analysis. The strength of the Cu-O bond between the Cu clusters and the silanol nests or SiO_2 surface was measured using the integration of the contribution of the energy bands up to the Fermi level based on the projected crystal orbital Hamiltonian (IpCOHP). The more positive the -IpCOHP, the stronger the bond.

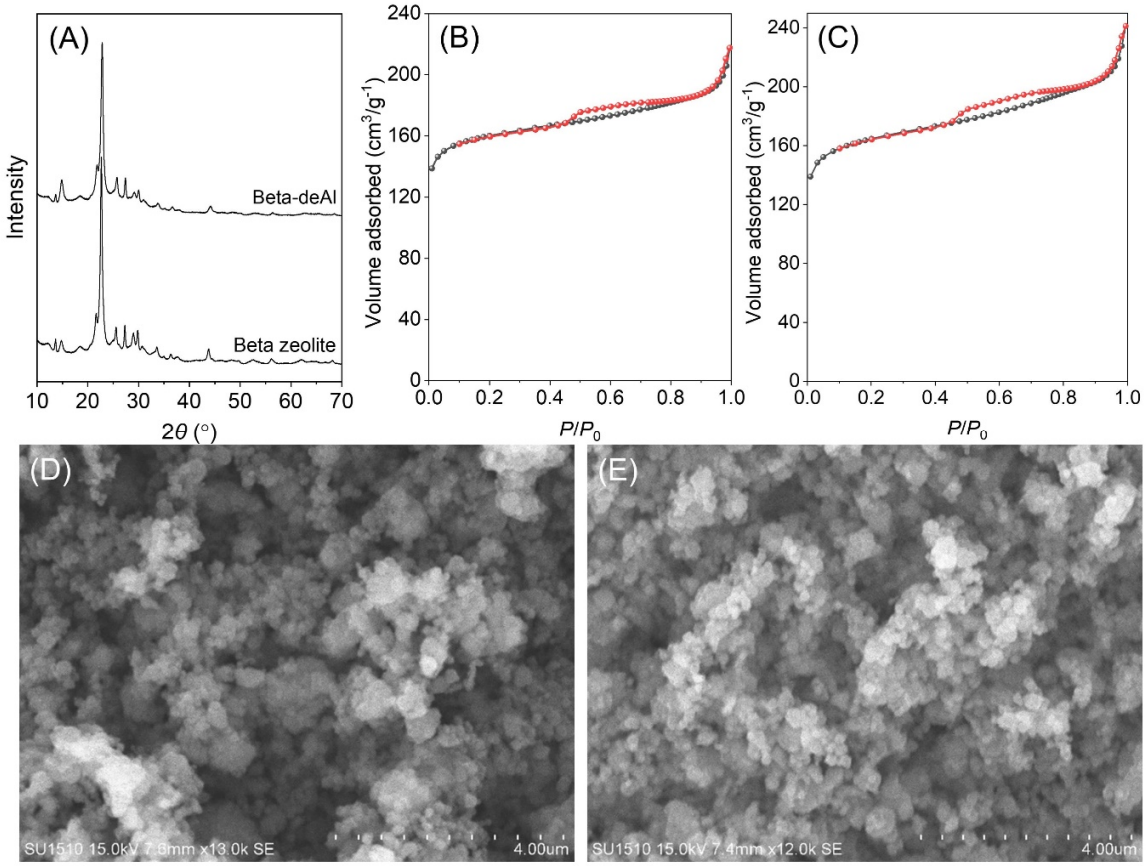

Fig. S1. (A) XRD patterns of commercial Beta zeolite and Beta-deAl. N_2 sorption isotherms of (B) commercial Beta zeolite (Si/Al ratio of 13, S_{BET} of 544 m^2/g) and (C) Beta-deAl (Si/Al ratio of 1250, S_{BET} of 561 m^2/g). SEM images of (D) commercial Beta and (E) Beta-deAl zeolites.

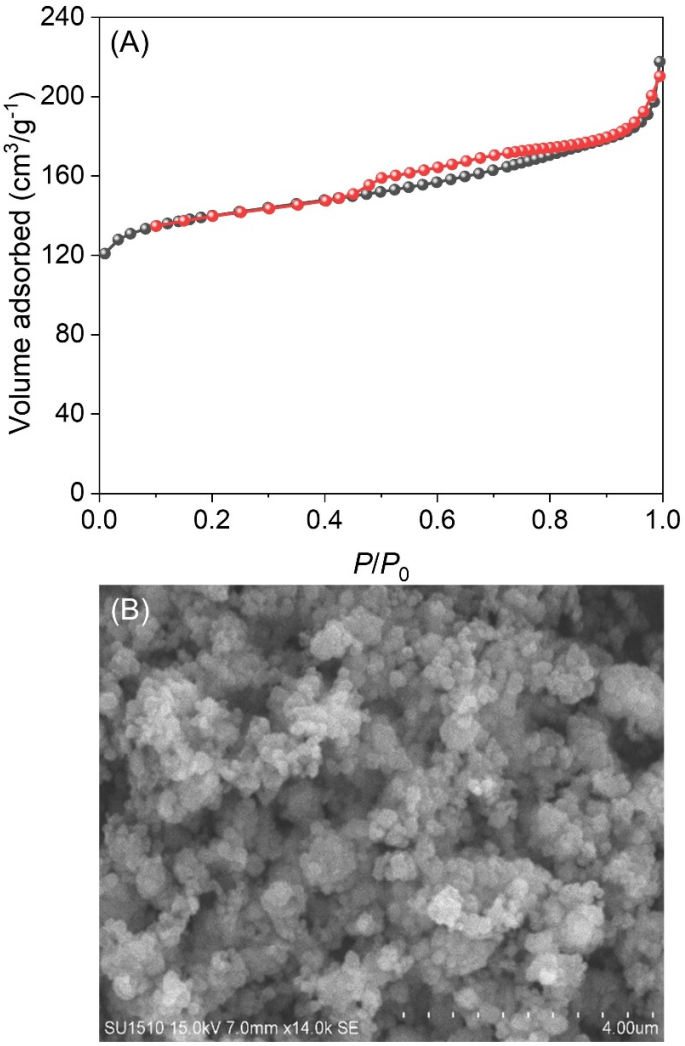

Fig. S2. (A) N_2 sorption isotherms and (B) SEM image of the Cu/Beta-deAl (3 wt% Cu, S_{BET} of 475 m^2/g).

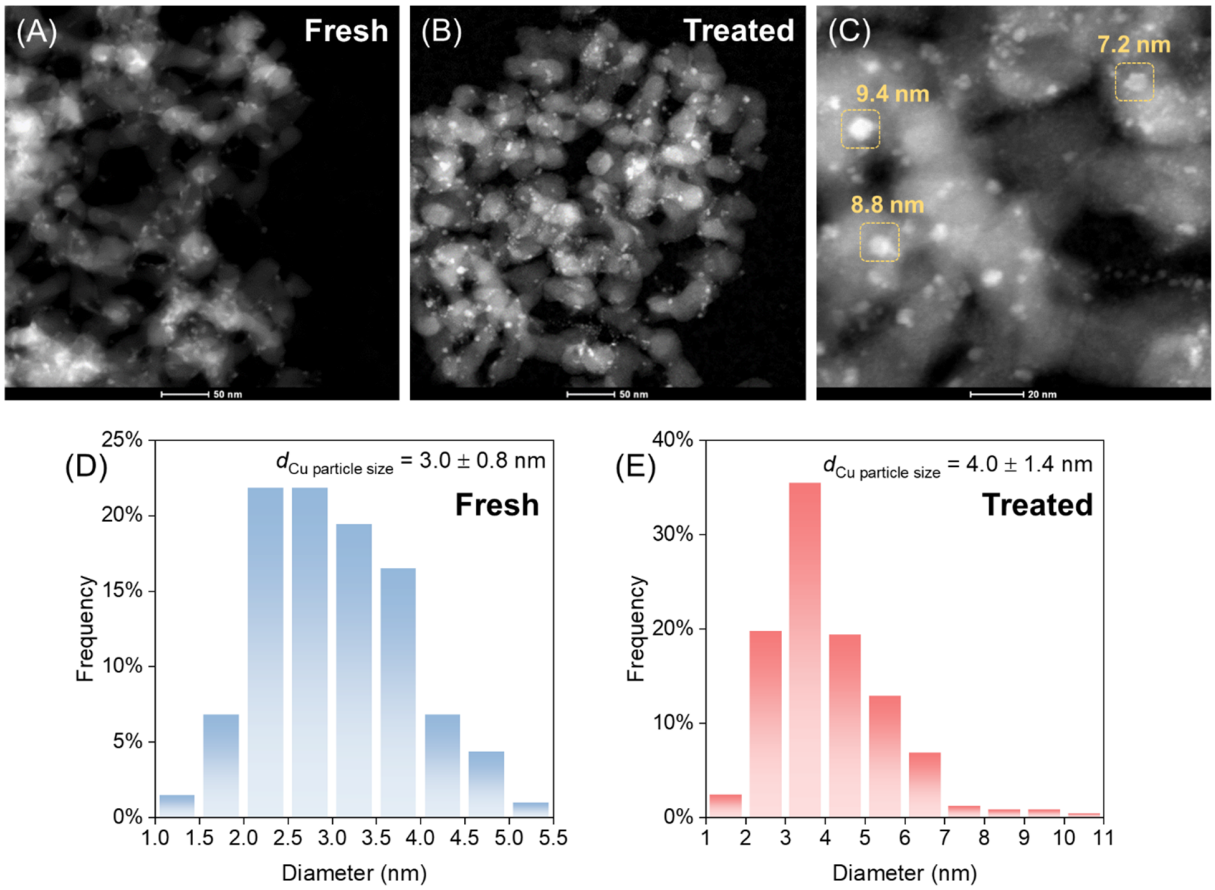

Fig. S3. STEM images of the Cu/SiO_2 (3 wt% Cu) (A) before and (B and C) after the methanol treatment at 200°C for 12 h. Cu NPs size distribution of (D) fresh and (E) methanol-treated Cu/SiO_2.

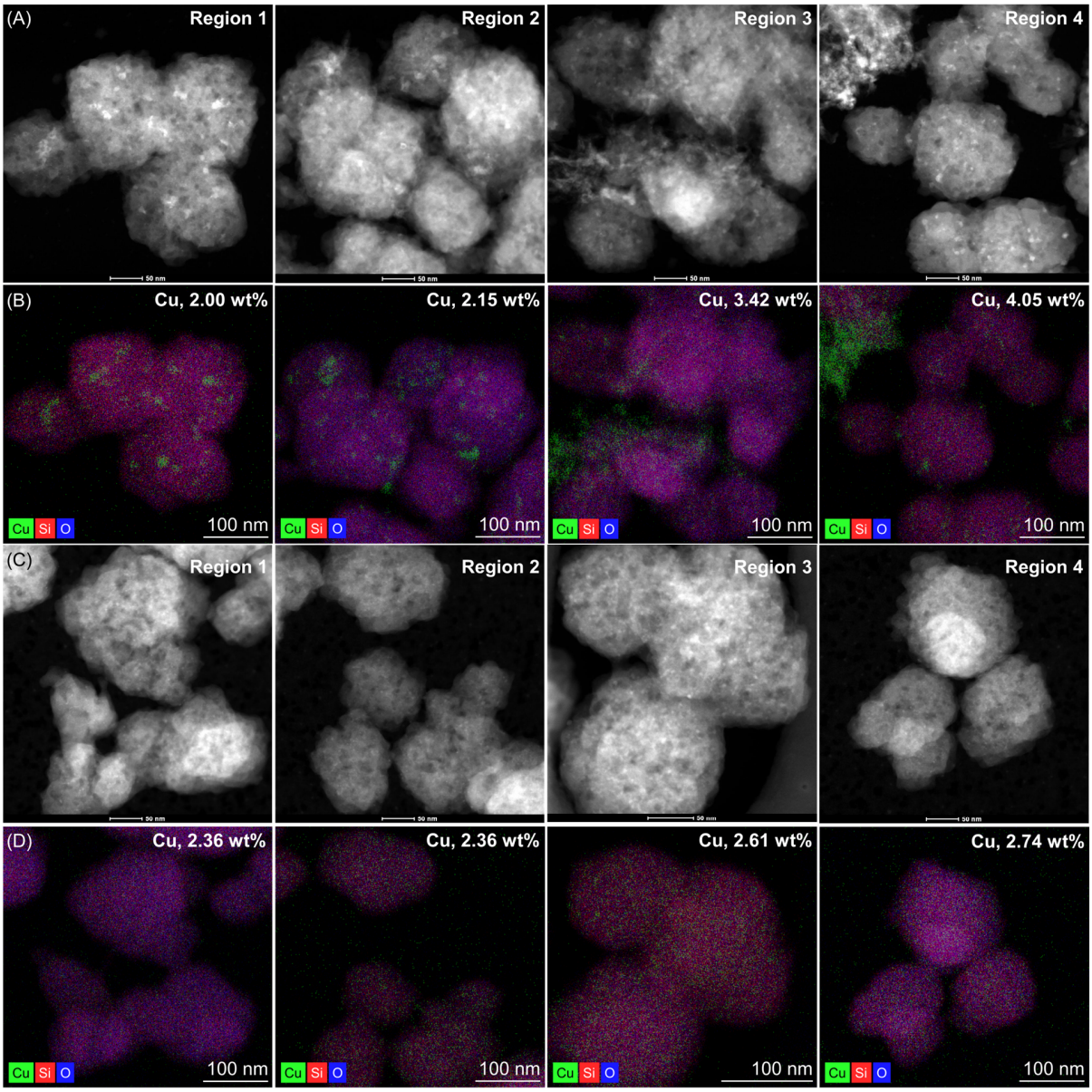

Fig. S4. STEM images characterizing the different regions on the (A) fresh Cu/Beta-deAl and (C) Cu/Beta-deAl after the methanol treatment at 200°C for 12 h (the same treatment conditions as those in Fig. 1A and B in the main text). (B and D) The corresponding EDS elemental maps and Cu contents by EDS analysis.

Note: The Cu NPs on the Cu/Beta-deAl could be changed into smaller ones after the methanol treatment. This phenomenon was not only observed in the STEM images of Fig. 1A and B in the main text, but also in the STEM images characterizing different randomly selected regions on the sample. As shown in fig. S4, the STEM images of different regions on the fresh Cu/Beta-deAl sample showed Cu NPs with sizes at 2-14 nm (fig. S4A). After the methanol treatments, smaller Cu NPs were obtained in the different regions with sizes at 1-5 nm (fig. S4C). More uniform

dispersion of Cu species on the methanol-treated Cu/Beta-deAl could also be observed by the Cu elemental maps (fig. S4B and D).

We analyzed the Cu contents in different regions of Cu/Beta-deAl by EDS. The different regions on fresh Cu/Beta-deAl showed varied Cu contents from 2.00 to 4.05 wt% (fig. S4B), while the methanol-treated sample showed similar Cu contents in different regions at 2.36-2.74 wt% (fig. S4D), suggesting more uniform Cu dispersion after the methanol treatment. (The Cu contents on the Cu/Beta-deAl before and after methanol treatment were both 3.0 wt% by ICP, which is due to the inherent error between ICP and EDS analysis.)

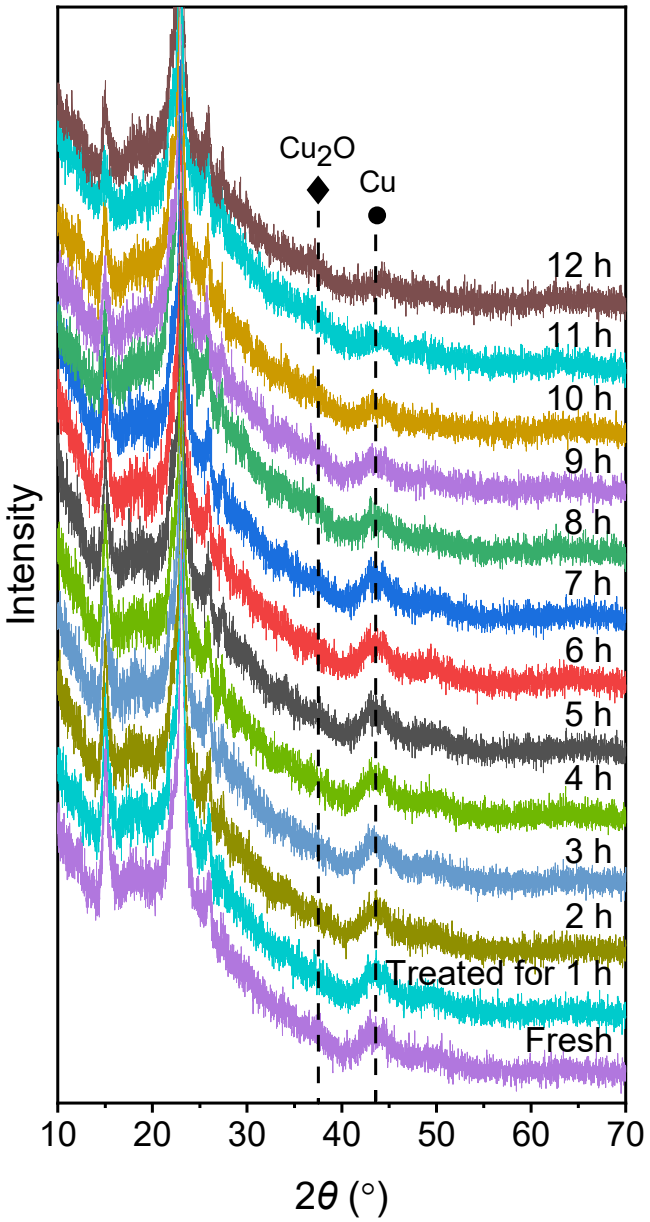

Fig. S5. In situ XRD patterns for the Cu/Beta-deAl during the methanol treatment. The treatment was performed at 200°C for 12 h with a methanol feeding rate of 0.03 mL/min. The patterns at 2, 4, 6, 8, 10, and 12 h were selected and shown in Fig. 1C of the main text.

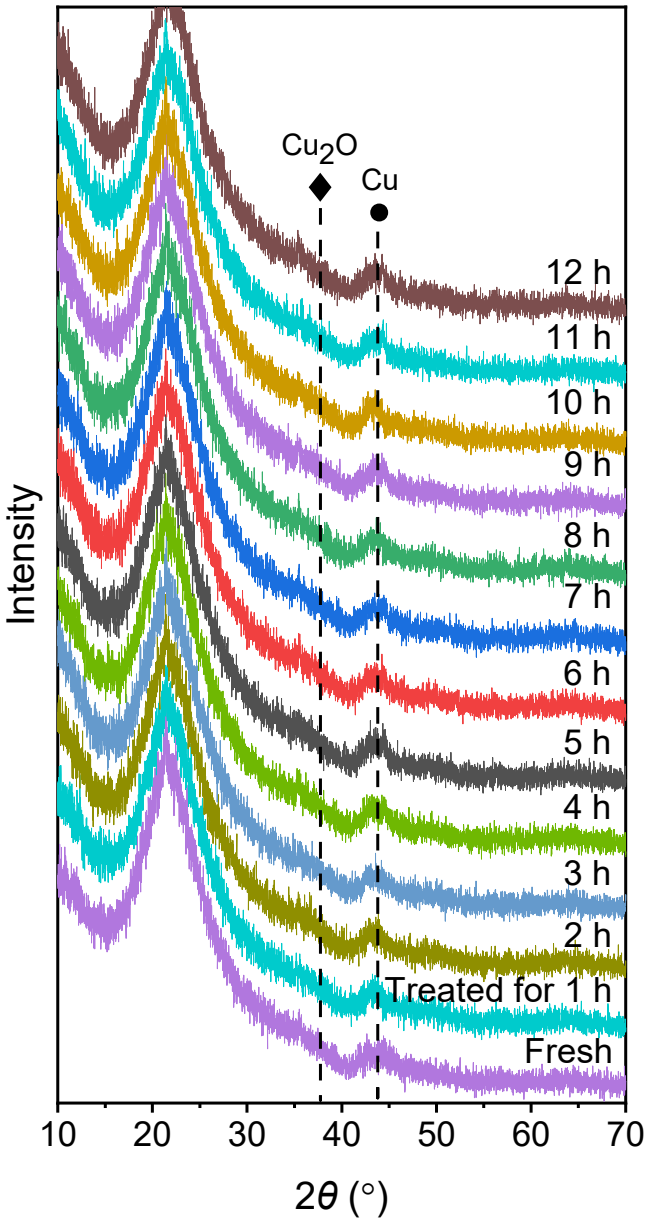

Fig. S6. In situ XRD patterns for the Cu/SiO_2 (3 wt% Cu) during the methanol treatment. The treatment was performed at 200°C for 12 h with a methanol feeding rate at 0.03 mL/min.

Note: The diffraction of metallic Cu phase at 43.3° (*31, 32*) was gradually enhanced by the methanol treatment with time prolonged on the Cu/SiO_2. This is assigned to the sintering of Cu NPs on SiO_2, which is consistent with the TEM results in fig. S3.

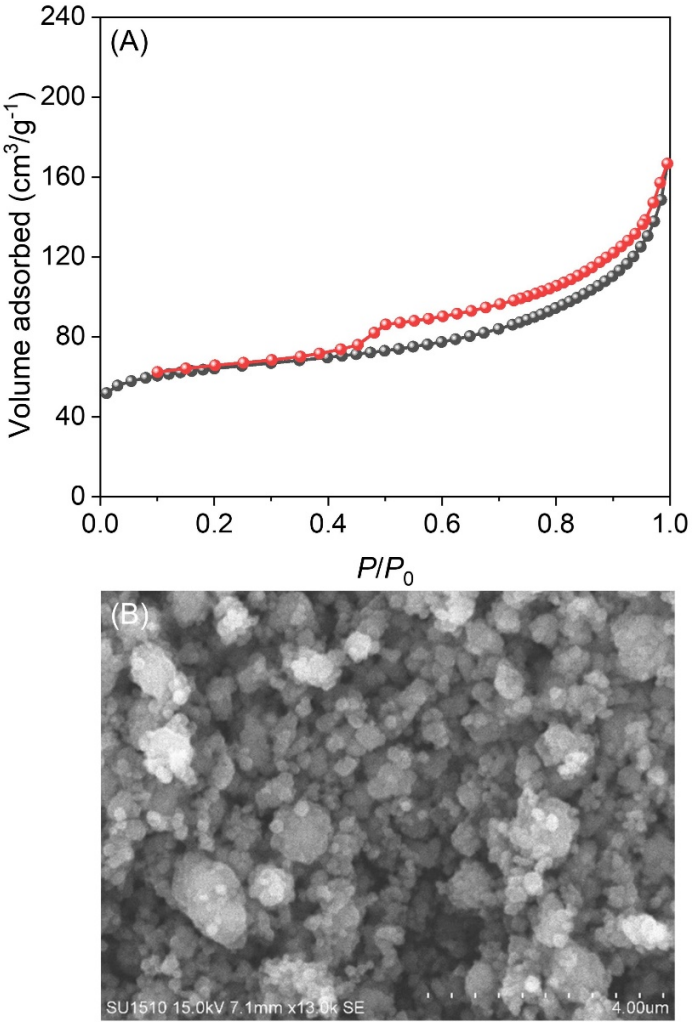

Fig. S7. (A) N_2 sorption isotherms and (B) SEM image of the Cu/Beta (3 wt% Cu, S_{BET} of 220 m^2/g).

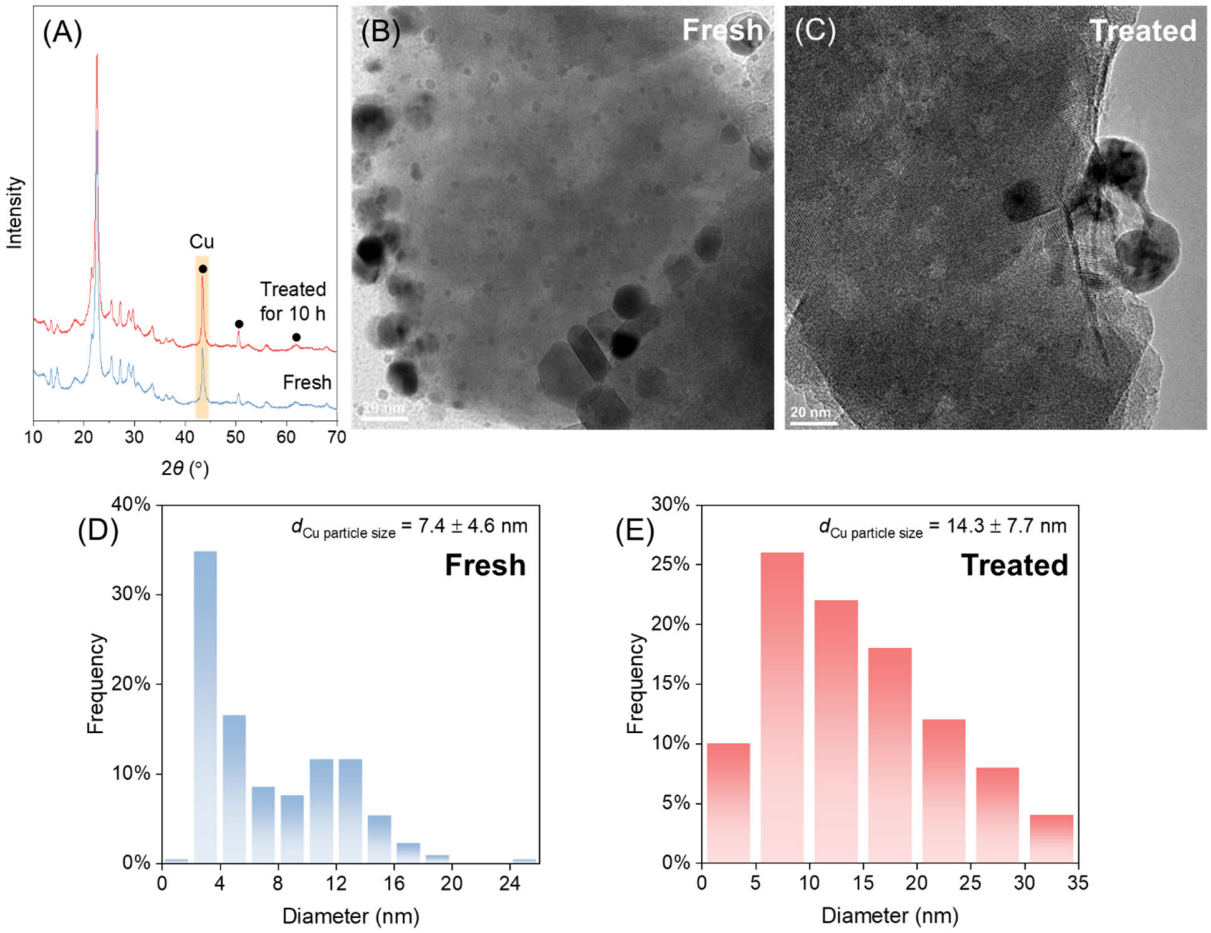

Fig. S8. XRD and TEM characterizing Cu/Beta (3 wt% Cu) before and after the methanol treatment. (A) XRD patterns of the fresh and methanol-treated Cu/Beta. TEM images and Cu NP size distributions of (B and D) fresh and (C and E) methanol-treated Cu/Beta.

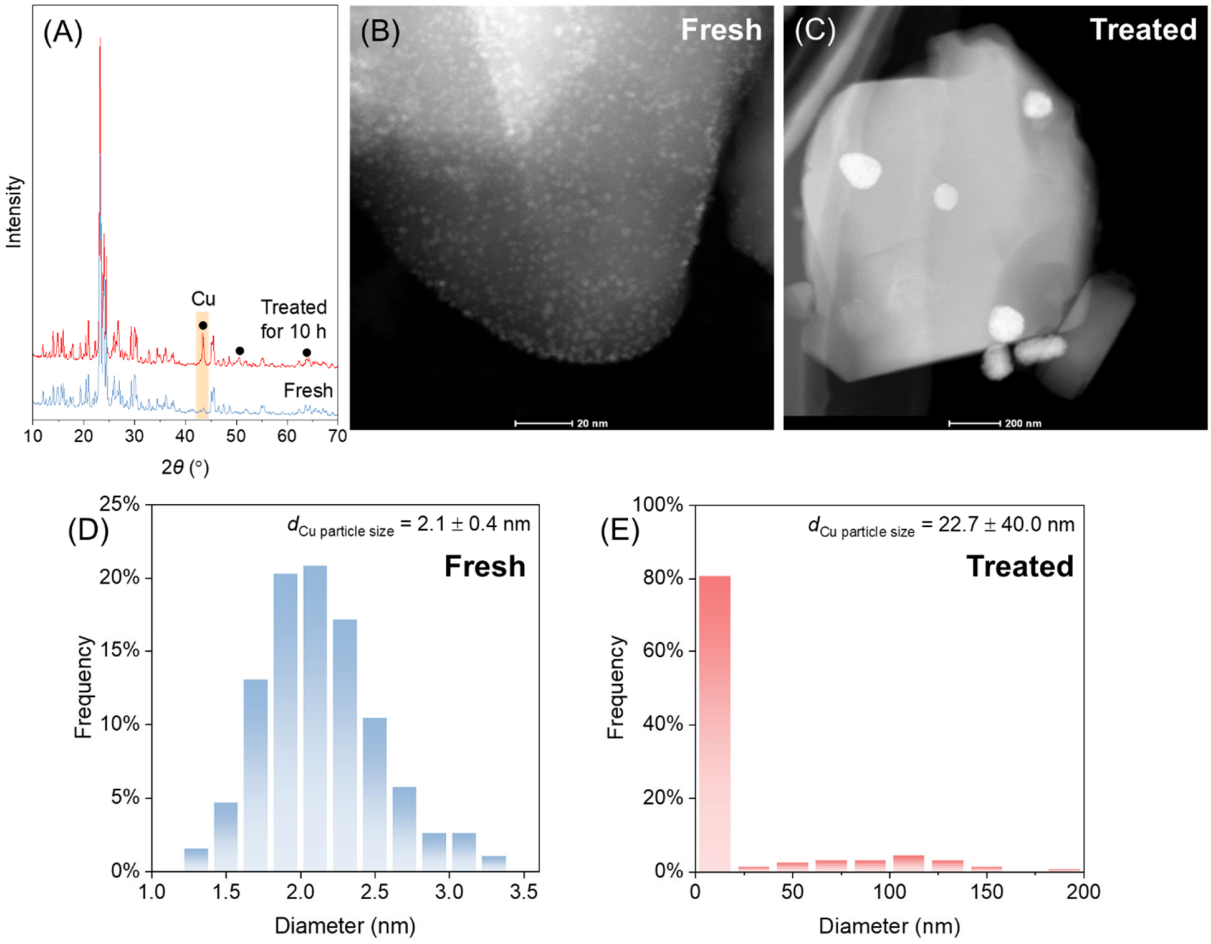

Fig. S9. XRD and STEM characterizing Cu/ZSM-5 (3 wt% Cu) before and after the methanol treatment. (A) XRD patterns of the fresh and methanol-treated Cu/ZSM-5. STEM images and Cu NP size distributions of (B and D) fresh and (C and E) methanol-treated Cu/ZSM-5.

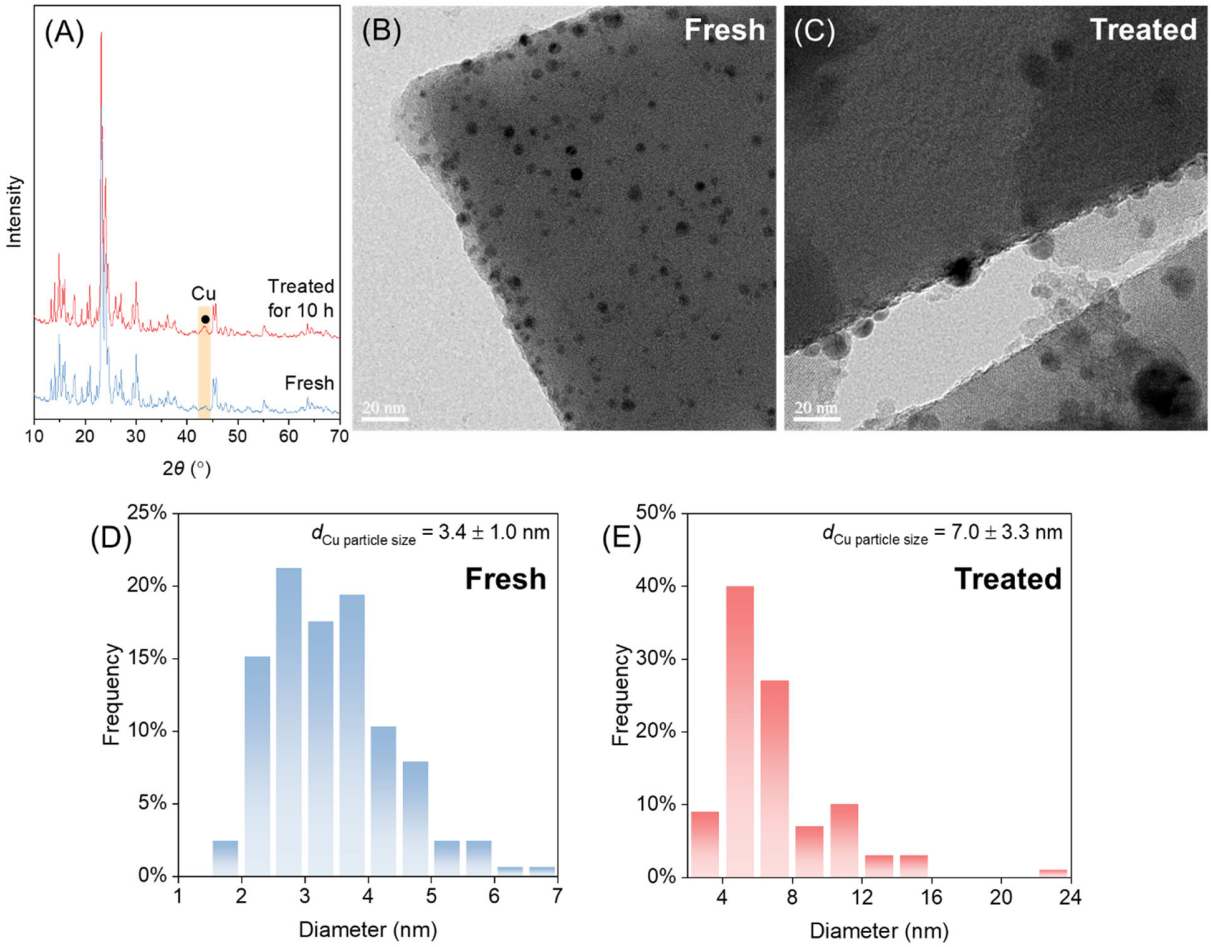

Fig. S10. XRD and TEM characterizing Cu/S-1 (3 wt% Cu) before and after the methanol treatment. (A) XRD patterns of the fresh and methanol-treated Cu/S-1. TEM images and Cu NP size distributions of (B and D) fresh and (C and E) methanol-treated Cu/S-1.

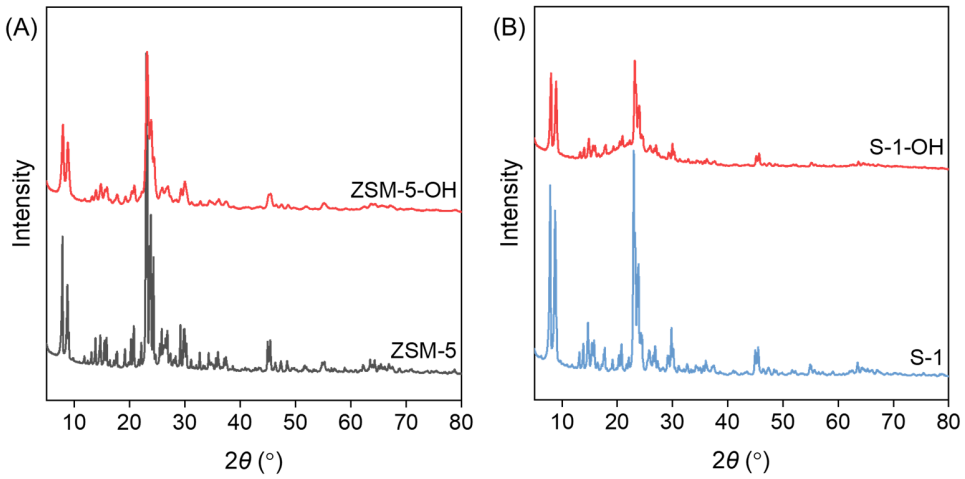

Fig. S11. XRD patterns of various MFI zeolites.

Note: Silanol-modified aluminosilicate ZSM-5 (ZSM-5-OH) and siliceous S-1 (S-1-OH) were rationally synthesized (*52*). XRD patterns of these materials all exhibited typical diffractions assigned to the MFI structure.

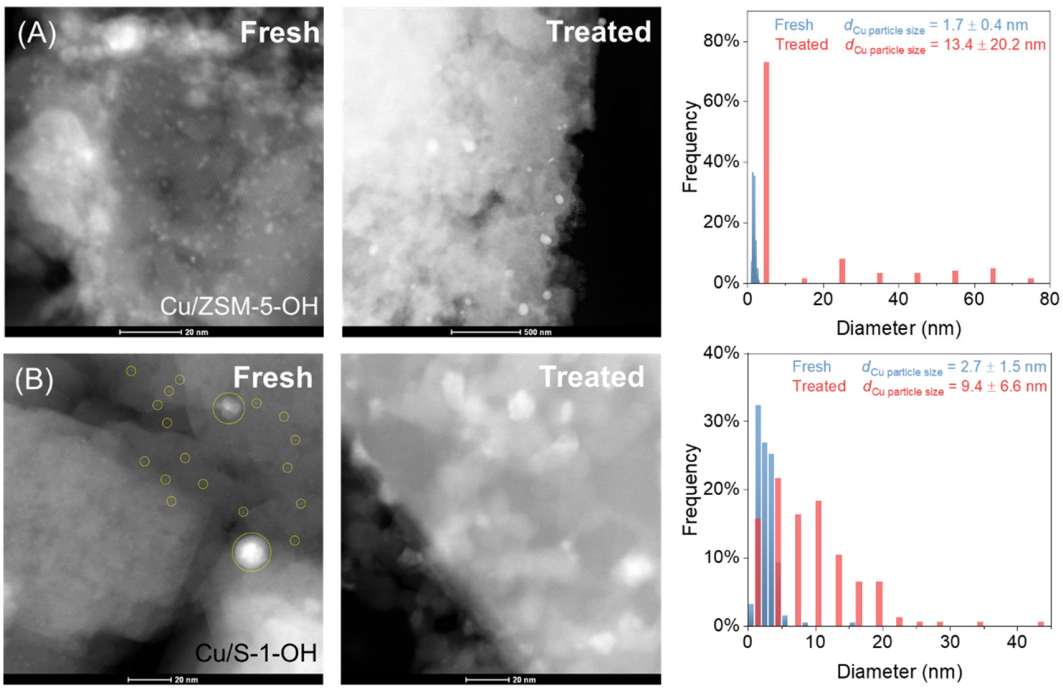

Fig. S12. STEM images and Cu NP size distributions of Cu NPs supported on (A) ZSM-5-OH and (B) S-1-OH before and after the methanol treatment. The Cu NPs on these zeolites were also sintered into larger ones after the methanol treatments.

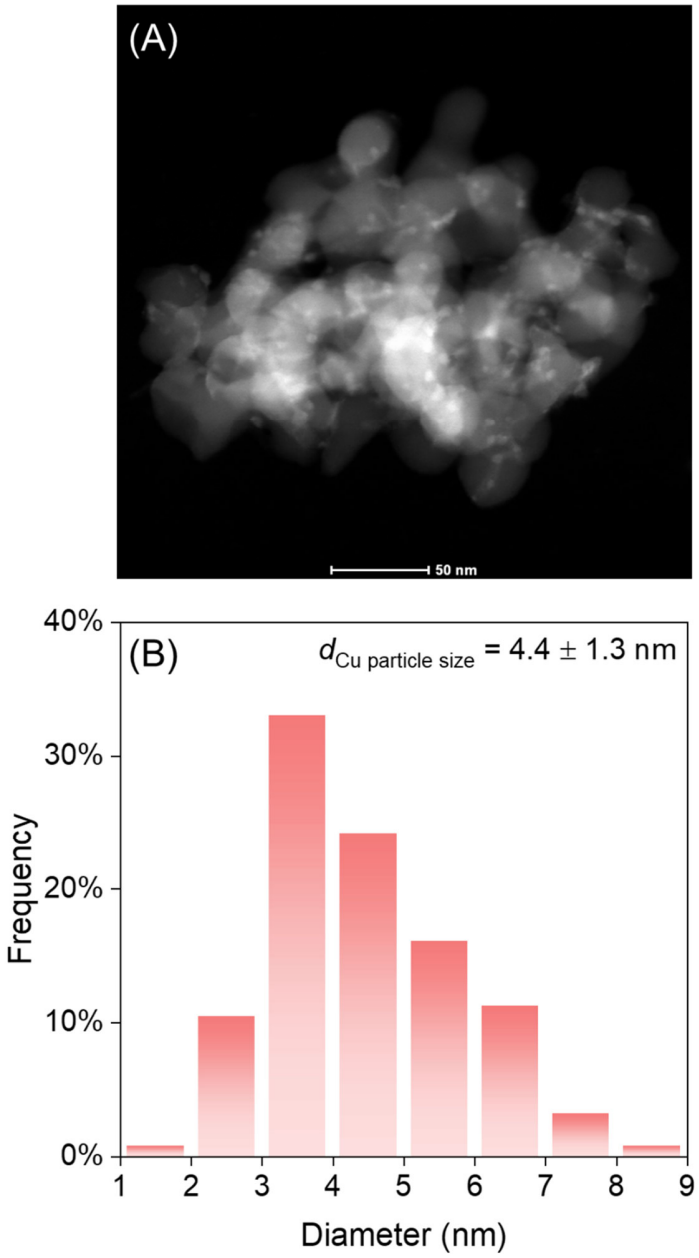

Fig. S13. (A) STEM image and (B) Cu NP size distribution of the spent Cu/SiO_2 after the DMO hydrogenation test for 80 h. The reaction conditions were the same to those in Fig. 2A of the main text.

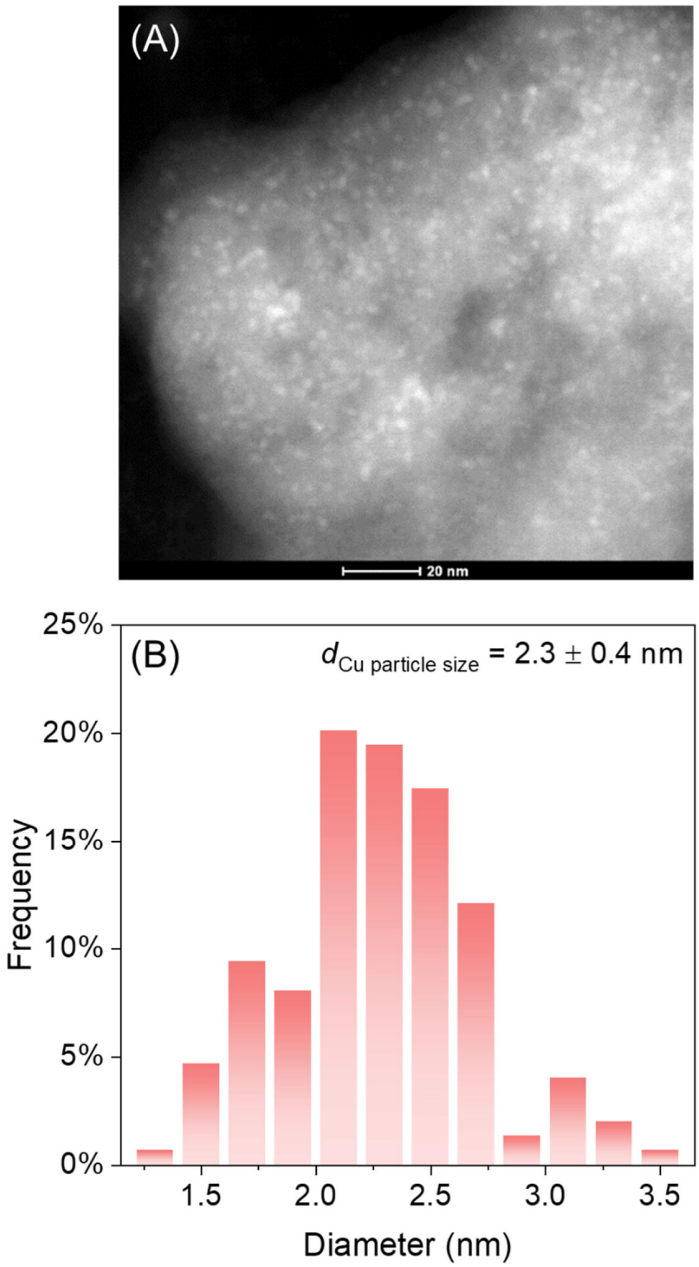

Fig. S14. (A) STEM image and (B) Cu NP size distribution of the spent Cu/Beta-deAl catalyst after the DMO hydrogenation test for 10 h. The reaction conditions were the same to those in Fig. 2A of the main text.

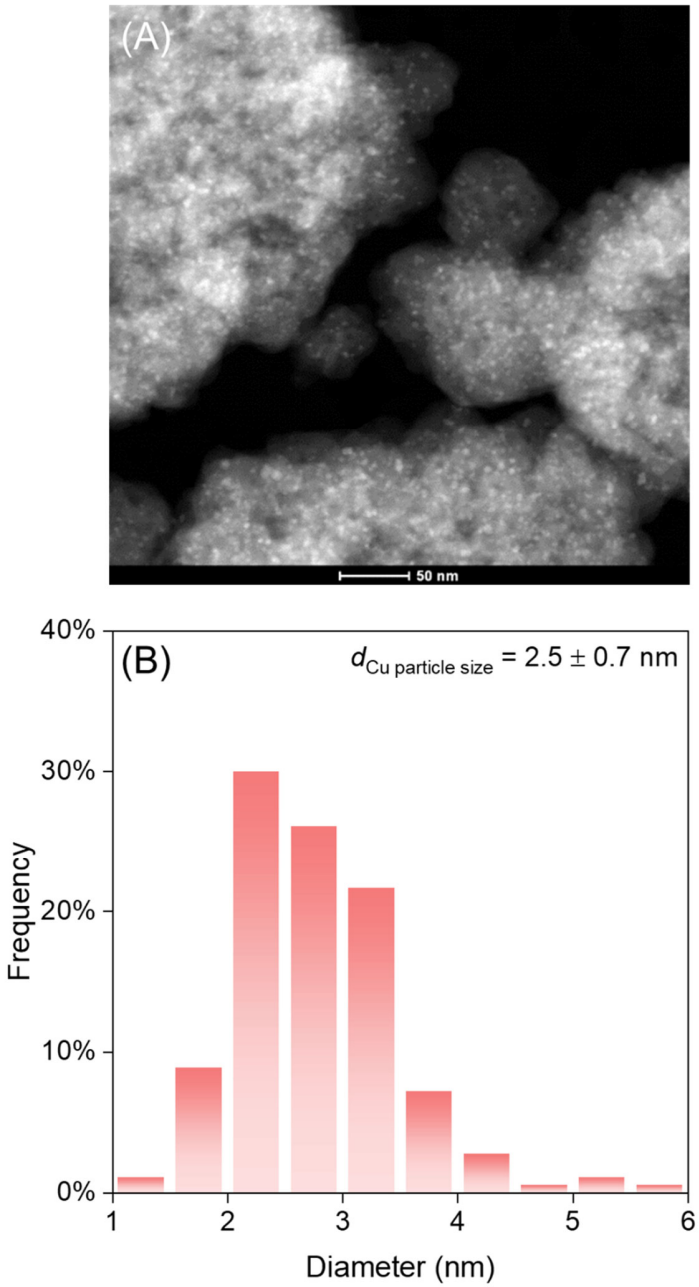

Fig. S15. (A) STEM image and (B) Cu NP size distribution of the spent Cu/Beta-deAl catalyst after the DMO hydrogenation test for 80 h. The reaction conditions were the same to those in Fig. 2A of the main text.

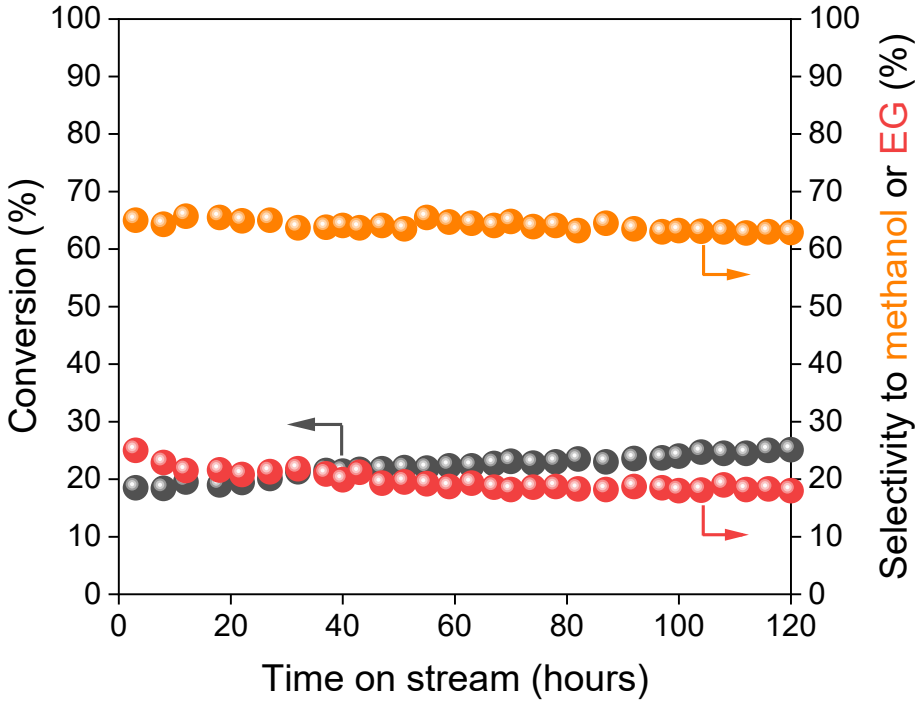

Fig. S16. Data showing the catalytic performances of Cu/Beta-deAl in the DMO hydrogenation using 1,4-dioxane as solvent. Reaction conditions: 200°C, 2.5 MPa, LHSV of 0.8 h^{-1}. Other products mainly included methyl glycolate and ethanol.

Note: We also performed the reaction using 1,4-dioxane as solvent. As shown in fig. S16, the spent Cu/Beta-deAl catalyst after the tests in DMO hydrogenation for 120 h (10 wt% DMO in 1,4-dioxane as feed) showed average Cu NP size at 2.4 nm, which is smaller than 5.6 nm of the fresh catalyst (Fig. 1A in the main text). In the conversion-time profiles of the DMO hydrogenation for 120 h, the DMO conversion was gradually increased from 18.5% to 25.1% on the Cu/Beta-deAl, which might be ascribed to that the methanol product results in the re-dispersion of Cu NPs.

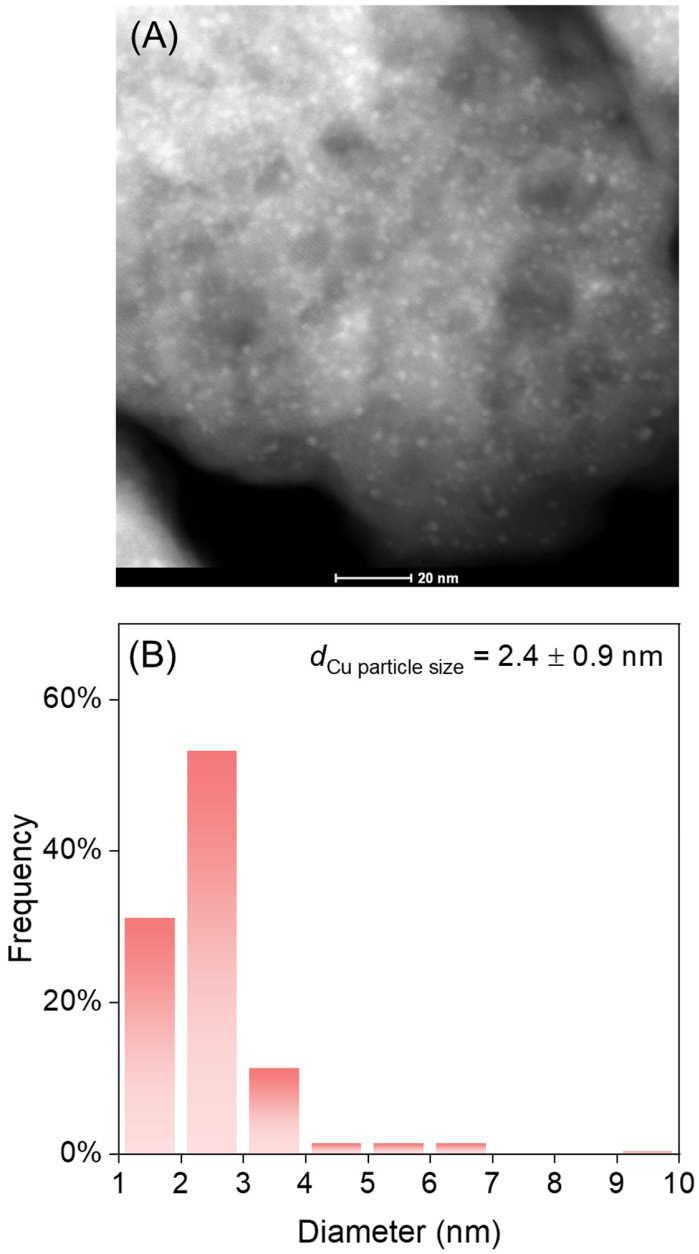

Fig. S17. (A) STEM image and (B) Cu NP size distribution of the spent Cu/Beta-deAl in 10 wt% DMO in 1,4-dioxane as solvent.

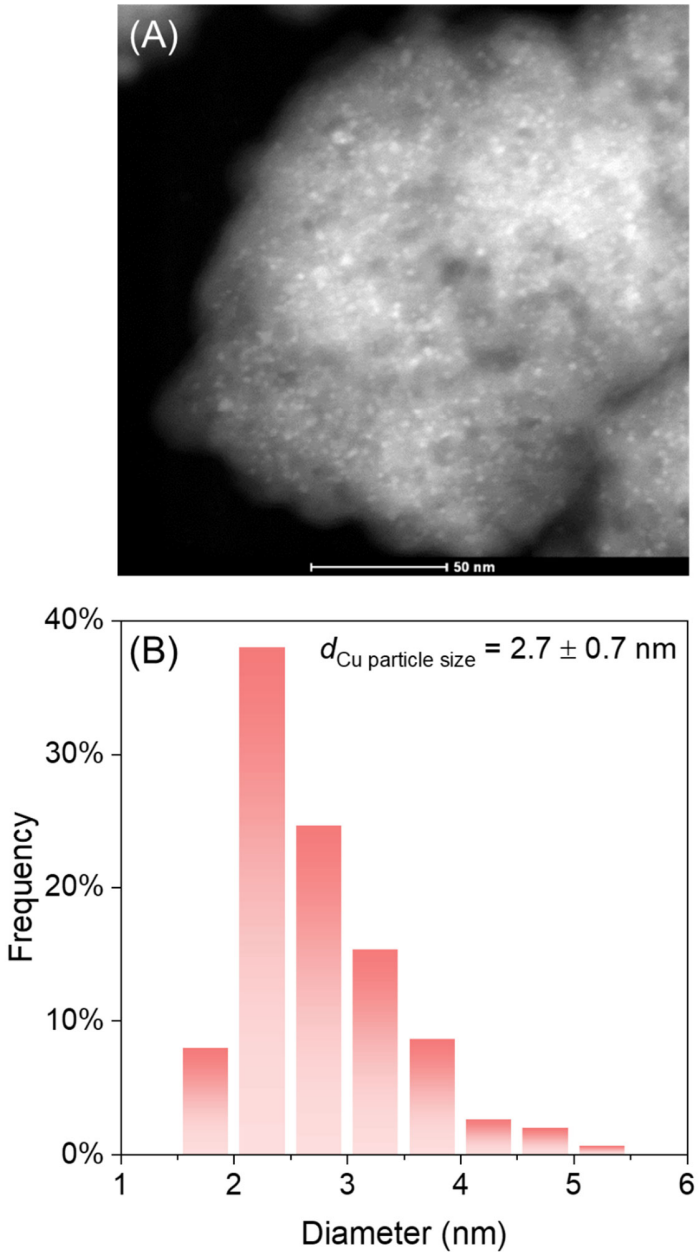

Fig. S18. (A) STEM image and (B) Cu NP size distribution of the spent Cu/Beta-deAl catalyst after the DMO hydrogenation test for 200 h. The reaction conditions were the same to those in Fig. 2C of the main text.

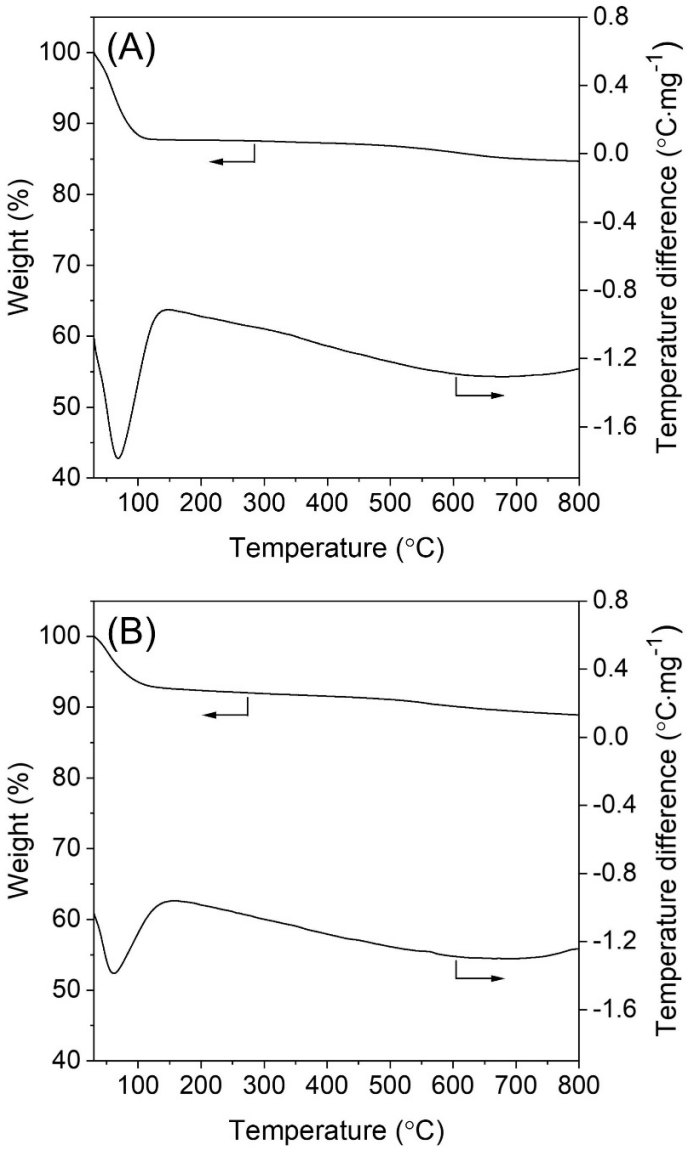

Fig. S19. TG profiles of (A) Beta-deAl support and (B) spent Cu/Beta-deAl catalyst after test in DMO hydrogenation for 200 h.

Note: The spent Cu/Beta-deAl catalyst showed TG profiles that was similar with that of the Beta-deAl support in the region with temperatures higher than 150°C, suggesting the negligible coke on the Cu/Beta-deAl.

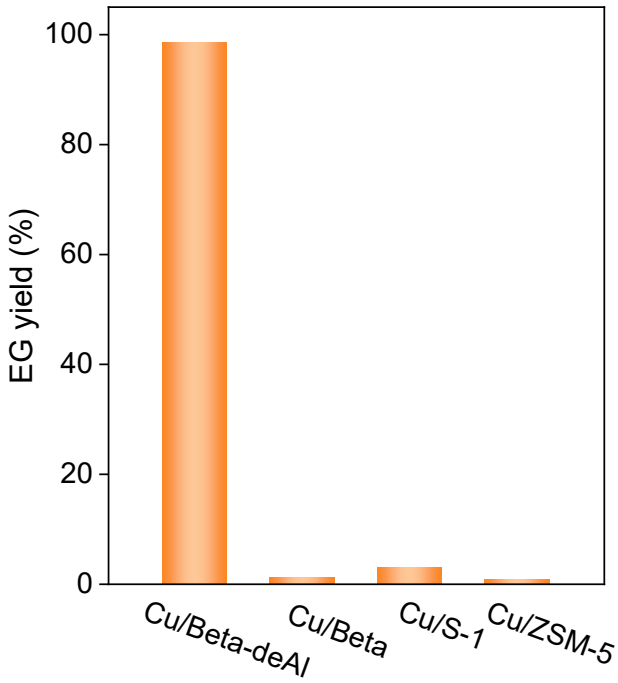

Fig. S20. Data showing the yields of EG from DMO hydrogenation over different zeolite supported Cu catalysts. The reaction conditions are the same to those in Fig. 2C of the main text.

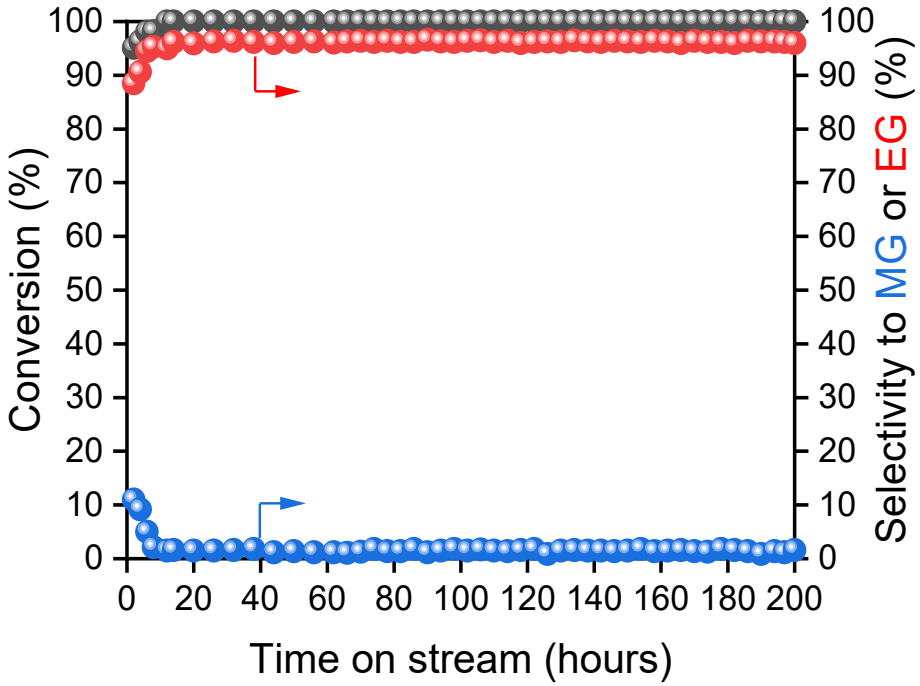

Fig. S21. Data showing the performances of Cu/Beta-deAl-18% in DMO hydrogenation for a long period. Reaction conditions: 200°C, 2.5 MPa, LHSV of 1.8 h^{-1}, and $n(H_2)/n$(DMO) of 60.

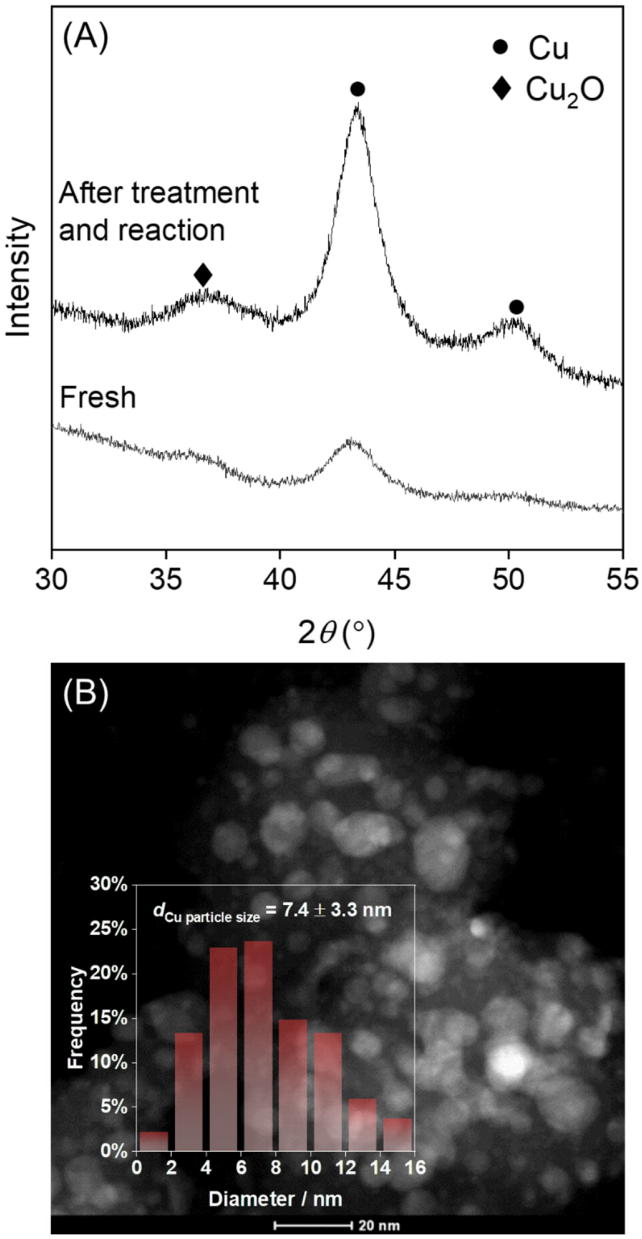

Fig. S22. (A) XRD patterns of the fresh and spent commercial Cu/SiO_2-C catalysts after the methanol treatment at 400°C and test in DMO hydrogenation. (B) STEM image of the spent Cu/SiO_2-C catalyst after the methanol treatment at 400°C and test in DMO hydrogenation.

Note: In the XRD patterns, the diffractions of metallic Cu were strong and sharp on the spent Cu/SiO_2-C catalyst, compared with that on the fresh one, suggesting the Cu sintering.

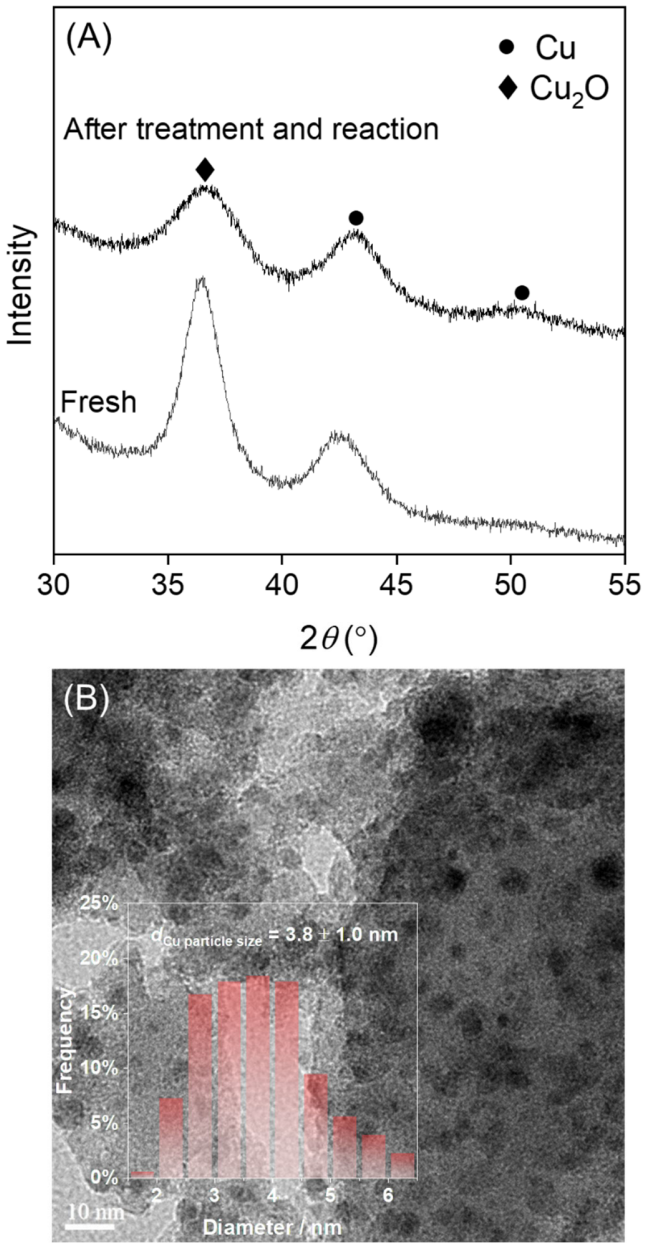

Fig. S23. (A) XRD patterns of the fresh and spent Cu/Beta-deAl-18% catalysts after the methanol treatment at 400°C and test in DMO hydrogenation. (B) TEM image of the spent Cu/Beta-deAl-18% catalyst after the methanol treatment at 400°C and test in DMO hydrogenation.

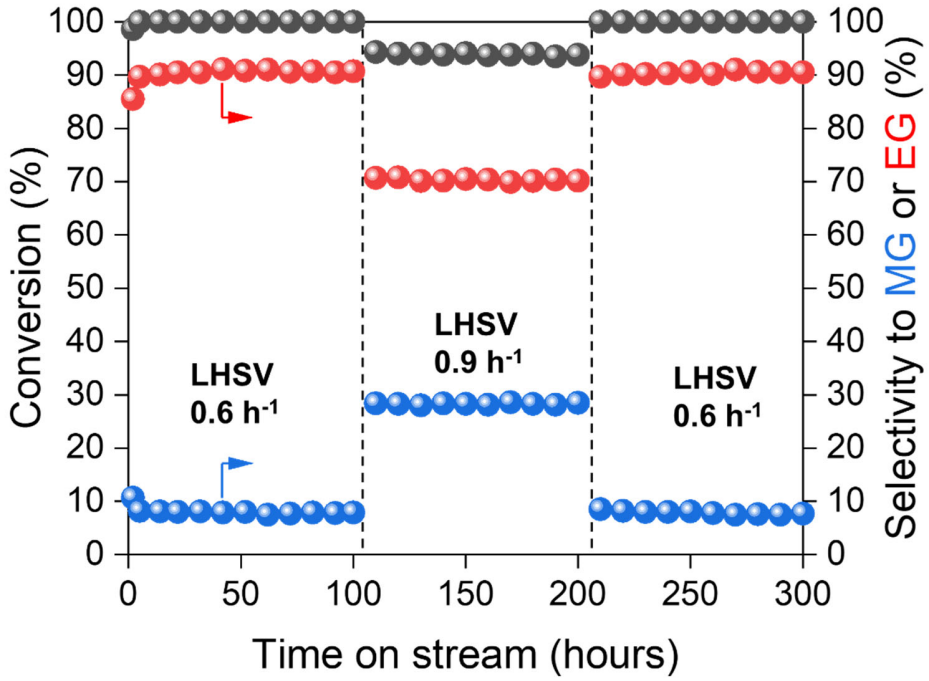

Fig. S24. Data showing the performances of the Cu/Beta-deAl-18% catalyst in DMO hydrogenation at ambient pressure under different LHSVs. Reaction conditions: 200°C, 0.1 MPa, $n(H_2)/n(DMO)$ of 240 (LHSV of 0.6 h^{-1}), and $n(H_2)/n(DMO)$ of 160 (LHSV of 0.9 h^{-1}).

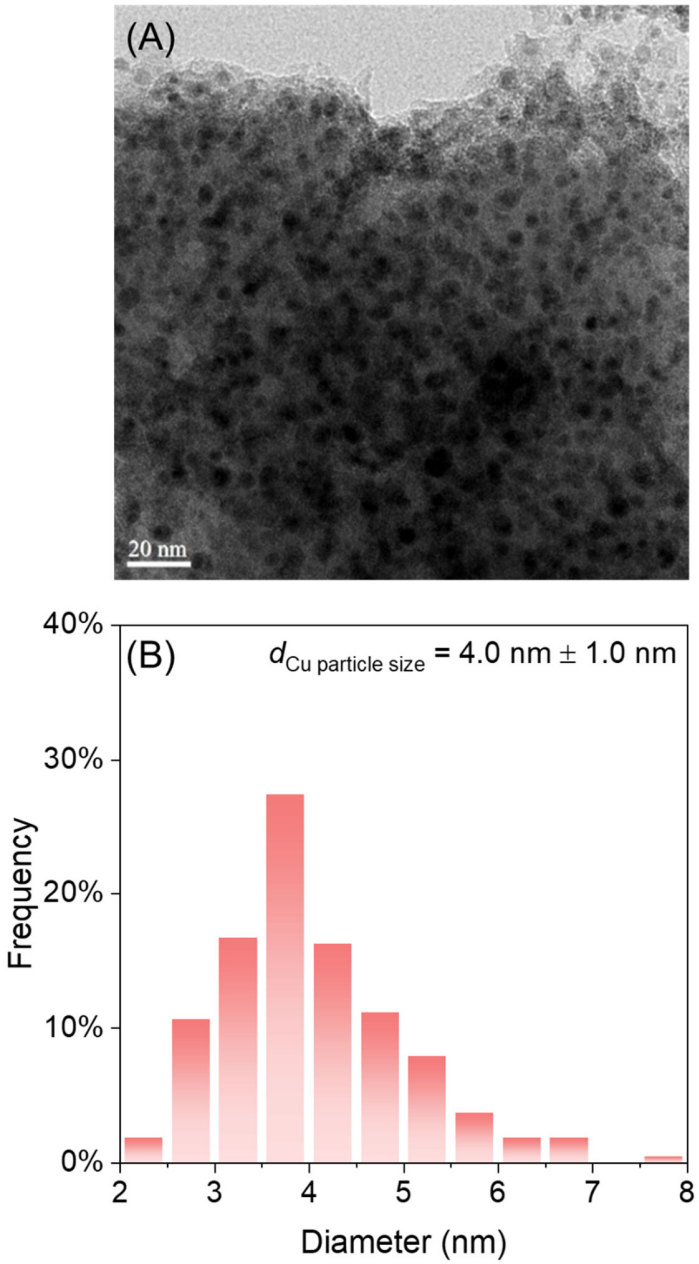

Fig. S25. (A) TEM image and (B) Cu NP size distribution of the spent Cu/Beta-deAl-18% catalyst after catalyzing the DMO hydrogenation at ambient pressure for 300 h.

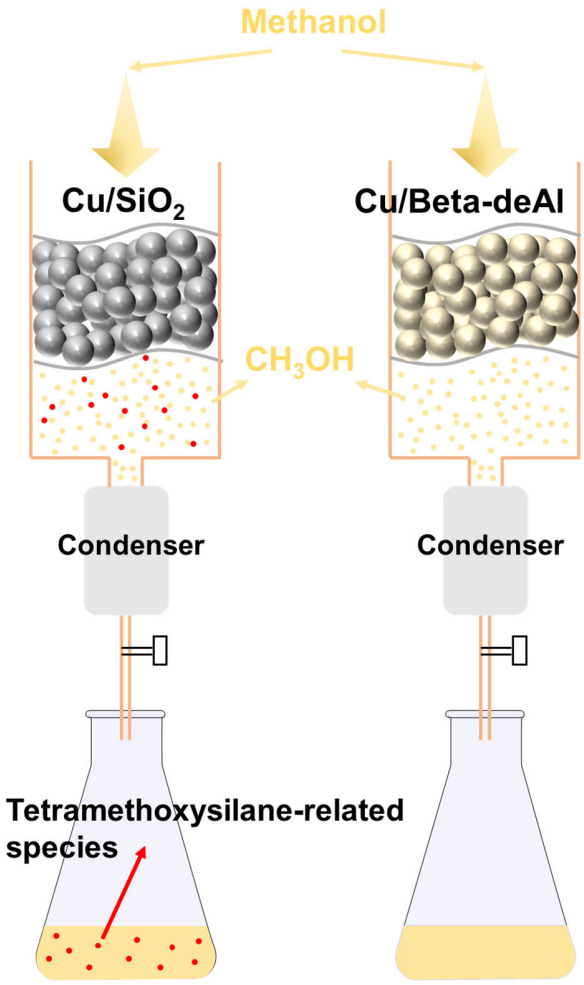

Fig. S26. Scheme showing the silica leaching from the amorphous silica (Cu/SiO_2) in methanol vapor at 200°C for 100 h, and the switched off silica leaching from the zeolite (Cu/Beta-deAl).

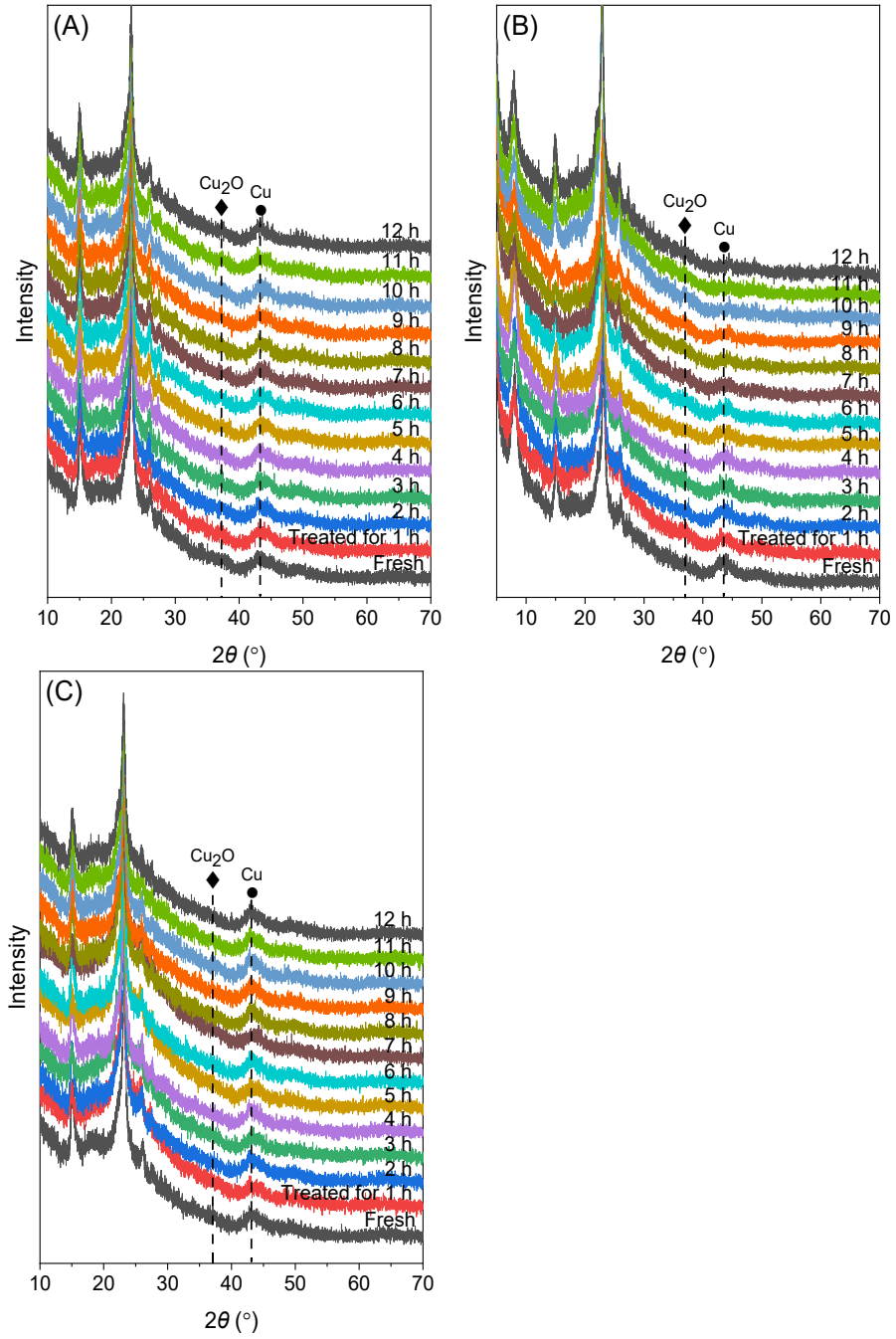

Fig. S27. In situ XRD patterns characterizing the Cu/Beta-deAl catalyst in the methanol treatment at (A) 100°C, (B) 300°C, and (C) 400°C for different periods.

Note: The Cu/Beta-deAl was treated in methanol vapor at 100°C, 200°C (fig. S5), 300°C, and 400°C to examine the effect of temperature on changing Cu particles on the Beta-deAl zeolite. The intensity of peaks at 43.3° and 36.5°, which are assigned to the diffractions of metallic Cu and Cu_2O phases (*31, 32*), were almost not changed at 100°C for 12 h (fig. S27A). However, those

characteristic peaks of Cu species disappeared after treatment at 200°C for 12 h (fig. S5), and 300°C for 7 h (fig. S27B). Further raising the aging temperature to 400°C for 12 h, the peak was unchanged in the in situ XRD patterns (fig. S27C), resulting in the sample with comparable Cu NP sizes (~5.1 nm, fig. S28). This phenomenon indicates that the re-dispersion of Cu is suppressed at higher temperature.

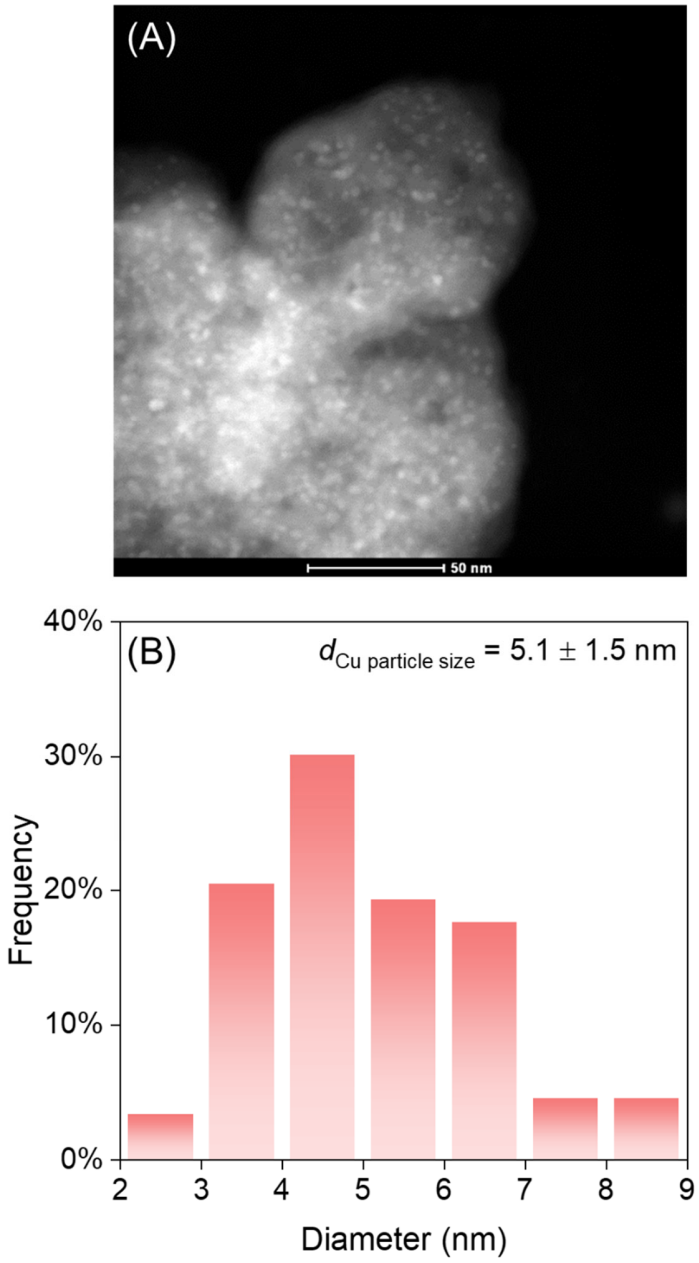

Fig. S28. (A) STEM image and (B) Cu NP size distribution of the Cu/Beta-deAl catalyst after the methanol treatment at 400°C for 12 h.

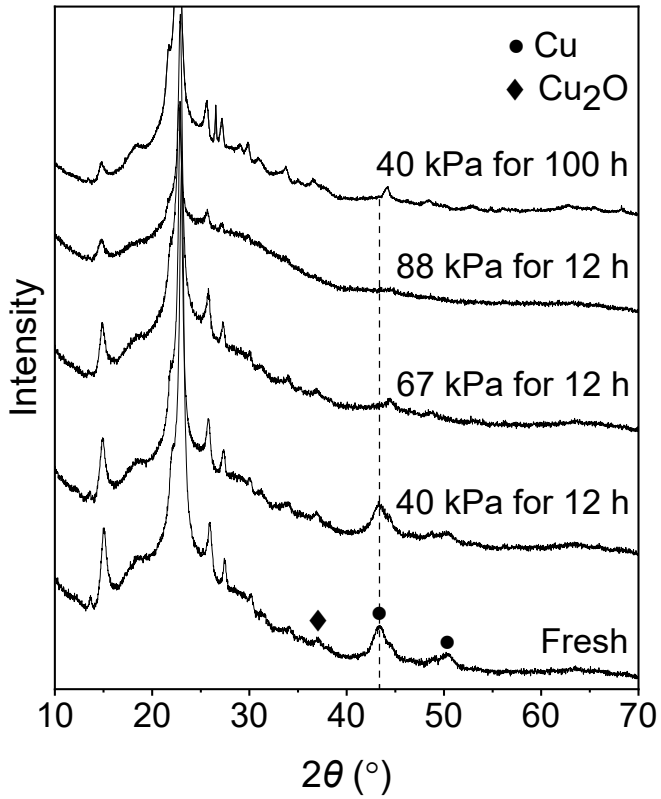

Fig. S29. XRD patterns characterizing the Cu/Beta-deAl samples after treatments with methanol under different partial pressures. The methanol partial pressure was adjusted by changing the feeding rate between 0.01 and 0.1 mL/min, and the treatment was conducted at 200°C for 12 h. The diffractions at about 26.5° and 68.4° were from the quartz sands which were used to dilute the catalyst in the fixed-bed reactor during the treatment.

Note: The concentration of methanol in the feed gas obviously influenced Cu re-dispersion. Cu re-dispersion on the Cu/Beta-deAl was extremely slow in the feed gas with methanol partial pressure at (~40 kPa, diluted with 10%H_2/90%N_2), as observed by the almost unchanged Cu diffraction in the XRD pattern after the treatment at 200°C for 12 h, and undetectable diffraction after 100 h. With raising partial pressure of methanol to 67 kPa, Cu re-dispersion occurred obviously, as observed with weak and broad Cu diffraction in the XRD pattern after treatment for 12 h. Further test with a high methanol partial pressure at 88 kPa led to undetectable diffraction of Cu in the XRD pattern after treatment for 12 h, confirming the high dispersion of Cu NPs.

We employed the XRD instrument with more sensitivity to characterize sample after treatment with 40 kPa of methanol after 100 h, compared with the instrument for other samples. In this case, the diffractions of Cu species were still undetectable, confirming the uniform dispersion. Simultaneously, the more-sensitive instrument gave a diffraction at 44.2° assigned to the Beta zeolite.

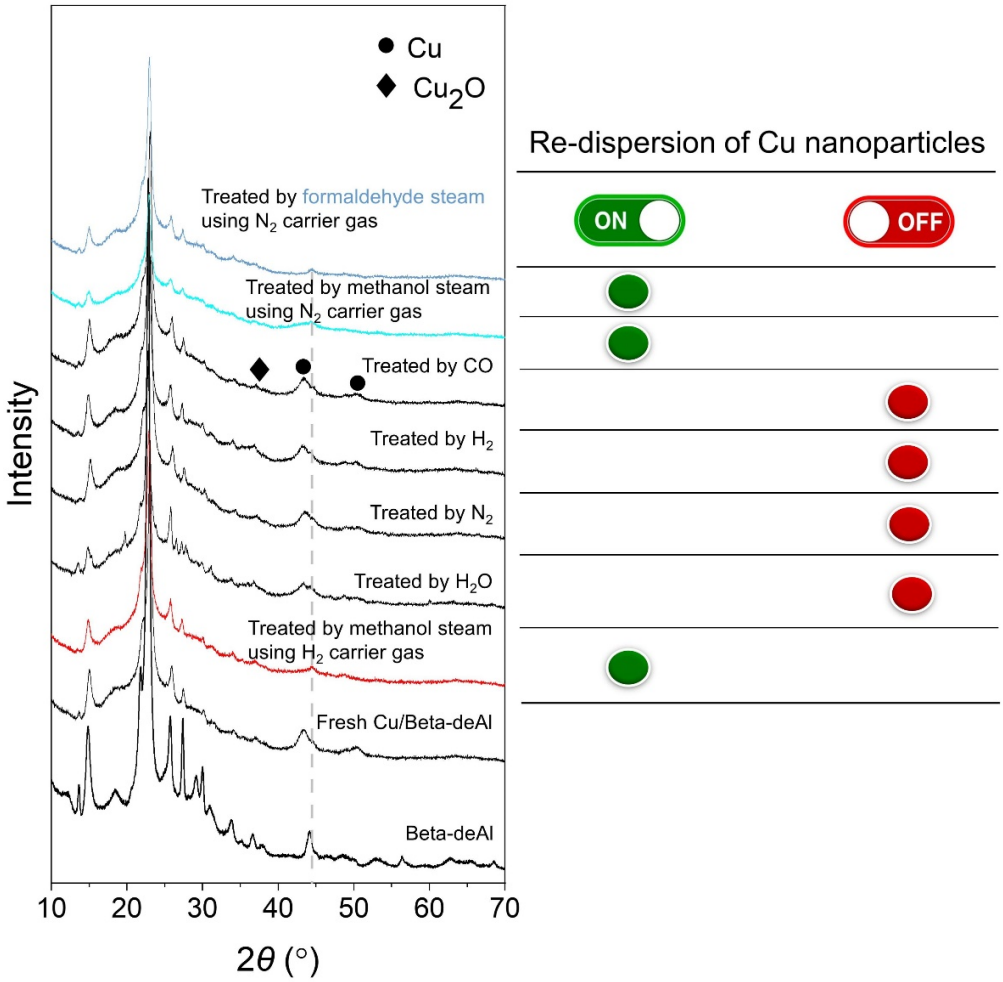

Fig. S30. XRD patterns of Cu/Beta-deAl catalyst after treatments at different conditions. The treatment was performed at 200°C for 12 h.

Note: The diffraction peaks of metallic Cu and Cu_2O were comparable before and after the treatment at 200°C for 12 h using different gases of water, N_2, H_2, and CO. TEM image also shows that the Cu particle size was almost unchanged (5.0-5.2 nm, fig. S31). Therefore, CO and H_2 from methanol decomposition are not responsible for the re-dispersion of Cu species.

In the methanol treatment, the re-dispersion of Cu NPs always occurred independent of carrier gas (methanol with H_2 or N_2). We further performed the treatment using formaldehyde vapor because dehydrogenation of methanol to formaldehyde easily occurred on Cu-based catalysts (*63*). The XRD pattern shows the disappearance of diffraction peaks of metallic Cu and Cu_2O phases on Cu/Beta-deAl after formaldehyde treatment at 200°C for 12 h, resulting in the sample with an average Cu NP size of 2.3 nm (fig. S33). The aforementioned results suggest that both methanol and formaldehyde are able to promote the re-dispersion of large Cu NPs into smaller ones.

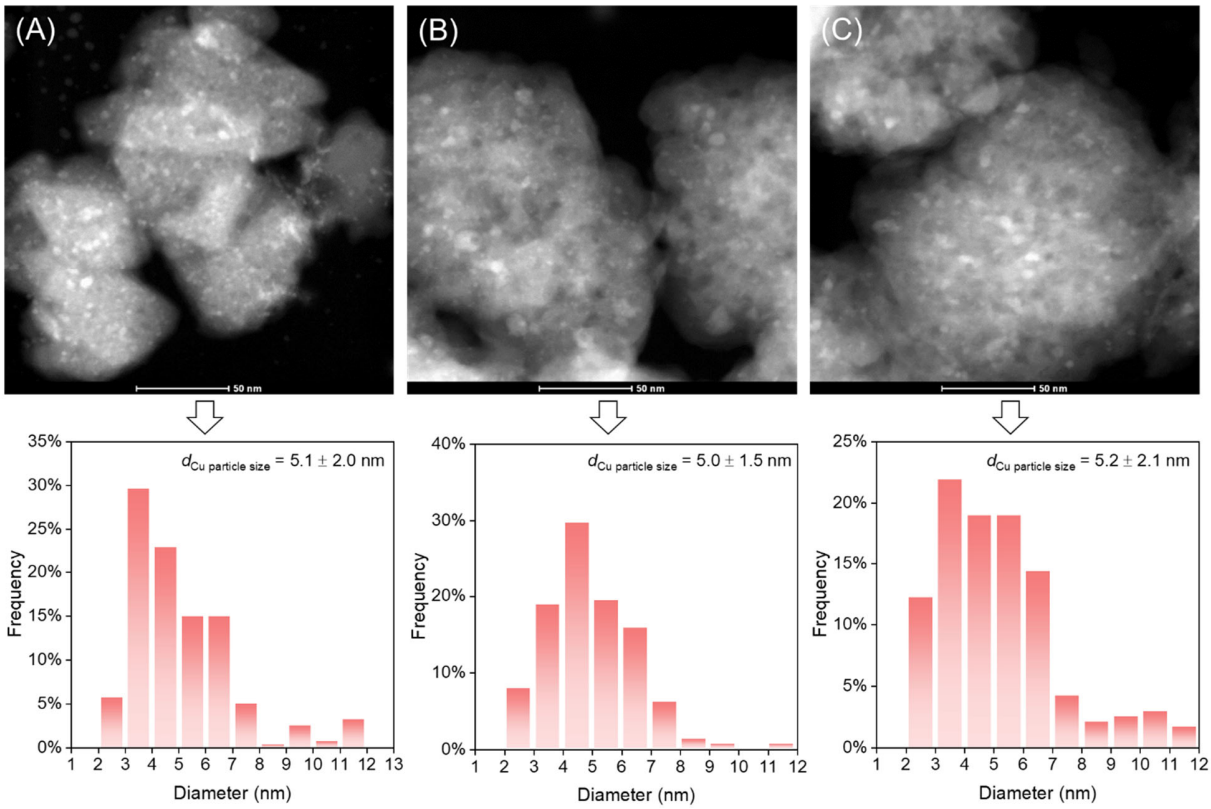

Fig. S31. TEM images and Cu NP size distributions of the Cu/Beta-deAl catalysts after treatment in different atmospheres of (A) water, (B) N_2, and (C) CO.

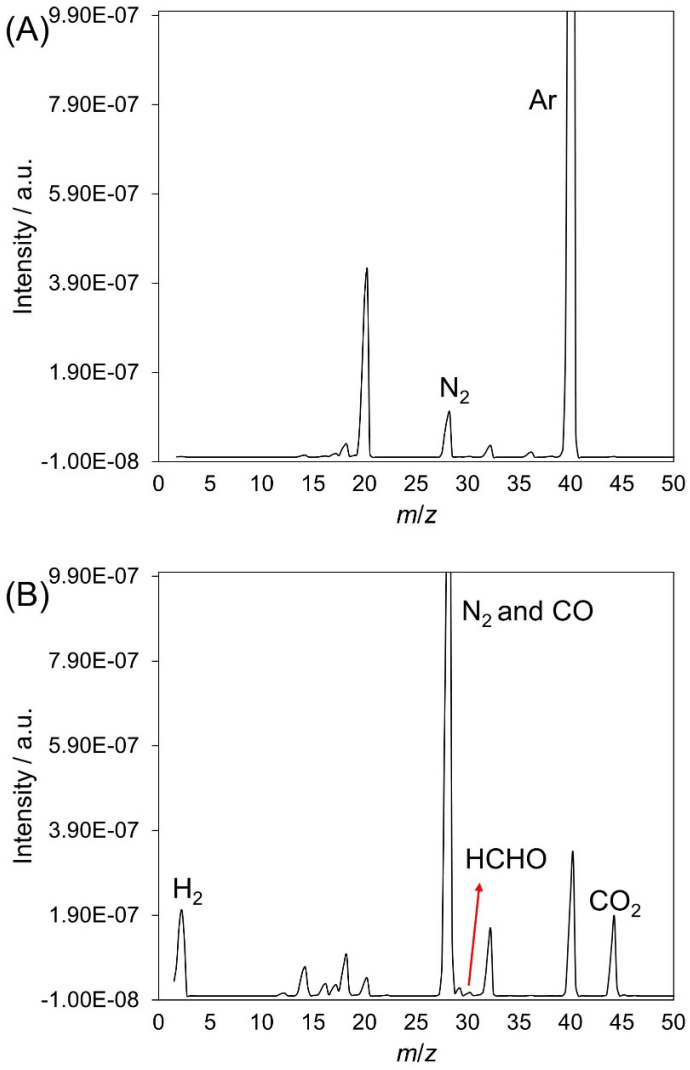

Fig. S32. Mass spectrum for (A) background, and (B) gaseous products for catalyst after the methanol treatment.

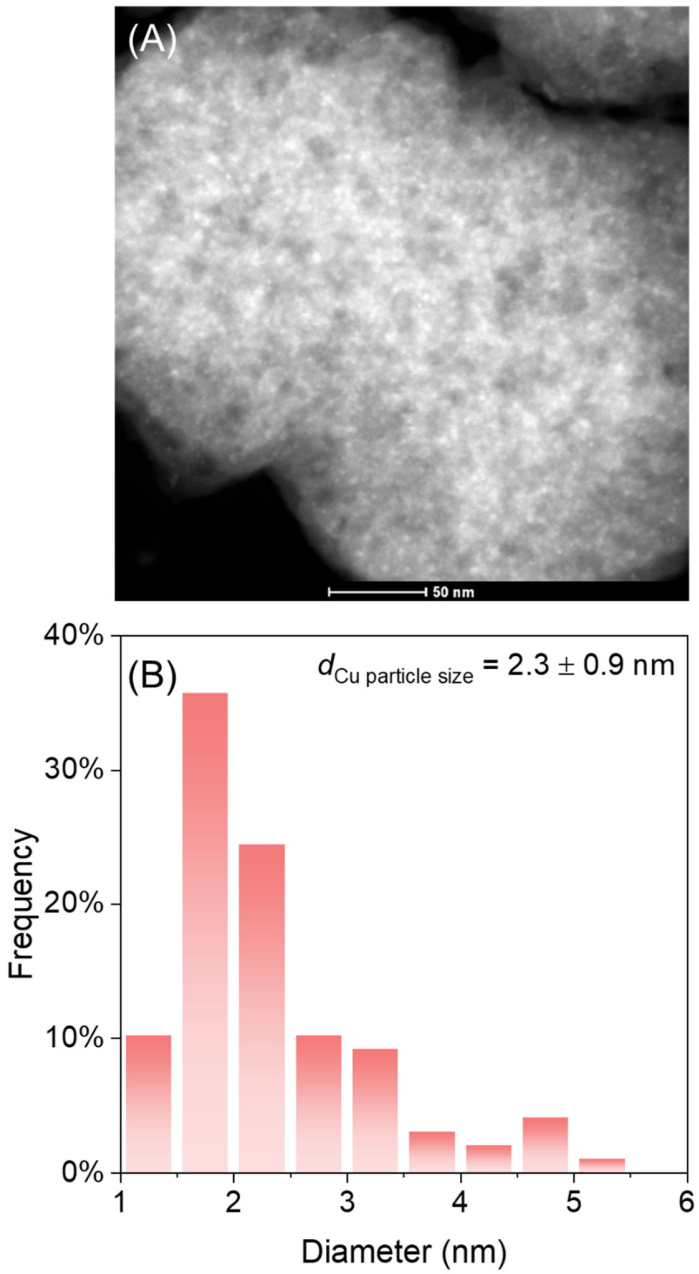

Fig. S33. (A) TEM image and (B) Cu NP size distribution of the Cu/Beta-deAl catalyst after formaldehyde treatment at 200°C for 12 h.

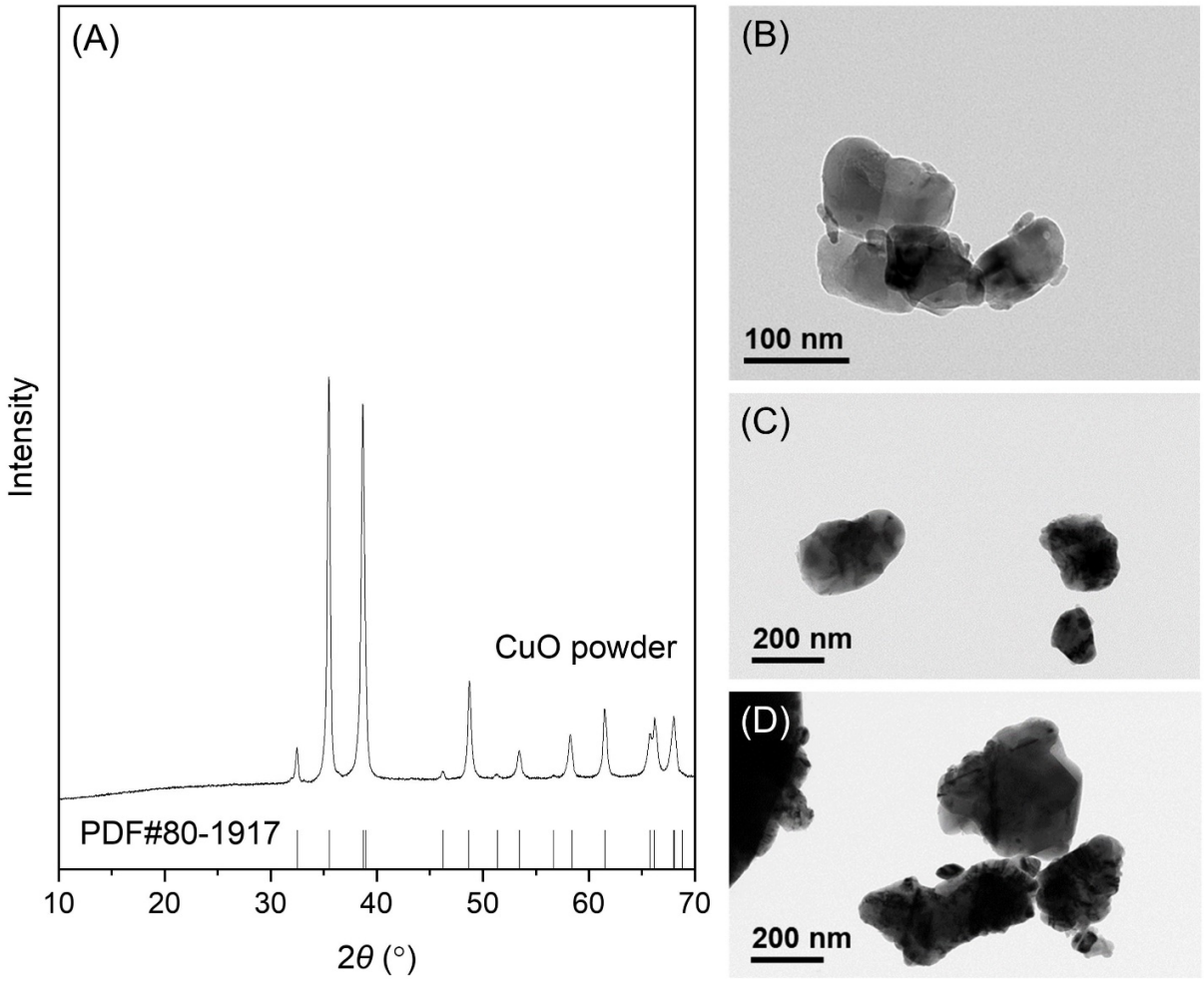

Fig. S34. (A) XRD pattern and (B-D) TEM images of commercial CuO powder. The CuO powder has a size distribution at 15-250 nm.

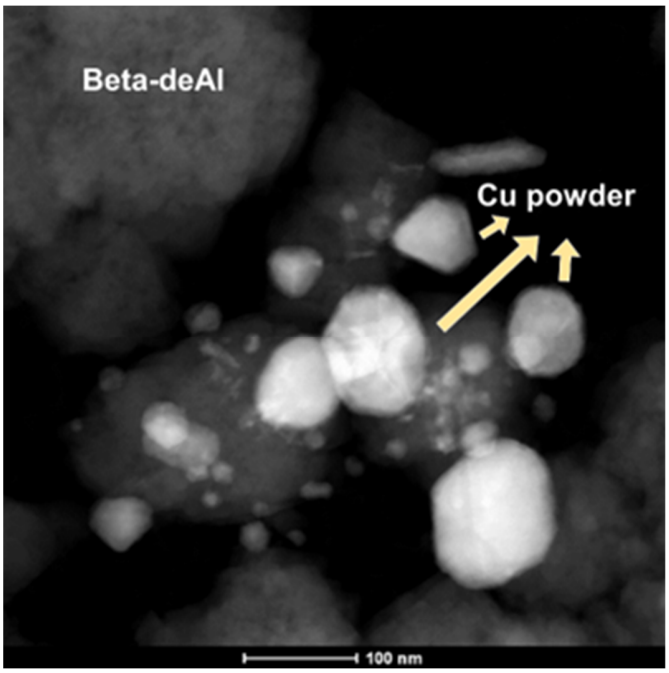

Fig. S35. STEM image characterizing the physical mixture of Cu powder (pre-reduction of the commercial CuO with hydrogen) and Beta-deAl.

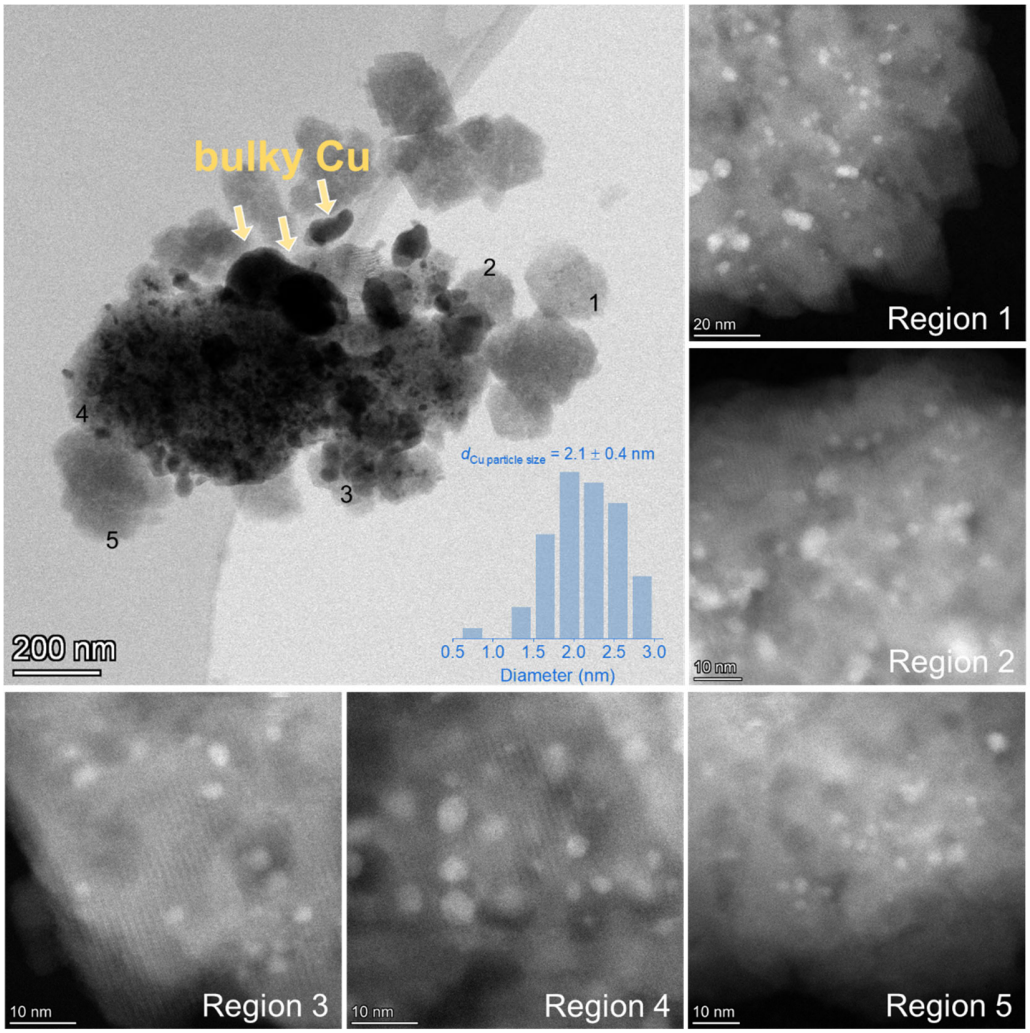

Fig. S36. TEM and STEM images characterizing the mixture of commercial Cu powder and Beta-deAl after the methanol treatment at 200°C for 5 h.

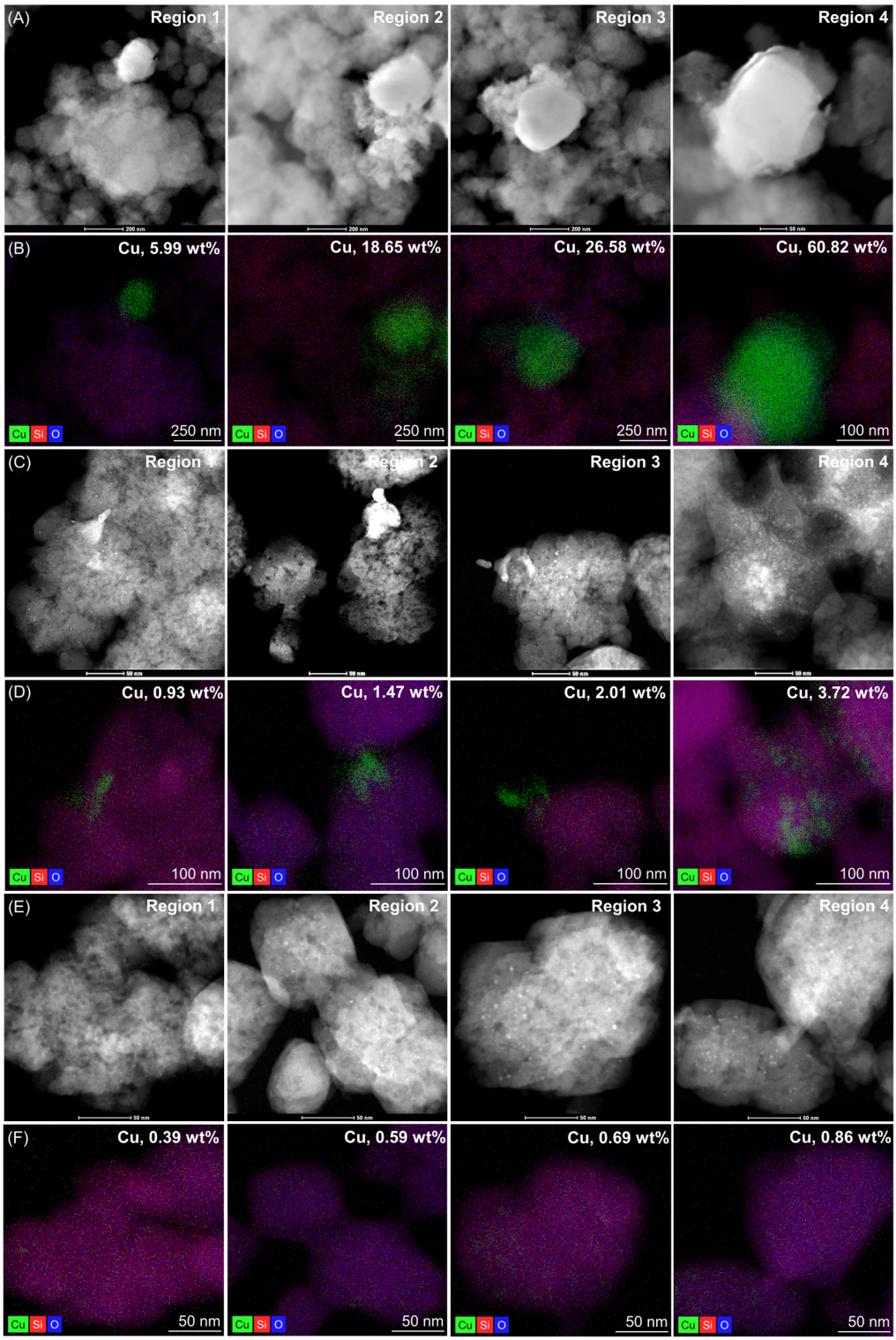

Fig. S37. STEM images characterizing the mixture of Cu powder and Beta-deAl zeolite during the methanol treatment at 200°C for (A) 0 h (fresh sample), (C) 70 h, and (E) 190 h. (B, D, and F) The corresponding EDS elemental maps and Cu contents by EDS analysis.

Note: We have characterized different regions on the mixture of Cu powder and Beta-deAl zeolite (weight fraction of Cu to zeolite at 0.48 wt%) by STEM and EDS during the methanol treatment at 200°C for different periods. The STEM images of different regions on the fresh mixture were shown in fig. S37A, where the bulky Cu particles were observed with undetectable small Cu NPs. EDS analysis of these regions with Cu particles gave varied values at 5.99 to 60.82 wt% (fig. S37B), suggesting the non-uniform dispersion of Cu because only bulky Cu particles existed. After methanol treatment for 70 h, the bulky Cu became smaller with the formation of abundant small-size Cu NPs on the Beta-deAl support (fig. S37C), and the Cu contents were from 0.93 to 3.72 wt% in different regions (fig. S37D), suggesting more uniform dispersion of Cu than that of the fresh Cu-zeolite mixture. Further prolonging the treatment to 190 h, a great number of small-size Cu NPs on the Beta-deAl support were observed whereas the bulky Cu was not detected in these regions (fig. S37E). The EDS analysis of the different regions showed comparable Cu contents at 0.39-0.86 wt% (fig. S37F), realizing a uniform Cu dispersion.

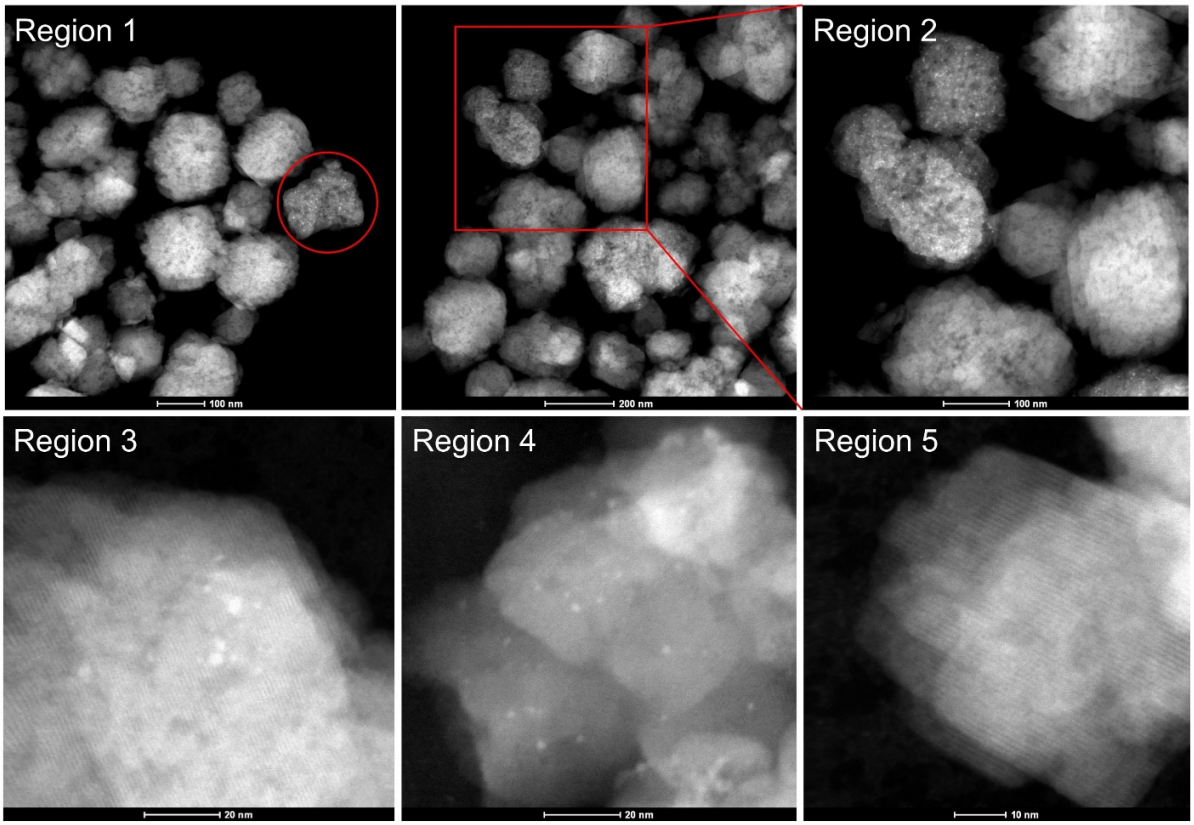

Fig. S38. STEM images characterizing the mixture of Cu powder and Beta-deAl after the methanol treatment at 200°C for 190 h. Regions different from Fig. 3F were characterized.

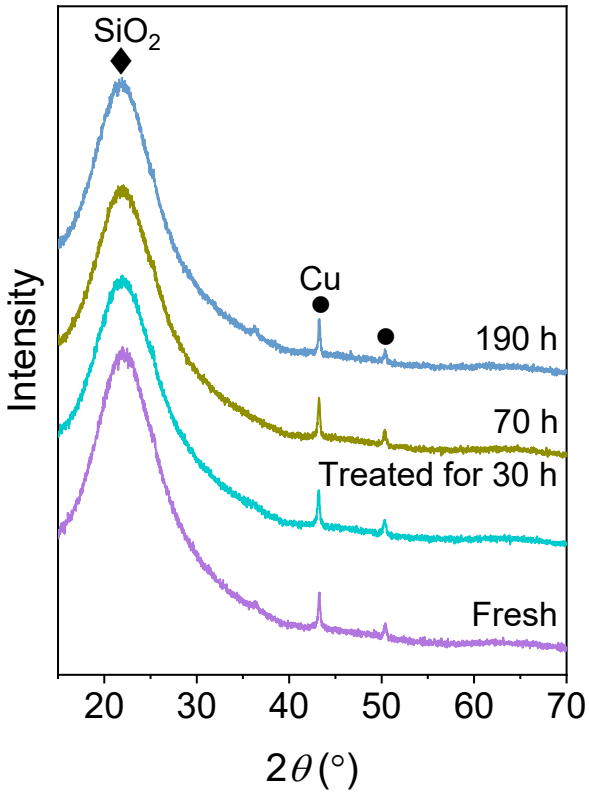

Fig. S39. XRD patterns characterizing the mixture of Cu powder and SiO_2 after the methanol treatment at 200°C for different periods.

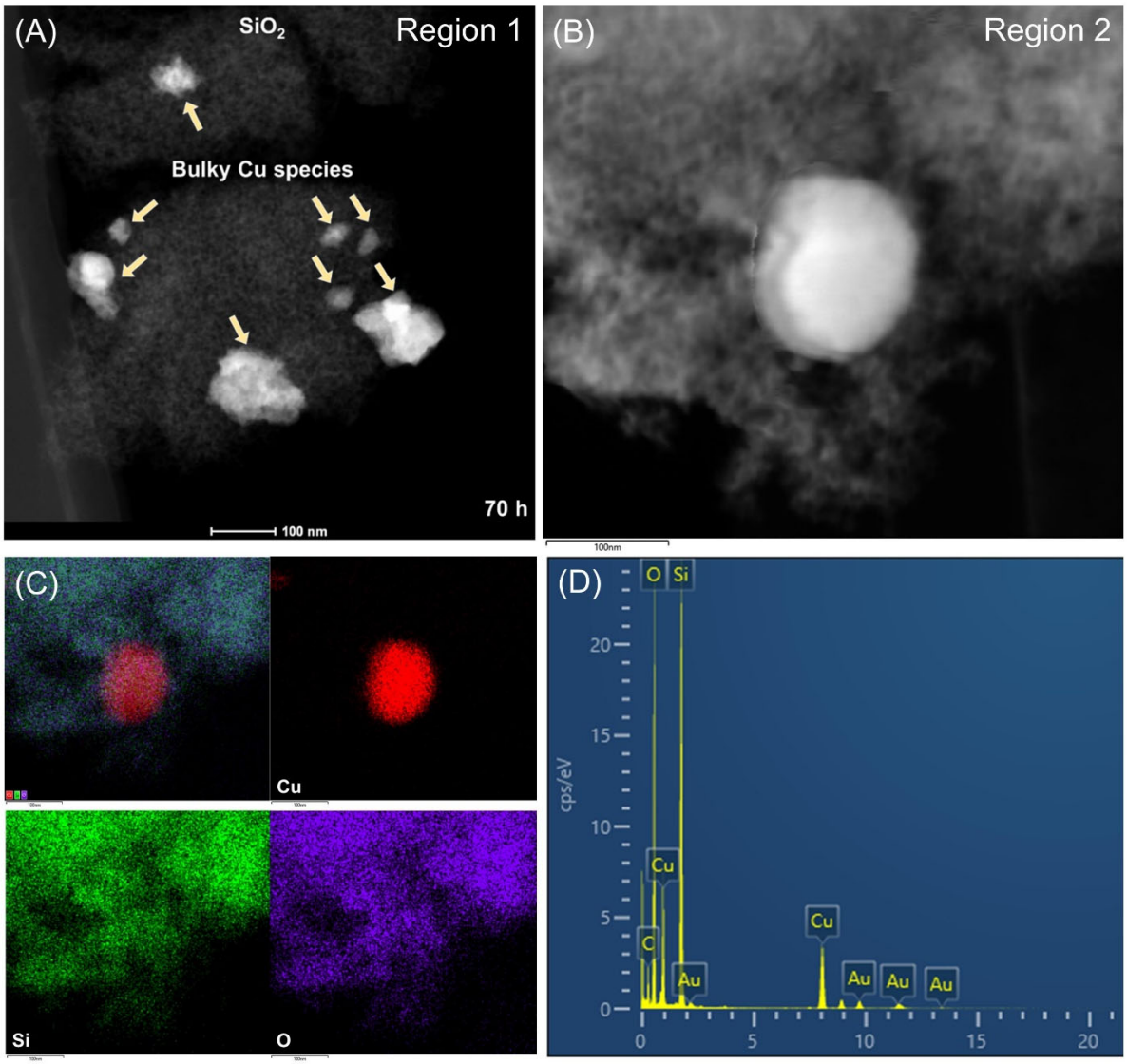

Fig. S40. STEM images and EDS elemental analysis of Cu powder physically mixed with SiO_2 after treatment by methanol at 200°C for 12 h. As observed in the images and elemental maps of the sample, it was not found the small-size Cu NPs, which might suggest that the partial etching of the large Cu particles does not occur.

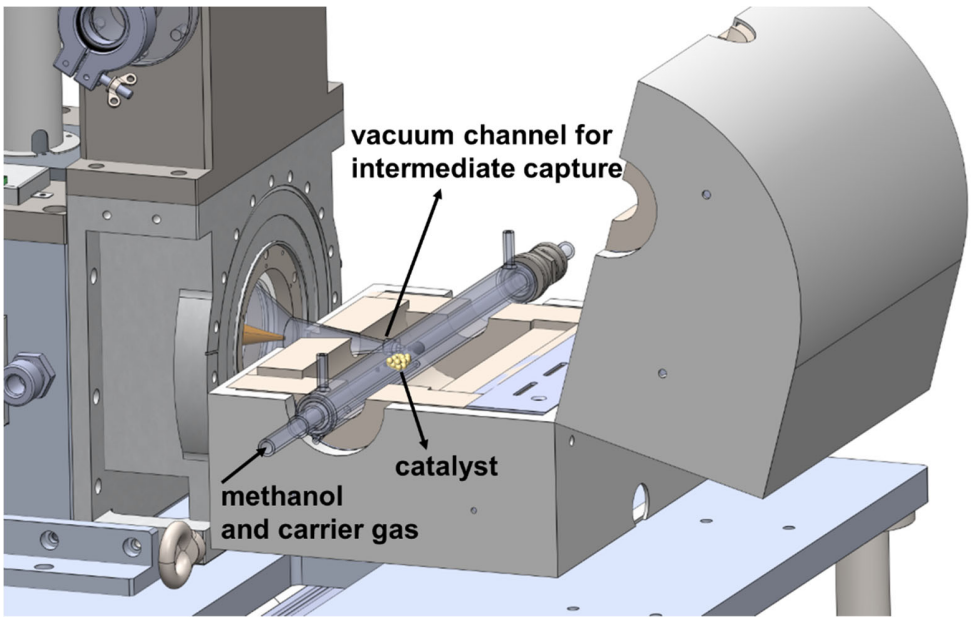

Fig. S41. The SVUV-PIMS for the analysis of possible intermediates in methanol vapor.

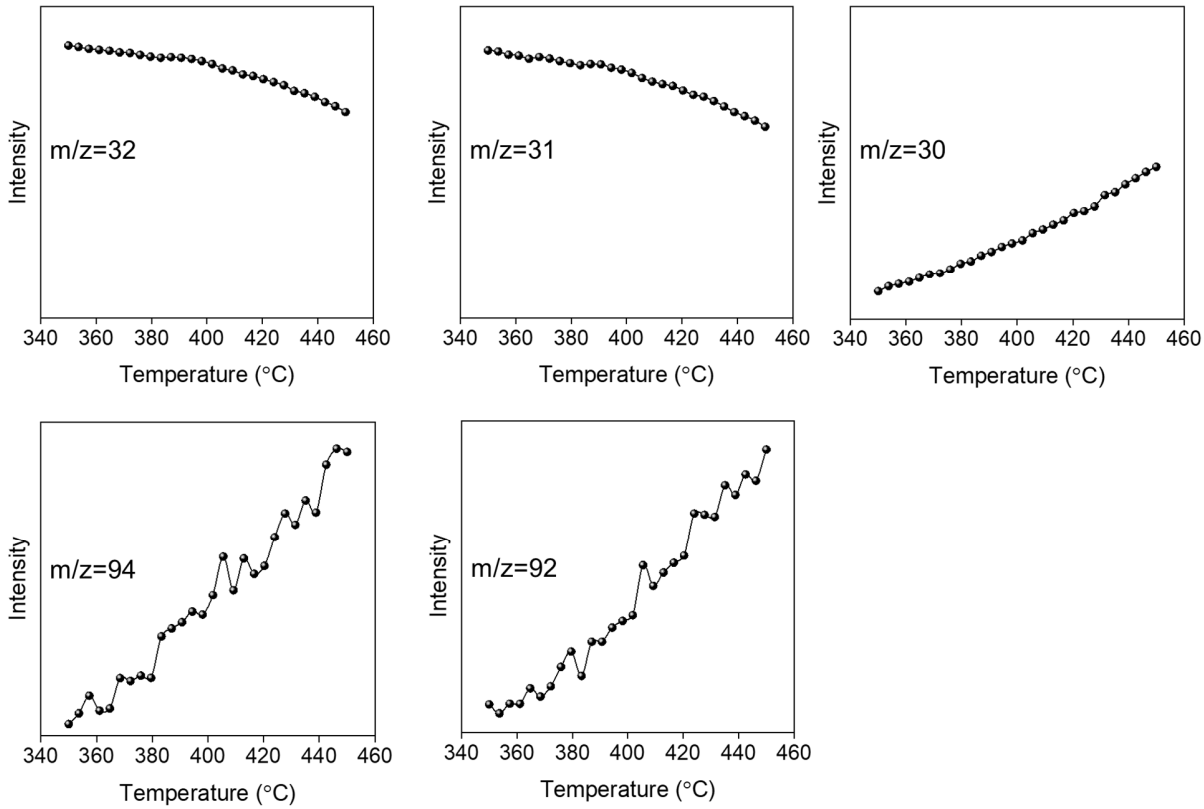

Fig. S42. Data showing the signal intensity in the SVUV-PIMS tests of the methanol treatment to Cu powder and Beta-deAl mixture as a function of temperature.

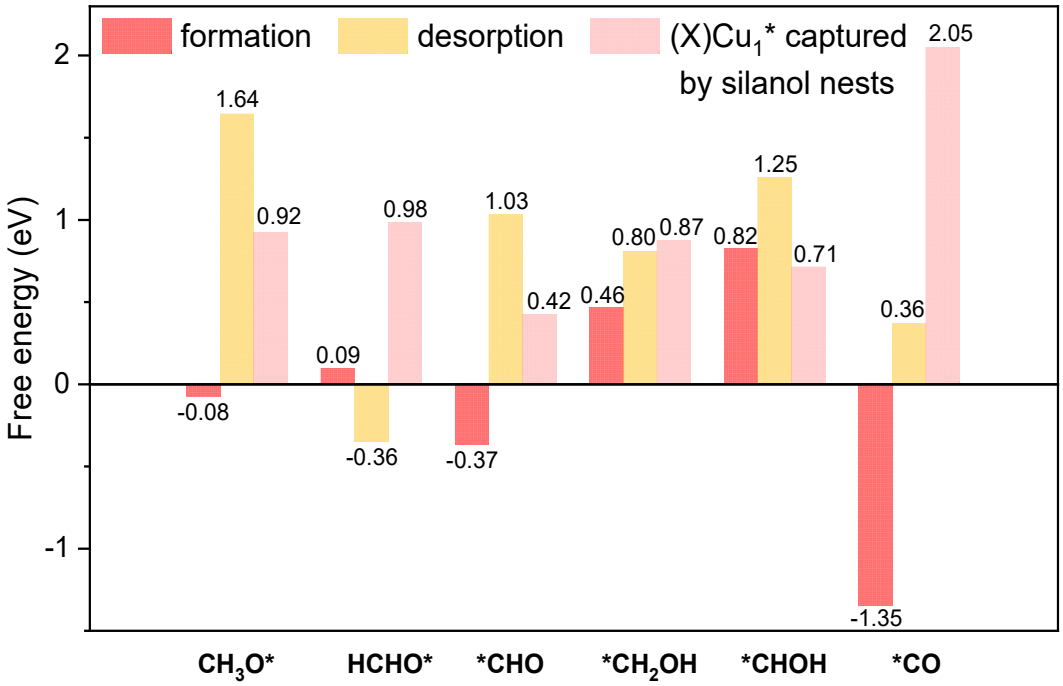

Fig. S43. Free energy of $C_xH_yO_z$ intermediates (X) formation, desorption from Cu cluster (Cu_{13} cluster), and the corresponding Cu_1 intermediates (X)Cu_1* captured by silanol nests (from adsorption state to one of the hydroxyl oxygens in the silanol nests with (X)Cu_1*).

Note: Although the (CHOH)Cu_1* has relatively lower energy input for the Cu detaching than the ligand desorption, it still cannot be considered as the intermediate for the reverse ripening because of relatively high energy input for the *CHOH formation.

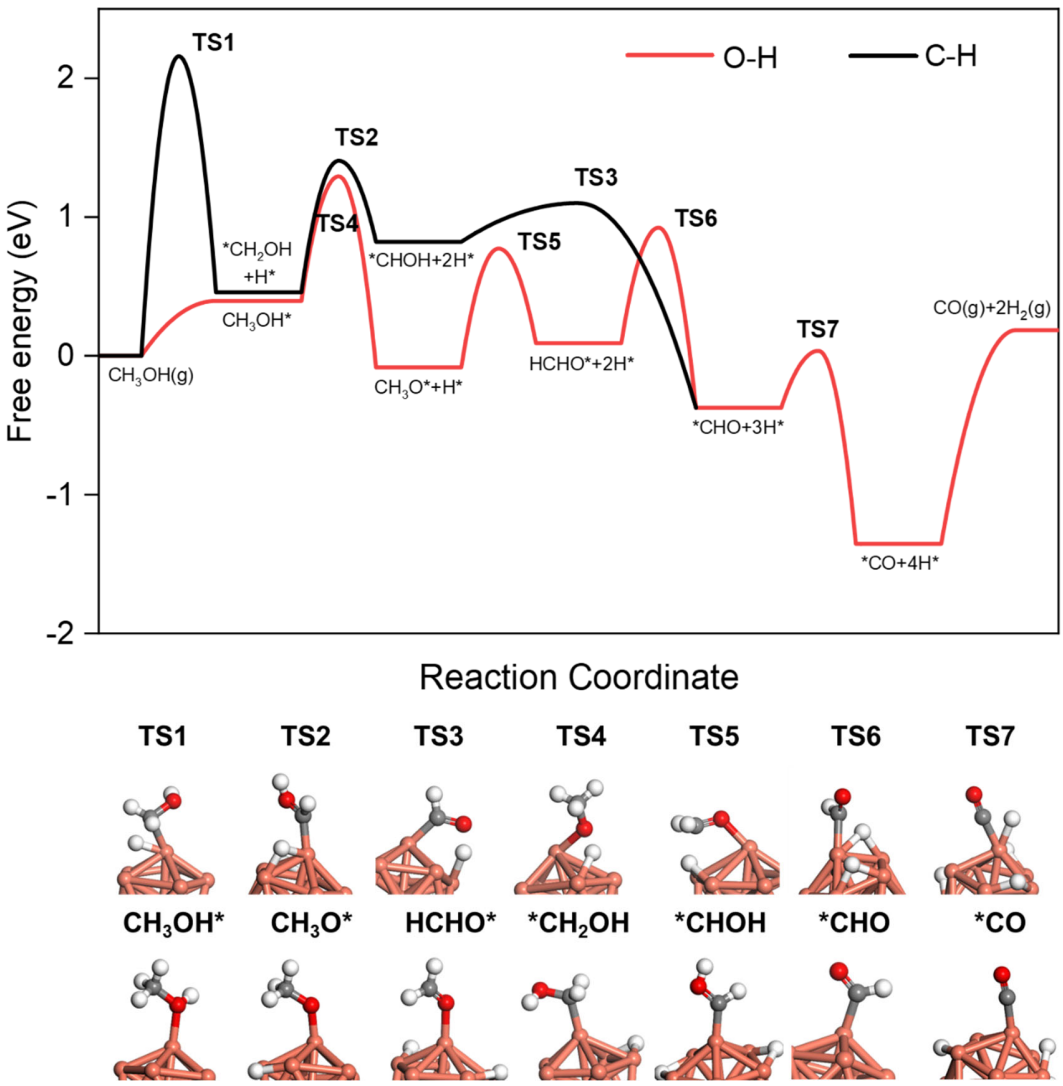

Fig. S44. Energy profiles of the methanol decomposition over the Cu/Beta-deAl.

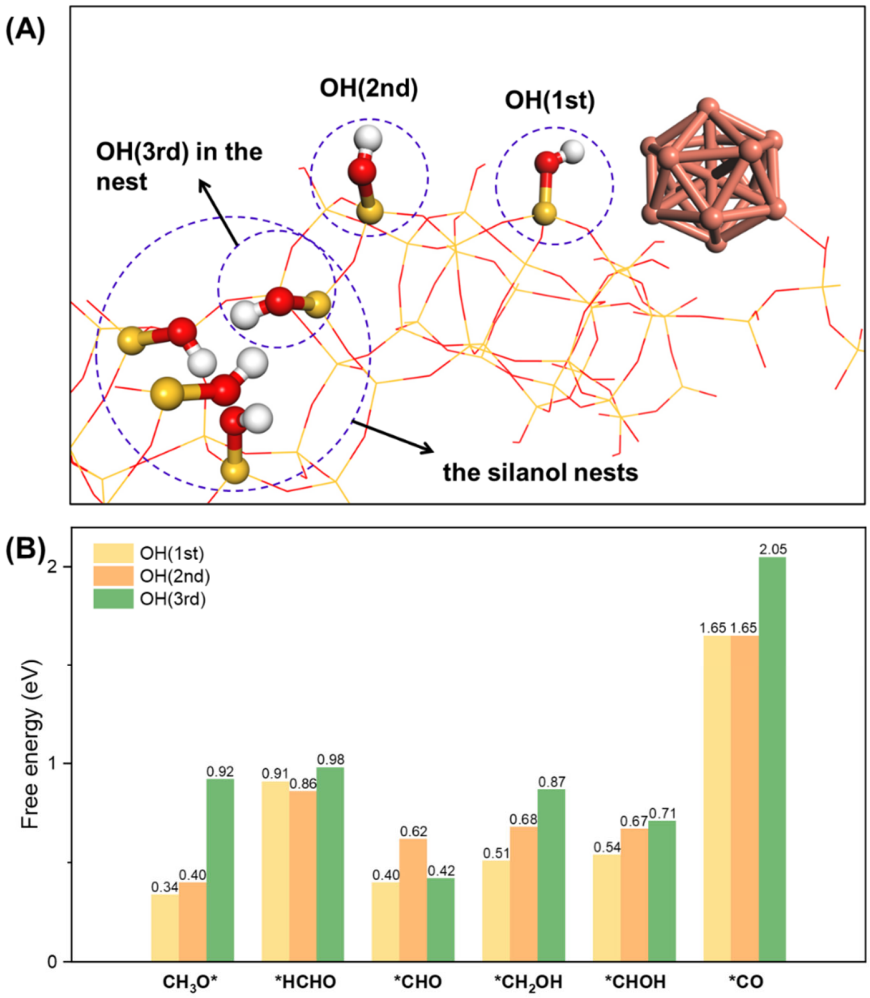

Fig. S45. (A) Schematic illustration of the hydroxyls and the silanol nests on Cu/Beta-deAl. (B) Free energy changes of (X)Cu_1* migration from Cu cluster to different hydroxyl sites.

Note: The hydroxyls of OH(1st) and OH(2nd) are the terminal OH groups, and OH(3rd) refers to the hydroxyls at the silanol nests (fig. S45A). The free energy change in each column (fig. S45B) is the accumulated migration energy from Cu cluster to the specified hydroxyl site, e.g. 0.4 eV of OH (2nd) in CH_3O* referring to the energy required for (CH_3O)Cu_1* migration to OH(2nd) which includes the energy change for (CH_3O)Cu_1* migration to OH(1st).

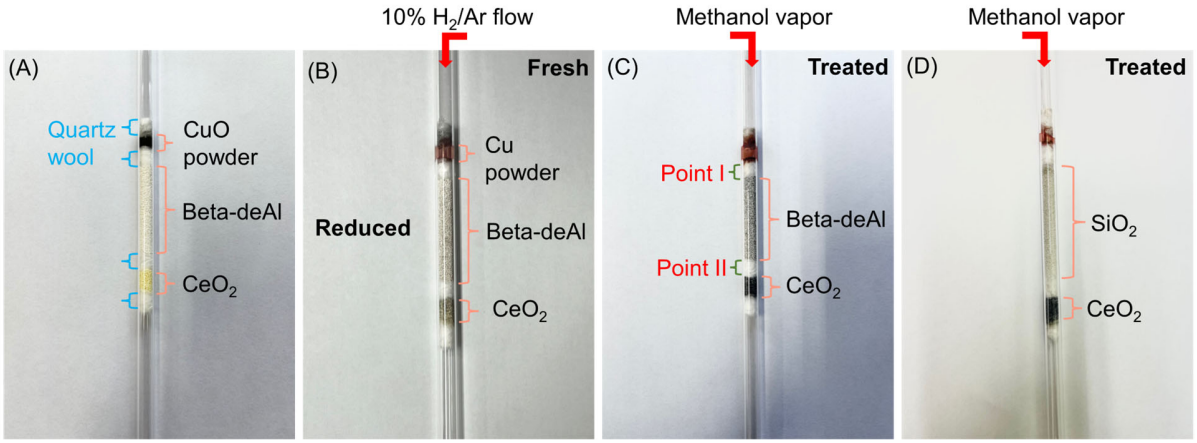

Fig. S46. Experimental setup for studying the gas-phase migration of Cu species over (A) a mixture of CuO powder, Beta-deAl, and CeO_2 across a fixed-bed reactor of quartz wool, (B) mixed beds after reduction at 400°C for 2 h by 10% H_2/Ar flow, and (C and D) mixed beds after reduction and methanol vapor treatment. Methanol treatment was performed at 400°C for 12 h at a methanol feeding rate of 0.1 mL_{liquid}/min using 10% H_2/Ar as carrier gas. The amount of CuO powder, Beta-deAl (or SiO_2), and CeO_2 was 0.2, 0.5, and 0.5 g, respectively.

Note: Inspired by the work (*64*), we rationally designed an experiment to study the gas-phase Cu migration and assess the migrated Cu amount with excluding the surface migration. As shown in fig. S46A, the CuO and Beta-deAl zeolite were localized in the fixed-bed reactor, which are spatially separated by quartz wool to exclude the surface migration. It is expected that the Cu_1 intermediates would transfer with the assistance of methanol vapor and be captured by the Beta-deAl zeolite. After the Beta-deAl bed, we placed a bed with CeO_2, a reducible oxide strongly interacted with metal species (*8, 9, 21*), to capture the residue Cu species in methanol vapor that were not fully captured by the zeolite. Based on the Cu contents on the Beta-deAl and CeO_2, the average Cu contents in methanol vapor before and after the Beta-deAl bed in the fixed-bed reactor could be obtained.

We characterized different regions on the Beta-deAl and CeO_2 by STEM and EDS after a pre-treatment with hydrogen flowing through the mixed beds at 400 °C for 2 h (fig. S46B), and both showed unobserved Cu NPs and undetectable Cu contents (fig. S47). These data suggest the negligible gas-phase Cu migration in H_2 atmosphere. After the treatment by methanol vapor at 400 °C for 12 h (a temperature of 400 °C, higher than the standard experiment, was employed to accelerate the gas-phase transport of Cu species), abundant Cu NPs were formed on the Beta-deAl zeolite as confirmed by the STEM images characterizing different regions (fig. S48A and B). The Cu contents in different regions of Beta-deAl varied from 0.17-1.57 wt% by EDS analysis (fig. S48C), which is reasonably due to the distinguishable Cu concentrations in the different regions of the zeolite bed by the methanol treatment. By ICP analysis, the average Cu content on the Beta-deAl was 1.04 wt%. On the CeO_2, the Cu species were also detected with contents at 0.65-1.06 wt% in different regions by EDS analysis (fig. S48D and E), and an average Cu content was at 0.80 wt% by ICP analysis.

Based on the amount of Beta-deAl (0.5 g) and CeO_2 (0.5 g) in the fixed bed reactor, we assessed the total amount of migrated Cu was 7.25 mg during the methanol treatment. Considering the gas feed at 25 mL/min, the average gas-phase Cu concentration before the Beta-deAl (Point I in the fixed-bed reactor, fig. S46C) was 7.99 $\mu mol_{Cu}/L$. After captured by zeolite, the average gas-phase Cu concentration was 3.47 $\mu mol_{Cu}/L$ (Point II in the fixed-bed reactor, fig. S46C).

In the equivalent test except using amorphous SiO_2 to replace Beta-deAl zeolite in the fixed-bed reactor (fig. S46D), the Cu content on SiO_2 was very limited (average Cu content <0.15 wt% by EDS, and 0.23 wt% by ICP, fig. S49A-C). The Cu content was 0.39-0.53 wt% on the CeO_2 by EDS analysis (fig. S49D and E) and 0.59 wt% by ICP analysis. These data corresponded to the average gas-phase Cu concentration at 3.56 $\mu mol_{Cu}/L$, while SiO_2 has less influence on the Cu concentration before and after the SiO_2 bed because of the extremely weak ability of SiO_2 for capturing Cu_1 intermediate.

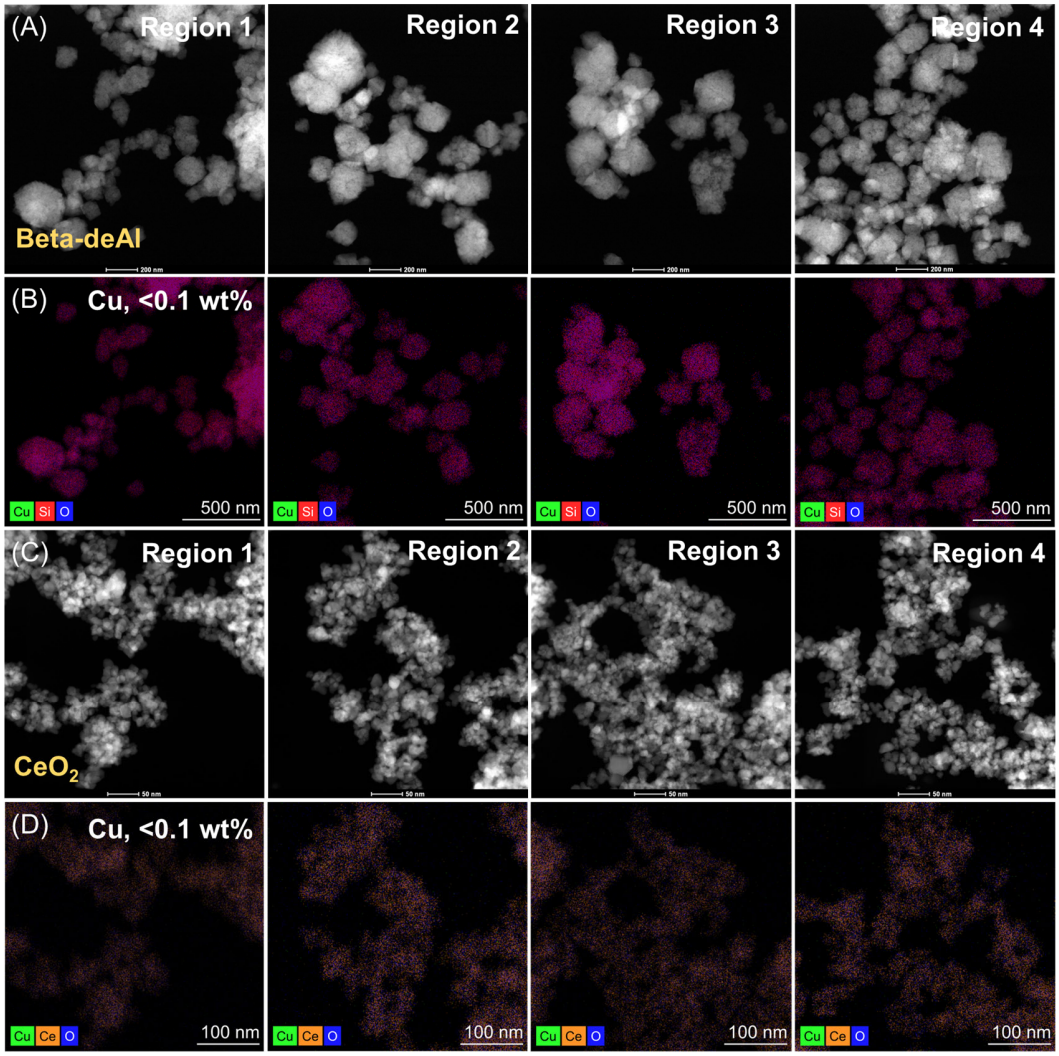

Fig. S47. STEM images characterizing different regions of fresh samples (the mixed beds after hydrogen treatment, corresponding to the experiment in fig. S46B). (A) Beta-deAl zeolite bed and (C) CeO_2 bed. (B and D) The corresponding EDS elemental maps and Cu contents by EDS analysis.

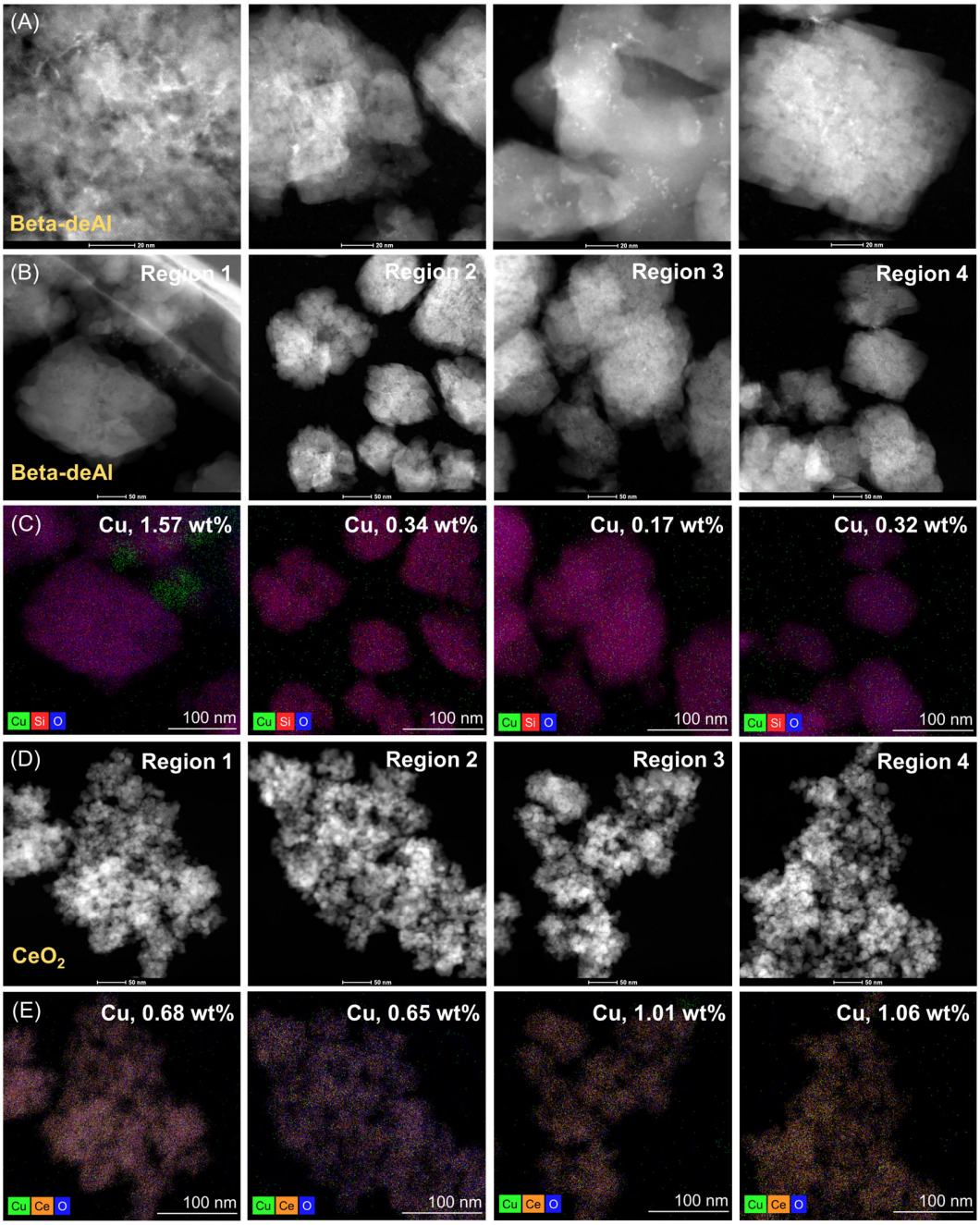

Fig. S48. STEM images characterizing different regions of methanol-treated samples (the mixed beds after methanol treatment, corresponding to the experiment in fig. S46C). (A and B) Beta-deAl zeolite bed and (D) CeO_2 bed. (C and E) The corresponding EDS elemental maps and Cu contents by EDS analysis.

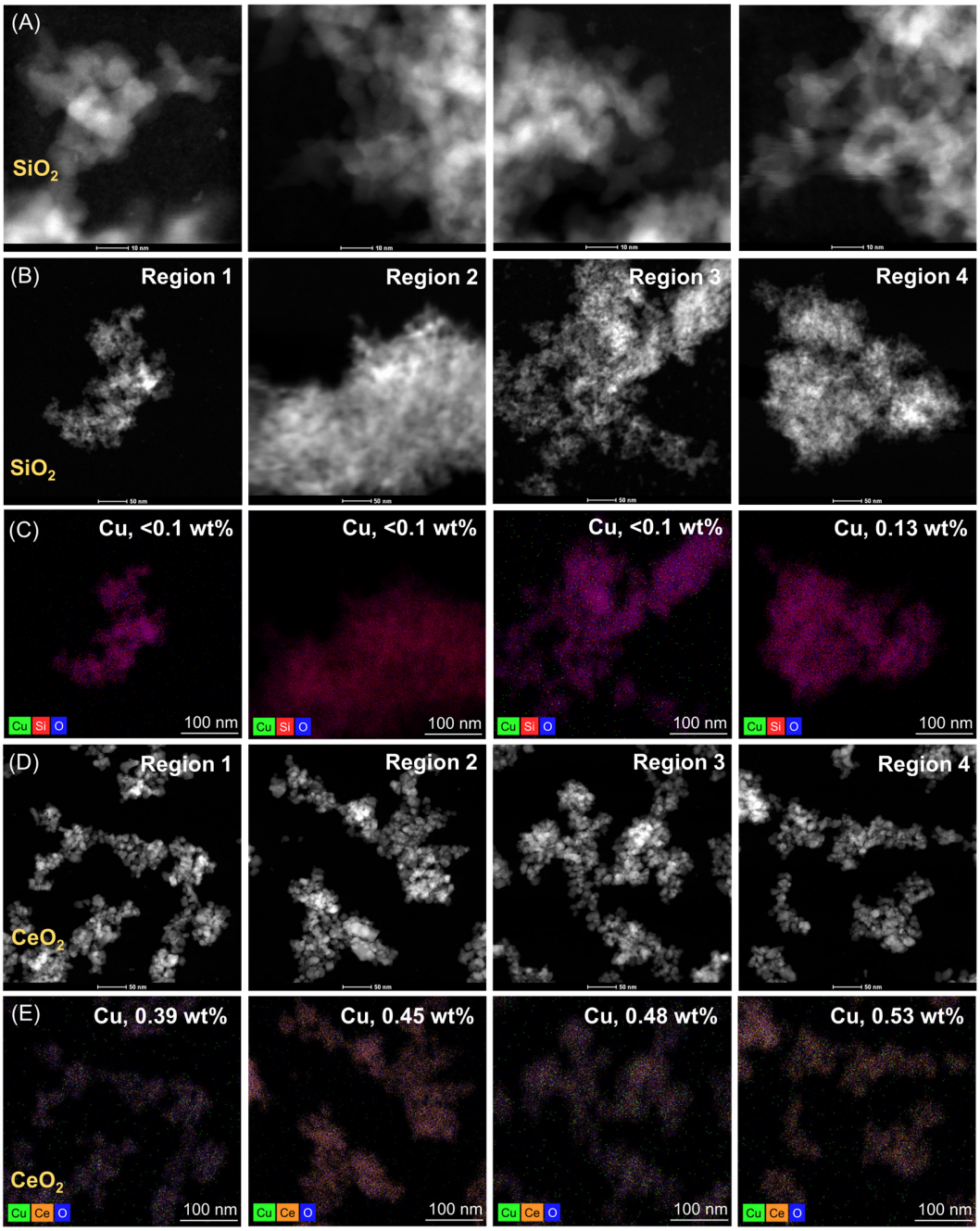

Fig. S49. STEM images characterizing different regions of methanol-treated samples (the mixed beds after methanol treatment, corresponding to the experiment in fig. S46D). (A and B) SiO_2 bed and (D) CeO_2 bed. (C and E) The corresponding EDS elemental maps and Cu contents by EDS analysis.

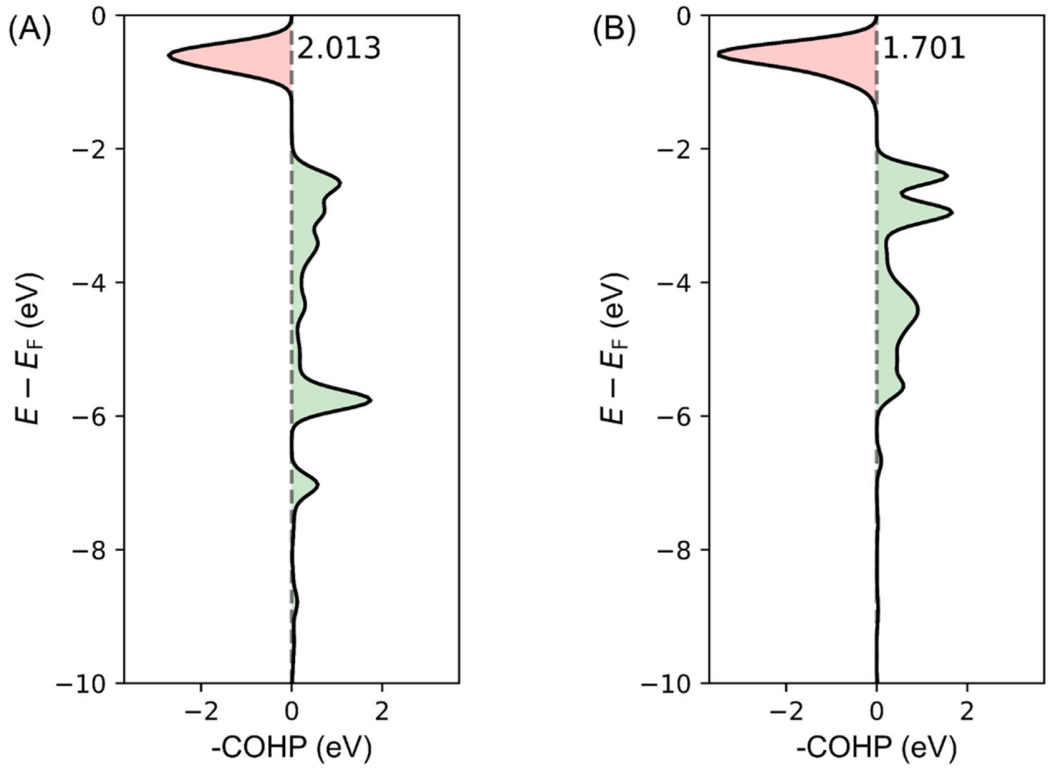

Fig. S50. The -COHP plot of (A) the Cu-O bond between Cu_1 and silanol nest site, (B) the Cu-O bond between Cu_1 and the SiO_2 surface. The -IpCOHP values are shown in the upper right corner of the plots.

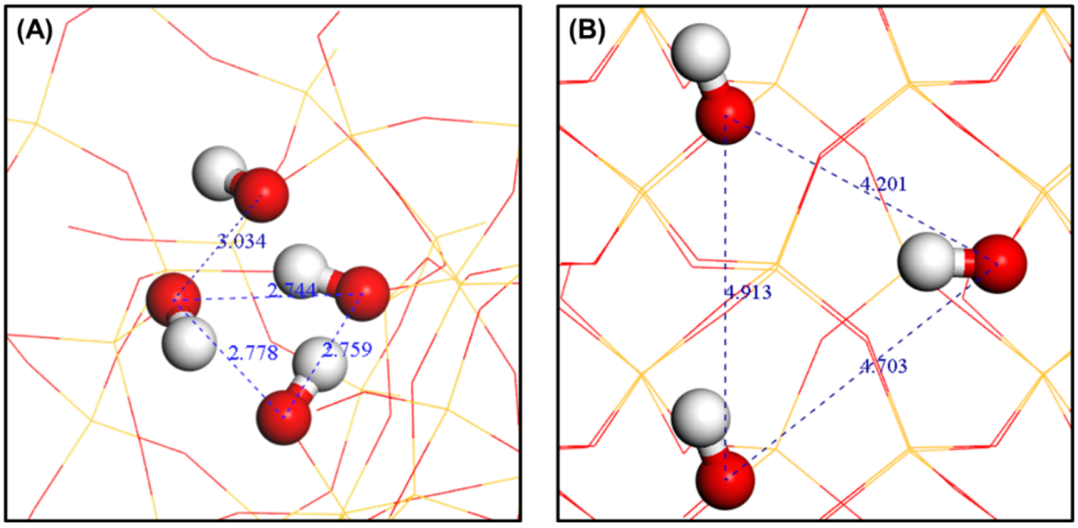

Fig. S51. Geometry structures of (A) the silanol nest sites and (B) the SiO_2 surface. The distances between the hydroxyl oxygen atoms (Å) are shown in blue dotted lines.

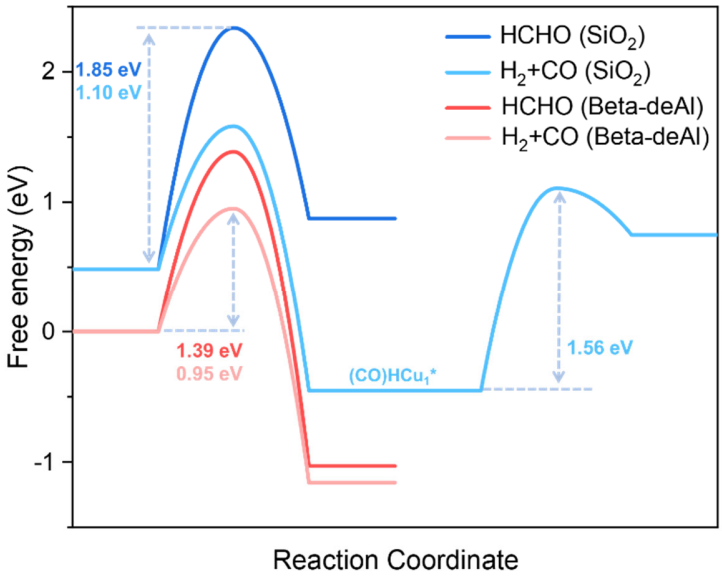

Fig. S52. The energy profiles for the different reaction pathways of (CHO)Cu_1* anchored at the silanol nest of the Beta-deAl and over the SiO_2(100) surface. (CO)HCu_1* was from dehydrogenation of (CHO)Cu_1*, and then it hydrogenated with the H atom on SiO_2 surface.

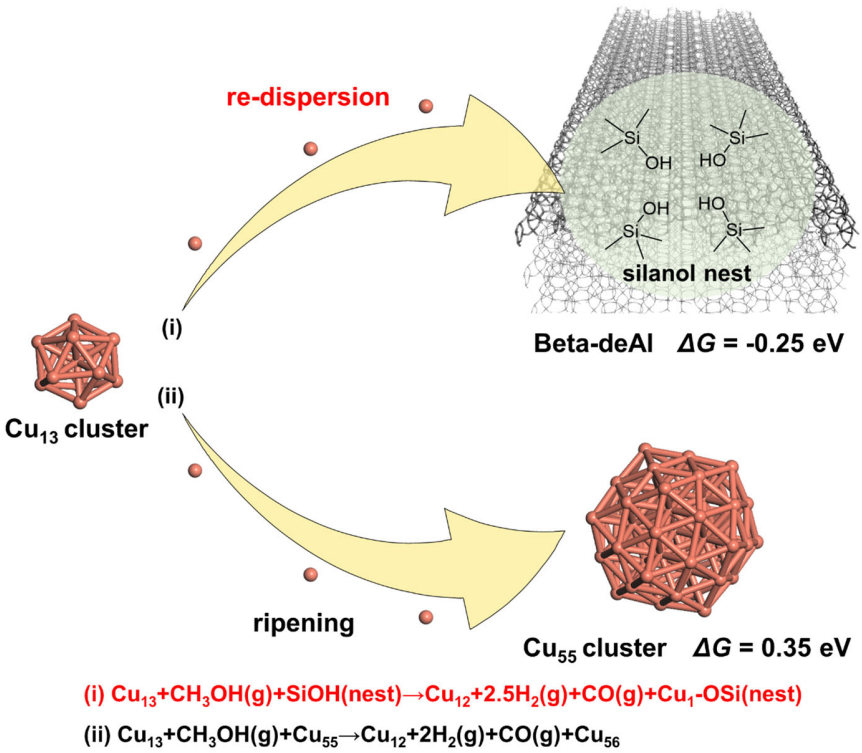

Fig. S53. Free energy changes for different routes with (CHO)Cu_1* captured by silanol nest and Cu_{55} cluster.

Note: We considered the Cu re-dispersion with formation of (CHO)Cu_1*, migration from the surface, and followed by being captured by (i) the silanol nests (Equation 1) and (ii) the Cu cluster (Cu_{55} as a model, Equation 2), respectively. Both routes showed similar energy barriers, but quite different free energy changes. The Cu sintering processes are endothermic with a standard free energy change at 0.35 eV for route (ii) with (CHO)Cu_1* being trapped by Cu_{55} cluster. In contrast, the route (i) with (CHO)Cu_1* being captured on silanol nest was exothermic with a free energy change at -0.25 eV and it remains exothermic with a free energy change at -0.27 eV when the fifth Cu atom is captured in the silanol nest. Therefore, the Cu re-dispersion was favorable relative to Cu sintering on the Beta-deAl support.

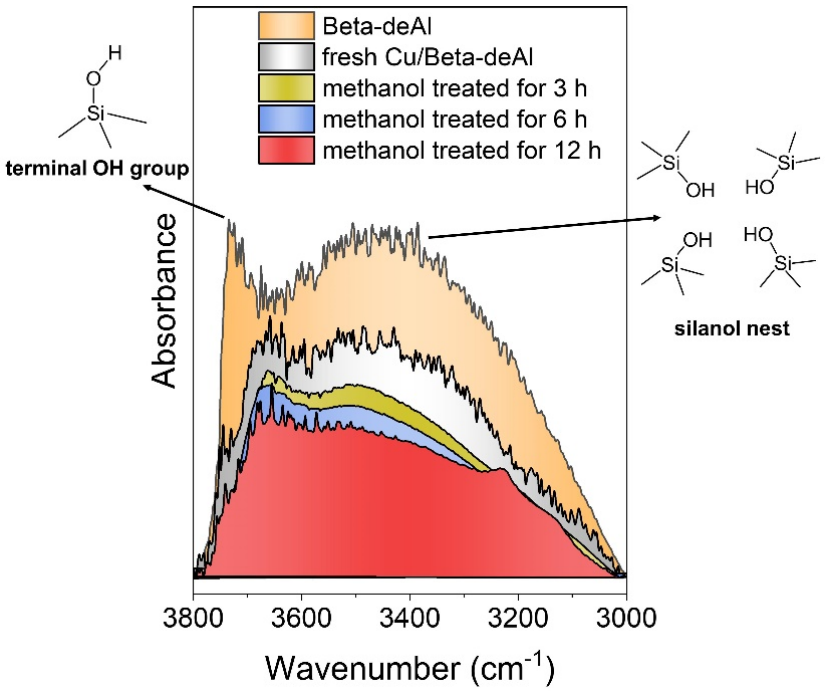

Fig. S54. FT-IR spectra of Cu/Beta-deAl (3.0 wt%) related samples under vacuum.

Note: The intensity of a broad band around 3500 cm^{-1} assigned to silanol nests (*50*) was gradually decreased, which corresponds to the partial consumption of silanol nests to capture Cu_I intermediates in the reverse ripening process.

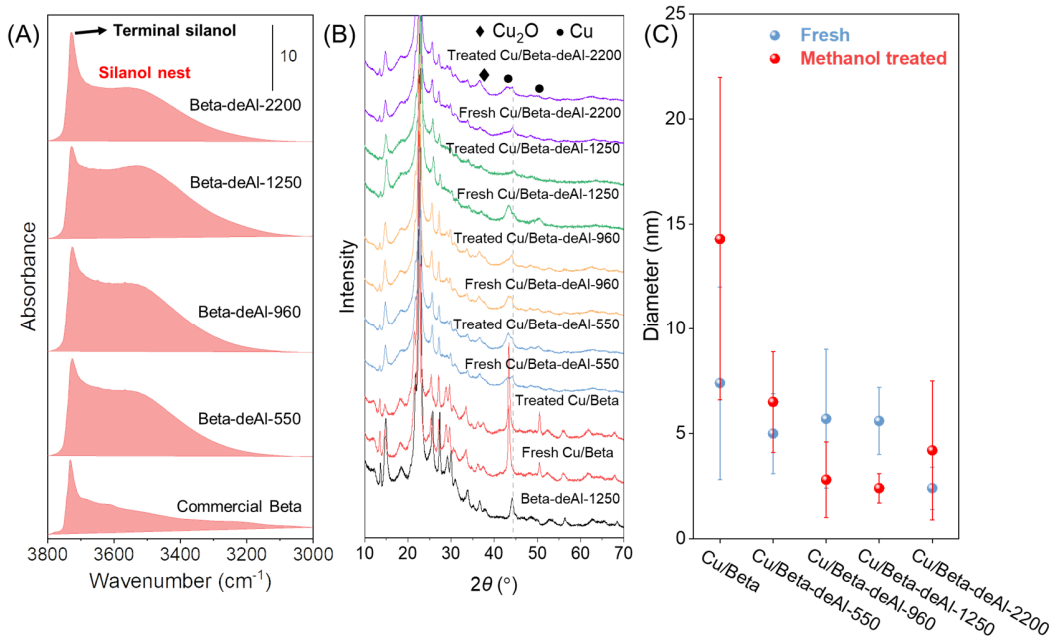

Fig. S55. (A) FT-IR spectra characterizing the silanols in Beta zeolites with different Si/Al ratios, (B) XRD patterns showing the fresh and methanol-treated Cu/Beta-deAl catalysts with different Si/Al ratios. The methanol treatment was performed at 200°C for 12 h. (C) Cu NP size distributions of various Cu/Beta-deAl catalysts before and after the methanol treatment.

Note: We studied the dealumination degree of commercial Beta zeolite (Si/Al at 13) on the Cu re-dispersion. The Beta zeolites were dealuminated with different periods or temperatures to obtain a series of Beta-deAl zeolites with Si/Al ratios at about 550, 960, 1250, and 2200 (the dealumination conditions were presented in table S6, denoted as Beta-deAl-550, -960, -1250, and -2200, respectively). FT-IR spectra of these zeolites characterizing the silanols were shown in fig. S55A, which were normalized by the intensity of the bands for Si−O−Si framework overtones appearing between 1700−2000 cm^{-1}. The parent Beta zeolite exhibited signals of isolated terminal silanols (~3740 cm^{-1}, *65*) and silanol nests (a broad band around 3500 cm^{-1}, *50*). After dealumination treatment, the contents of silanol nests increased with raising the Si/Al ratio from 13 to 550, 960, and 1250. Further dealumination to the zeolite with Si/Al ratio at 2200 led to the reduction of silanol nests and enhancement of terminal silanols, which might be due to the partial destruction of zeolite linkage by deep acid treatment for dealumination.

After loading Cu NPs on these zeolites, the diffraction of metallic Cu appeared at 43.3° and then became stronger and sharper on the Cu/Beta and Cu/Beta-deAl-550 after the methanol treatment, suggesting the Cu sintering on these zeolites (figs. S55B, C, and S56). TEM characterization showed the formation of many large Cu NPs (some of them even larger than 10 nm). The average Cu NP size of the Cu/Beta increased from 7.4 nm to 14.3 nm after the methanol treatment, and the Cu/Beta-deAl-550 showed the average size increasing from 5.0 nm to 6.5 nm, respectively (figs. S8, S55C, and S57A). For the Cu/Beta-deAl-960 and Cu/Beta-deAl-1250 samples, the Cu NPs became smaller after the methanol treatment as confirmed by the XRD

patterns with broad diffractions (fig. S55B). TEM images of the Cu/Beta-deAl-960 and Cu/Beta-deAl-1250 samples showed direct observation of the re-dispersed Cu NPs, giving the average Cu NP sizes of fresh Cu/Beta-deAl-960 and Cu/Beta-deAl-1250 at 5.7 and 5.6 nm, and then reduced to 2.8 and 2.4 nm over the treated catalysts, respectively (fig. S57B and Fig. 1A and B in the main text). These results suggest a re-dispersion process which is consistent with the findings in this manuscript. However, the Cu/Beta-deAl-2200 exhibited an opposite phenomenon, where the Cu NPs were sintered after the methanol treatment, as confirmed by both XRD and TEM characterizations (figs. S55B, C, and S57C), which should be due to the limited silanol nests with abundant terminal silanols in the Beta-deAl-2200 as observed in the FT-IR characterization (fig. S55A).

Considering that these zeolites have the same topology but distinguishable dealumination degree with various amounts of silanol nests, different trends in the change of Cu NP sizes under the methanol treatment should be reasonably attributed to the amount of silanol nests. The Cu NPs re-dispersed on the Cu/Beta-deAl-960 and Cu/Beta-deAl-1250 with abundant silanol nests, while they were sintered on the Cu/Beta, Cu/Beta-deAl-550, and Cu/Beta-deAl-2200 with limited silanol nests.

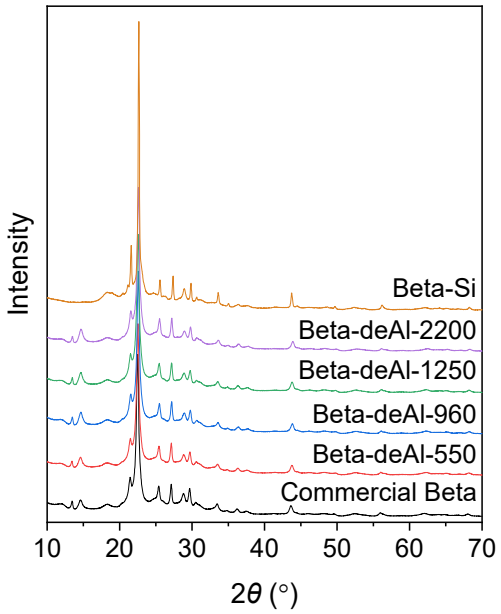

Fig. S56. XRD patterns of various Beta zeolites.

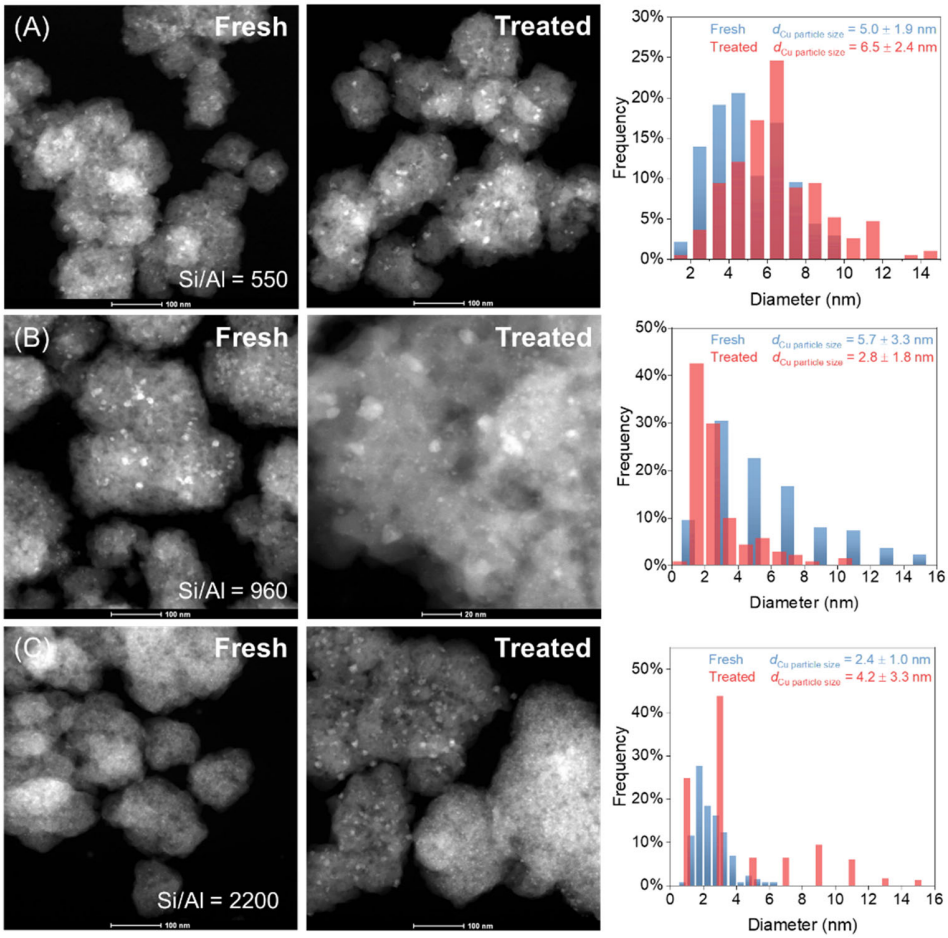

Fig. S57. STEM images and Cu NP size distributions of Cu/Beta-deAl samples with Si/Al ratios at (A) 550, (B) 960, and (C) 2200 before and after the methanol treatment at 200°C for 12 h. The STEM images of the Cu/Beta-deAl with Si/Al ratio at 1250 (the standard sample used in this work) were shown in Fig. 1A and B in the main text.

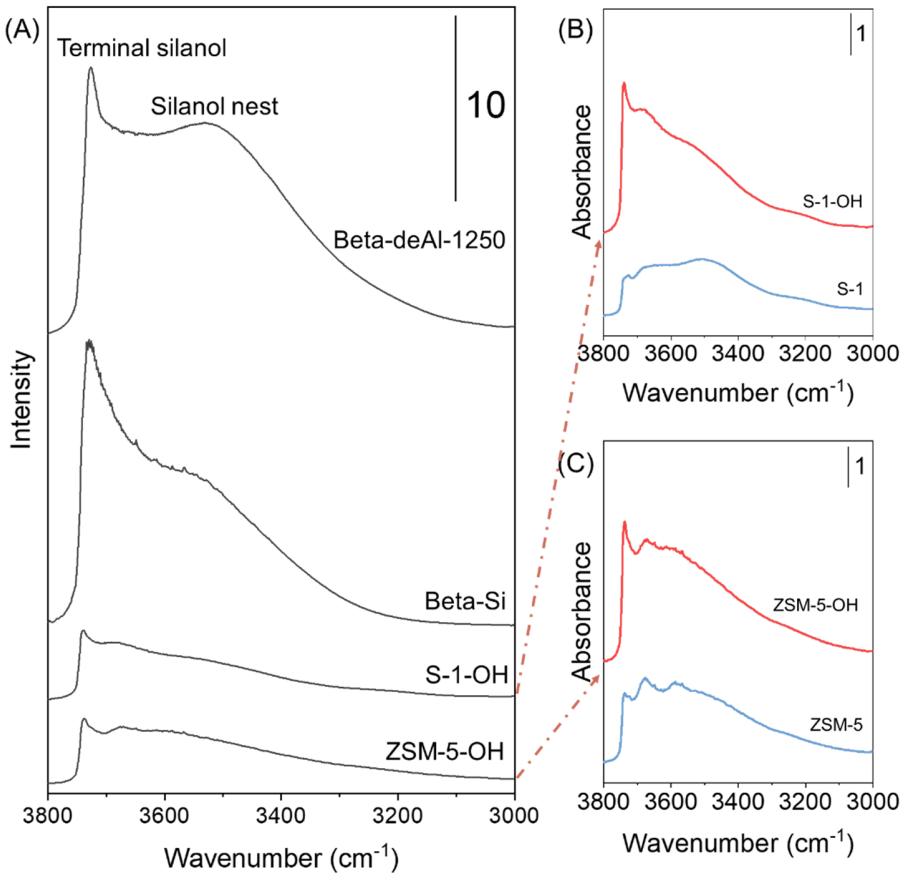

Fig. S58. (A) FT-IR charactering the silanols over different zeolites. (B) Comparison of the S-1-OH with the general S-1. (C) Comparison of the ZSM-5-OH with the general ZSM-5.

Note: All the spectra were normalized by the intensity of the bands for Si−O−Si framework overtones appearing between 1700−2000 cm^{-1}.

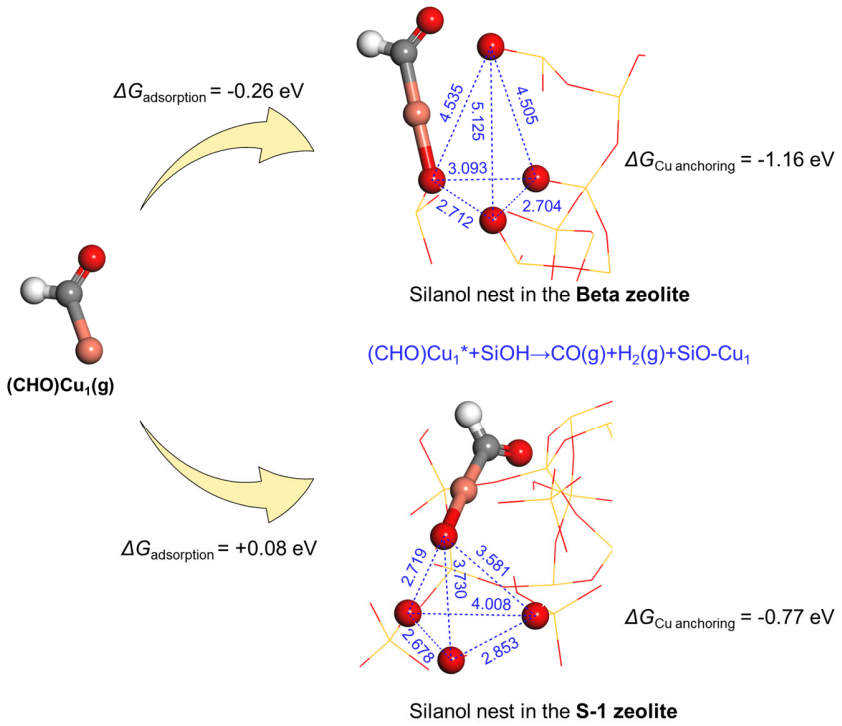

Fig. S59. Scheme showing the models, free energy change, and bond lengths (Å) of (CHO)Cu1(g) anchoring in the silanol nests of Beta and S-1 zeolites.

Note: In addition to the contents of silanol nests, we also studied the difference for trapping the (CHO)Cu1(g) intermediate between silanol nests in the Beta and those in S-1 zeolites. The free energy of (CHO)Cu1(g) adsorption on the silanol nest of S-1 was 0.08 eV, which was higher than that of -0.26 eV on the Beta zeolite. This difference might be due to the spatial difference between the nests in the S-1 and those in the Beta zeolite. When the (CHO)Cu1(g) intermediate was adsorbed, the Beta zeolite exhibited expanded silanol-silanol distance and weakened hydrogen bonds in one nest, resulting in a large space for (CHO)Cu1(g). In contrast, the silanol nest in the S-1 zeolite exhibited more spatial limitations, as supported by shorter silanol-silanol distance than that in the Beta zeolite. As a result, the whole process of Cu re-dispersion on the S-1 was endothermic but that on the Beta was exothermic, suggesting the energy favorability of this process on the Beta zeolite.

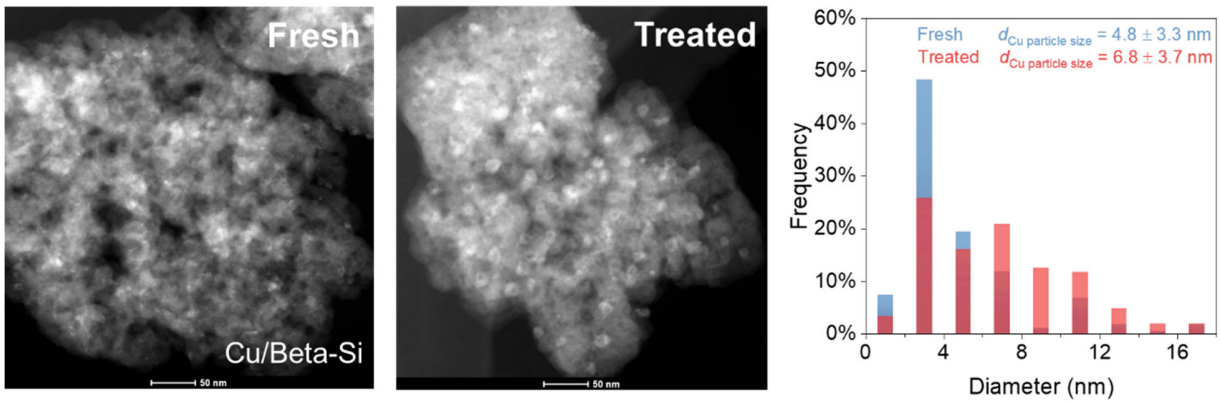

Fig. S60. STEM images of Cu/Beta-Si before and after the methanol treatment.

Note: We performed the study on siliceous Beta zeolite (Beta-Si) with abundant terminal groups rather than silanol nests (fig. S58A). The fresh and methanol-treated Cu/Beta-Si samples gave the Cu NP sizes at 4.8 nm and 6.8 nm, respectively.

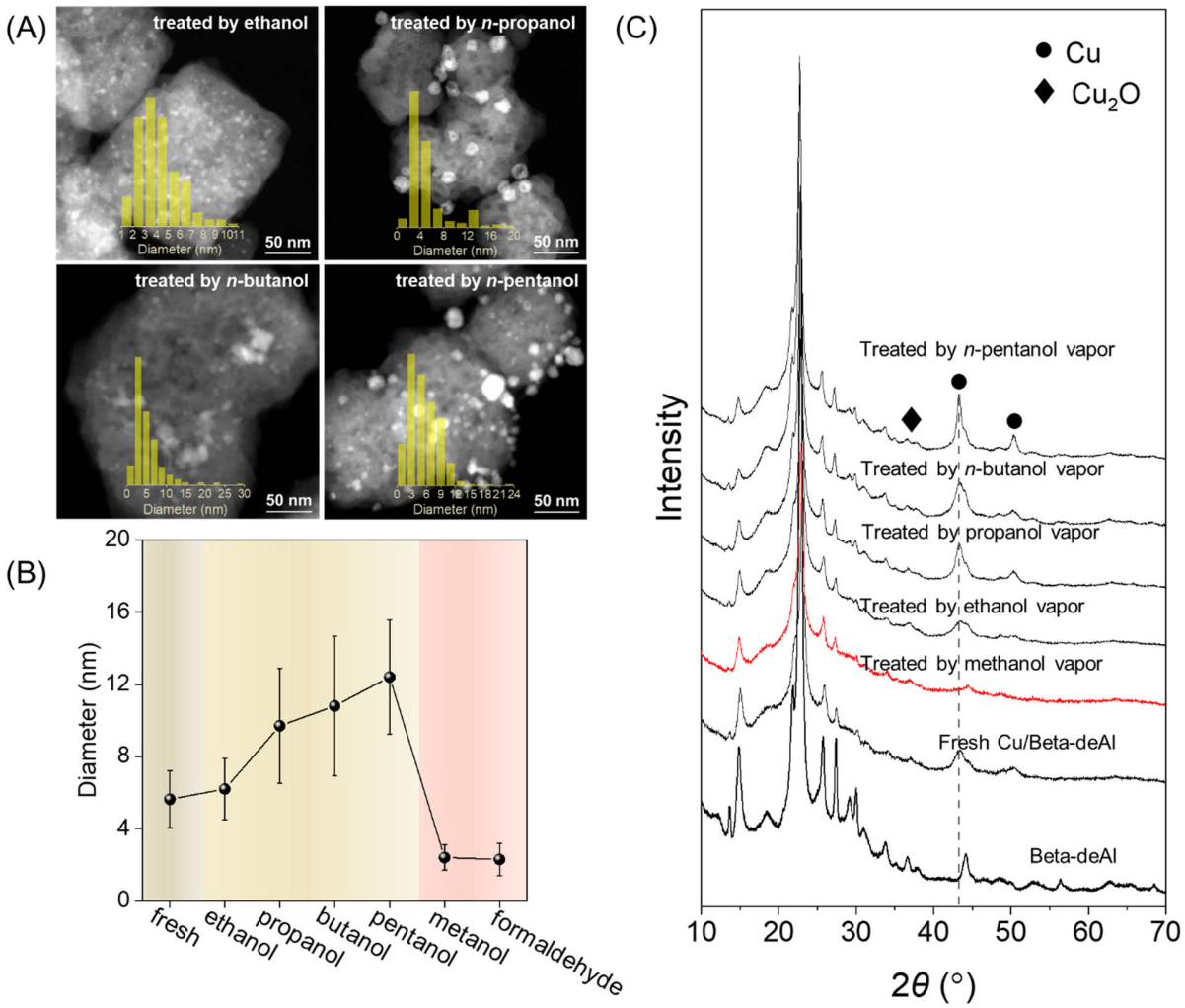

Fig. S61. (A) TEM images, (B) average Cu particle sizes, and (C) XRD patterns characterizing the Cu/Beta-deAl catalysts after treatments by different alcohols at 200°C for 12 h.

Note: Other mono-alcohols including ethanol, *n*-propanol, *n*-butanol, and *n*-pentanol were also examined under the same conditions (200°C, 12 h with the alcohol feeding rate at 0.03 mL/min). As shown in fig. S61, after treatments by ethanol, *n*-propanol, *n*-butanol, and *n*-pentanol, the Cu NPs sintered, giving the average sizes at 6.2, 9.7, 10.8, and 12.4 nm, respectively (fig. S61A and B). These results are obviously different from that using methanol or formaldehyde (Fig. 1 in the main text and fig. S61B), which was also supported by the XRD characterization (fig. S61C).

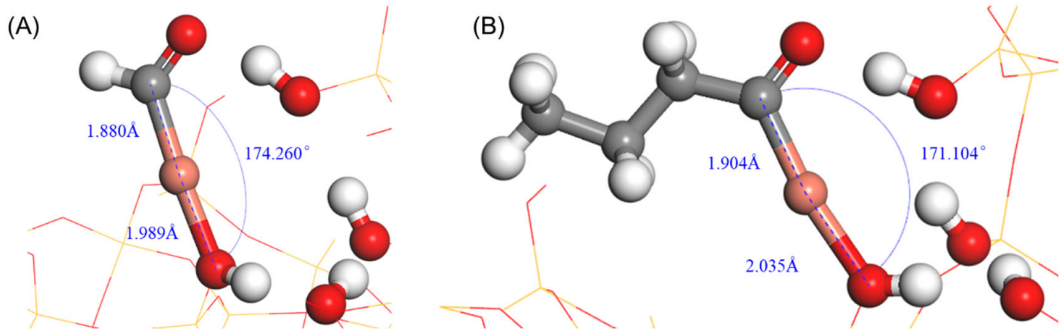

Fig. S62. The Cu-C and Cu-O bond lengths and the ∠C-Cu-O bond angle for the (A) $(CHO)Cu_1$* and (B) $(C_4H_7O)Cu_1$* intermediates adsorbed at the silanol nest.

Table S1. Data showing the performance of commercial Cu/SiO_2-C catalyst in DMO hydrogenation.

LHSV / h^{-1}	Conv. / %	Selectivity / %			
		EG	MG	Ethanol	C_2-C_4
0.6	100	56.3	1.8	30.8	11.1
1.8	100	84.9	2.3	7.5	5.3
3.0	100	91.4	5.6	1.8	1.2
3.7	85.6	70.3	28.6	0.8	0.3

Reaction conditions: 2.5 MPa, 200°C, H_2 flow rate of 15 mL/min.

Note: Under a given H_2 flow rate, EG yield was drastically increased with LHSV increasing from 0.6 to 1.8 h^{-1} due to the suppress of overreaction of EG to ethanol. Raising the LHSV to 3.0 h^{-1} resulted in the EG yield at 90.1-93.4%. Further adjusting the H_2 flow rate and reaction temperature could not improve the EG yield.

Table S2. Data showing the performance of Cu/Beta-deAl-18% catalyst in DMO hydrogenation.

LHSV / h^{-1}	*T* / °C	Conv. / %	Selectivity / %			
			EG	MG	Ethanol	C_2-C_4
1.8	200	100	96.2	0.4	1.3	2.1
3.0	220	100	95.8	0.2	1.7	2.3

Reaction conditions: 2.5 MPa, 200°C, H_2 flow rate of 30 mL/min.

Table S3. Data showing the performances of the Cu/Beta-deAl-18% in ambient-pressure DMO hydrogenation at different temperatures.

T / °C	$n(H_2)/n$(DMO)	Conv. / %	Selectivity / %			STY_{EG} / g g_{cat}^{-1} h^{-1}
			EG	MG	C_2-C_4	
190	45	35.1	36.1	62.7	1.2	-
210	45	70.8	52.9	45.6	1.5	-
230	45	>99.9	90.1	8.1	1.8	0.28

Note: By optimizing the reaction conditions, the Cu/Beta-deAl-18% gave the space-time yield at 0.28 g_{EG} g_{cat}^{-1} h^{-1}, under the full DMO conversion and 90.1% EG selectivity. This space-time yield was even comparable with that of the fullerene-modified Cu/SiO_2 catalyst (10 wt% of fullerene, 20 wt% of Cu), which has been regarded as the state-of-the-art for ambient-pressure DMO hydrogenation (*28*).

Table S4. Curve fitting parameters of Cu *K*-edge EXAFS for catalysts after reduction or methanol treatment.

Sample	Shell	[b]CN	[c]R / Å	[d]σ^2 / Å^2	[e]ΔE_0 / eV
[a]Cu foil	Cu-Cu	12	2.56	-	-
[a]Cu_2O	Cu-O	4	1.85	-	-
	Cu-Cu	8	3.70	-	-
[a]CuO	Cu-O	2	1.91	-	-
		2	1.99	-	-
	Cu-Cu	4	2.91	-	-
Cu/SiO_2 (after reduction, fresh)	Cu-O	1.4±0.2	1.86±0.02	0.003	
	Cu-Cu	3.5±0.4	2.56±0.02	0.008	8.6±2.9
	Cu-O-Cu	1.7±0.8	3.04±0.04	-	
Cu/SiO_2-treated (after reduction and methanol treatment at 300°C for 12 h)	Cu-Cu	8.2±0.3	2.51±0.01	0.008	8.2±0.3
Cu/Beta-deAl (after reduction, fresh)	Cu-Cu	9.0±0.7	2.54±0.01	0.008	4.4±2.0
Cu/Beta-deAl-treated (after reduction and methanol treatment at 300°C for 12 h)	Cu-O	1.5±0.1	1.87±0.01	0.003	
	Cu-Cu	2.3±0.3	2.56±0.01	0.008	10.0±2.4
	Cu-O-Cu	1.7±0.6	3.06±0.01	-	

S_0^2 was fixed as 0.8. [a] EXAFS data (R and CN) were calculated by FEFF code from the crystal structures. [b] The coordination numbers. [c] Average absorber-back scatterer distance. [d] Debye-Waller factor. [e] Inner potential correction.

Table S5. The reaction barrier and Gibbs free energy change of the methanol decomposition over Cu/Beta-deAl.

Reaction	*Ga / eV*	*ΔG* / eV
$CH_3OH(g)\rightarrow CH_3OH^*$		0.40
$CH_3OH^*\rightarrow CH_3O^*+H^*$	0.90	-0.48
$CH_3O^*\rightarrow HCHO^*+H^*$	0.86	0.17
$HCHO^*\rightarrow *CHO+H^*$	0.83	-0.46
$*CHO\rightarrow *CO+H^*$	0.41	-0.98
$CH_3OH(g)\rightarrow *CH_2OH+H^*$	2.16	0.46
$*CH_2OH\rightarrow *CHOH+H^*$	0.95	0.36
$*CHOH\rightarrow *CHO+H^*$	0.28	-1.20
$H^*+H^*\rightarrow H_2(g)$	0.91	0.59

Table S6. The dealumination conditions for the synthesis of Beta-deAl zeolites with different dealumination degree.

Sample	*T* / °C	*t* / h	Si/Al ratio (by ICP)
Commercial Beta	-	-	13
Beta-deAl-550	80	3	550
Beta-deAl-960	80	6	960
Beta-deAl-1250	80	12	1250
Beta-deAl-2200	100	24	2200

Note: The Beta-deAl employed in this work was Si/Al ratio at 1250 unless noted.

Table S7. The adsorption energy (E_{ads}) of the Cu_1 atom on different sites.

Adsorption type	E_{ads} / eV
Cu_1 on Cu_4 (with silanol nests)	-2.80
Cu_1 on Cu_{55} (with silanol nests)	-2.96
Cu_1 on Cu_{73} (with silanol nests)	-2.60
Cu_1 on Cu_{55} (without silanol nests)	-2.40
Cu_1 on large Cu particles	-2.22

"Cu_1 on Cu_x (with silanol nests/without silanol nests)" means the adsorption energy of Cu_1 atom on the Cu_x cluster at the silanol nests or general Cu_x cluster without silanol nests. The more negative value of the E_{ads} suggests the stronger adsorption strength. Large Cu particles refer to the Cu(111) surface as a model to simulate the extended surface of the large Cu particles.

Note: We have conducted computational studies to investigate the adsorption energies of Cu_1 intermediate on the Cu_{55} cluster with and without the silanol nests. As shown in table S7, the adsorption energy of Cu_1 on the Cu_{55} cluster at the silanol nests (-2.96 eV) is more exothermic than that without silanol nests (-2.40 eV). This is reasonably attributed to the strong Cu-O bonding and steric hindrance in the silanol nests. Accordingly, it limits structural relaxation and consequently leads to the formation of more defects on the Cu_{55} clusters at the silanol nests, which contributes to a stronger adsorption of Cu_1 intermediate.

In addition, it is reasonably imagined that the Cu-O bonding gradually diminishes with the increasing size of the Cu nanostructures. For example, the adsorption energy of Cu_1 on the Cu_{73} cluster at the silanol nests is -2.60 eV (table S7), weaker than that on Cu_{55} at the silanol nest. With raising the Cu nanostructure size at the silanol nests, their adsorption energy to Cu_1 atoms tends to be similar to that of the bulky Cu surface. In other word, the Cu_1 intermediate has equal probability to be captured by an adjacent Cu NP at silanol nest and bulky Cu particle. However, it is worth noting that a great number of silanol nests in Beta-deAl zeolite enables numerous small Cu NPs to be stabilized. These silanol nests have significant advantage to capture the Cu_1 intermediates in competition with the limited amount of large Cu particles. Therefore, this feature reasonably leads to the re-dispersion of Cu particles rather than the Cu sintering. To further support this hypothesis, we reduced the silanol concentration on Beta-deAl by controlling the dealumination degree, and those Beta-deAl supports with less amounts of silanol nests failed to re-disperse Cu NPs (fig. S61 in the Supplementary Materials).

Table S8. The free energy in the reverse Ostwald ripening process on Cu/Beta-deAl under methanol and *n*-butanol atmosphere.

Treatment atmosphere	$\Delta G_{adsorption}$ / eV	$\Delta G_{(RCO)Cu1*}$ / eV	$\Delta G_{(RCO)Cu1*\ migration\ to\ silanol\ nest}$ / eV	$\Delta G_{Cu1\ anchoring\ in\ the\ silanol\ nest}$ / eV
methanol	0.40	-0.77	0.42	-1.16
n-butanol	0.48	-0.62	0.58	-0.34

Note: RCO* (on Cu_{13} cluster) from methanol and *n*-butanol. R = H and C_3H_7, respectively.

References and Notes

1. B. C. Gates, Supported metal clusters: Synthesis, structure, and catalysis. *Chem. Rev.* **95**, 511–522 (1995). doi:10.1021/cr00035a003

2. P. Munnik, P. E. de Jongh, K. P. de Jong, Recent developments in the synthesis of supported catalysts. *Chem. Rev.* **115**, 6687–6718 (2015). doi:10.1021/cr500486u Medline

3. C. Mondelli, G. Gözaydın, N. Yan, J. Pérez-Ramírez, Biomass valorisation over metal-based solid catalysts from nanoparticles to single atoms. *Chem. Soc. Rev.* **49**, 3764–3782 (2020). doi:10.1039/D0CS00130A Medline

4. A. T. Bell, The impact of nanoscience on heterogeneous catalysis. *Science* **299**, 1688–1691 (2003). doi:10.1126/science.1083671 Medline

5. X. Li, X. I. Pereira-Hernández, Y. Chen, J. Xu, J. Zhao, C. W. Pao, C. Y. Fang, J. Zeng, Y. Wang, B. C. Gates, J. Liu, Functional CeO_x nanoglues for robust atomically dispersed catalysts. *Nature* **611**, 284–288 (2022). doi:10.1038/s41586-022-05251-6 Medline

6. E. V. Makshina, M. Dusselier, W. Janssens, J. Degrève, P. A. Jacobs, B. F. Sels, Review of old chemistry and new catalytic advances in the on-purpose synthesis of butadiene. *Chem. Soc. Rev.* **43**, 7917–7953 (2014). doi:10.1039/C4CS00105B Medline

7. M. B. Gawande, A. Goswami, F.-X. Felpin, T. Asefa, X. Huang, R. Silva, X. Zou, R. Zboril, R. S. Varma, Cu and Cu-based nanoparticles: Synthesis and applications in catalysis. *Chem. Rev.* **116**, 3722–3811 (2016). doi:10.1021/acs.chemrev.5b00482 Medline

8. S. Hu, W.-X. Li, Sabatier principle of metal-support interaction for design of ultrastable metal nanocatalysts. *Science* **374**, 1360–1365 (2021). doi:10.1126/science.abi9828 Medline

9. J. Jones, H. Xiong, A. T. DeLaRiva, E. J. Peterson, H. Pham, S. R. Challa, G. Qi, S. Oh, M. H. Wiebenga, X. I. Pereira Hernández, Y. Wang, A. K. Datye, Thermally stable single-atom platinum-on-ceria catalysts via atom trapping. *Science* **353**, 150–154 (2016). doi:10.1126/science.aaf8800 Medline

10. J. C. Matsubu, S. Zhang, L. DeRita, N. S. Marinkovic, J. G. Chen, G. W. Graham, X. Pan, P. Christopher, Adsorbate-mediated strong metal-support interactions in oxide-supported Rh catalysts. *Nat. Chem.* **9**, 120–127 (2017). doi:10.1038/nchem.2607 Medline

11. T. W. van Deelen, C. Hernández Mejía, K. P. de Jong, Control of metal-support interactions in heterogeneous catalysts to enhance activity and selectivity. *Nat. Catal.* **2**, 955–970 (2019). doi:10.1038/s41929-019-0364-x

12. Z. Li, Y. Cui, Z. Wu, C. Milligan, L. Zhou, G. Mitchell, B. Xu, E. Shi, J. T. Miller, F. H. Ribeiro, Y. Wu, Reactive metal–support interactions at moderate temperature in two-dimensional niobium-carbide-supported platinum catalysts. *Nat. Catal.* **1**, 349–355 (2018). doi:10.1038/s41929-018-0067-8

13. M. D. Argyle, C. H. Bartholomew, Heterogeneous catalyst deactivation and regeneration: A review. *Catalysts* **5**, 145–269 (2015). doi:10.3390/catal5010145

14. X. Jiang, X. Nie, X. Guo, C. Song, J. G. Chen, Recent advances in carbon dioxide hydrogenation to methanol via heterogeneous catalysis. *Chem. Rev.* **120**, 7984–8034 (2020). doi:10.1021/acs.chemrev.9b00723 Medline

15. W. Zhou, K. Cheng, J. Kang, C. Zhou, V. Subramanian, Q. Zhang, Y. Wang, New horizon in C1 chemistry: Breaking the selectivity limitation in transformation of syngas and hydrogenation of CO_2 into hydrocarbon chemicals and fuels. *Chem. Soc. Rev.* **48**, 3193–3228 (2019). doi:10.1039/C8CS00502H Medline

16. D. Li, F. Xu, X. Tang, S. Dai, T. Pu, X. Liu, P. Tian, F. Xuan, Z. Xu, I. E. Wachs, M. Zhu, Induced activation of the commercial $Cu/ZnO/Al_2O_3$ catalyst for the steam reforming of methanol. *Nat. Catal.* **5**, 99–108 (2022). doi:10.1038/s41929-021-00729-4

17. D. R. Palo, R. A. Dagle, J. D. Holladay, Methanol steam reforming for hydrogen production. *Chem. Rev.* **107**, 3992–4021 (2007). doi:10.1021/cr050198b Medline

18. P. Wynblatt, N. A. Gjostein, Particle growth in model supported metal catalysts—I. Theory. *Acta Metall.* **24**, 1165–1174 (1976). doi:10.1016/0001-6160(76)90034-1

19. S. C. Parker, C. T. Campbell, Kinetic model for sintering of supported metal particles with improved size-dependent energetics and applications to Au on TiO_2(110). *Phys. Rev. B* **75**, 035430 (2007). doi:10.1103/PhysRevB.75.035430

20. R. van den Berg, T. E. Parmentier, C. F. Elkjær, C. J. Gommes, J. Sehested, S. Helveg, P. E. de Jongh, K. P. de Jong, Support functionalization to retard Ostwald ripening in copper methanol synthesis catalysts. *ACS Catal.* **5**, 4439–4448 (2015). doi:10.1021/acscatal.5b00833

21. D. Yao, Y. Wang, Y. Li, A. Li, Z. Zhen, J. Lv, F. Sun, R. Yang, J. Luo, Z. Jiang, Y. Wang, X. Ma, Scalable synthesis of Cu clusters for remarkable selectivity control of intermediates in consecutive hydrogenation. *Nat. Commun.* **14**, 1123 (2023). doi:10.1038/s41467-023-36640-8 Medline

22. S. Feng, X. Song, Y. Liu, X. Lin, L. Yan, S. Liu, W. Dong, X. Yang, Z. Jiang, Y. Ding, In situ formation of mononuclear complexes by reaction-induced atomic dispersion of supported noble metal nanoparticles. *Nat. Commun.* **10**, 5281 (2019). doi:10.1038/s41467-019-12965-1 Medline

23. S. Chen, X. Chang, G. Sun, T. Zhang, Y. Xu, Y. Wang, C. Pei, J. Gong, Propane dehydrogenation: Catalyst development, new chemistry, and emerging technologies. *Chem. Soc. Rev.* **50**, 3315–3354 (2021). doi:10.1039/D0CS00814A Medline

24. A. Bishara, K. M. Murad, A. Stanislaus, M. Ismial, S. S. Hussian, Factors controlling the sintering of an industrial bimetallic reforming catalyst during regeneration. *Appl. Catal.* **7**, 351–359 (1983). doi:10.1016/0166-9834(83)80034-7

25. Y. Nishihata, J. Mizuki, T. Akao, H. Tanaka, M. Uenishi, M. Kimura, T. Okamoto, N. Hamada, Self-regeneration of a Pd-perovskite catalyst for automotive emissions control. *Nature* **418**, 164–167 (2002). doi:10.1038/nature00893 Medline

26. N. Felvey, J. Guo, R. Rana, L. Xu, S. R. Bare, B. C. Gates, A. Katz, A. R. Kulkarni, R. C. Runnebaum, C. X. Kronawitter, Interconversion of atomically dispersed platinum cations and platinum clusters in zeolite ZSM-5 and formation of platinum *gem*-dicarbonyls. *J. Am. Chem. Soc.* **144**, 13874–13887 (2022). doi:10.1021/jacs.2c05386 Medline

27. H. Li, Y. Shen, X. Xiao, H. Jiang, Q. Gu, Y. Zhang, L. Lin, W. Luo, S. Zhou, J. Zhao, A. Wang, T. Zhang, B. Yang, Controlled-release mechanism regulates rhodium migration

and size redistribution boosting catalytic methane conversion. *ACS Catal.* **13**, 1197–1206 (2023). doi:10.1021/acscatal.2c05463

28. J. Zheng, L. Huang, C.-H. Cui, Z.-C. Chen, X.-F. Liu, X. Duan, X.-Y. Cao, T.-Z. Yang, H. Zhu, K. Shi, P. Du, S.-W. Ying, C.-F. Zhu, Y.-G. Yao, G.-C. Guo, Y. Yuan, S.-Y. Xie, L.-S. Zheng, Ambient-pressure synthesis of ethylene glycol catalyzed by C_{60}-buffered Cu/SiO_2. *Science* **376**, 288–292 (2022). doi:10.1126/science.abm9257 Medline

29. J. Gong, H. Yue, Y. Zhao, S. Zhao, L. Zhao, J. Lv, S. Wang, X. Ma, Synthesis of ethanol via syngas on Cu/SiO_2 catalysts with balanced Cu^0-Cu^+ sites. *J. Am. Chem. Soc.* **134**, 13922–13925 (2012). doi:10.1021/ja3034153 Medline

30. J. Lin, X. Zhao, Y. Cui, H. Zhang, D. Liao, Effect of feedstock solvent on the stability of Cu/SiO_2 catalyst for vapor-phase hydrogenation of dimethyl oxalate to ethylene glycol. *Chem. Commun.* **48**, 1177–1179 (2012). doi:10.1039/C1CC15783C Medline

31. C. Xu, G. Chen, Y. Zhao, P. Liu, X. Duan, L. Gu, G. Fu, Y. Yuan, N. Zheng, Interfacing with silica boosts the catalysis of copper. *Nat. Commun.* **9**, 3367 (2018). doi:10.1038/s41467-018-05757-6 Medline

32. J. Sun, J. Yu, Q. Ma, F. Meng, X. Wei, Y. Sun, N. Tsubaki, Freezing copper as a noble metal-like catalyst for preliminary hydrogenation. *Sci. Adv.* **4**, eaau3275 (2018). doi:10.1126/sciadv.aau3275 Medline

33. H. Yue, Y. Zhao, L. Zhao, J. Lv, S. Wang, J. Gong, X. Ma, Hydrogenation of dimethyl oxalate to ethylene glycol on a Cu/SiO_2/cordierite monolithic catalyst: Enhanced internal mass transfer and stability. *AIChE J.* **58**, 2798–2809 (2012). doi:10.1002/aic.12785

34. J. Zheng, J. Zhou, H. Lin, X. Duan, C. T. Williams, Y. Yuan, CO-mediated deactivation mechanism of SiO_2-supported copper catalysts during dimethyl oxalate hydrogenation to ethylene glycol. *J. Phys. Chem. C Nanomater. Interfaces* **119**, 13758–13766 (2015). doi:10.1021/acs.jpcc.5b03569

35. C.-S. Chen, W.-H. Cheng, S.-S. Lin, Enhanced activity and stability of a Cu/SiO_2 catalyst for the reverse water gas shift reaction by an iron promoter. *Chem. Commun.* **2001**, 1770–1771 (2001). doi:10.1039/b104279n Medline

36. Z. Gao, B. Ma, S. Chen, J. Tian, C. Zhao, Converting waste PET plastics into automobile fuels and antifreeze components. *Nat. Commun.* **13**, 3343 (2022). doi:10.1038/s41467-022-31078-w Medline

37. C. Wen, Y. Cui, W.-L. Dai, S. Xie, K. Fan, Solvent feedstock effect: The insights into the deactivation mechanism of Cu/SiO_2 catalysts for hydrogenation of dimethyl oxalate to ethylene glycol. *Chem. Commun.* **49**, 5195–5197 (2013). doi:10.1039/c3cc40570b Medline

38. S. Qing, X. Hou, L. Li, G. Feng, X. Wang, Z. Gao, W. Fan, Deactivation feature of Cu/SiO_2 catalyst in methanol decomposition. *Int. J. Hydrogen Energy* **44**, 16667–16674 (2019). doi:10.1016/j.ijhydene.2019.03.160

39. C. D. Chang, A. J. Silvestri, The conversion of methanol and other O-compounds to hydrocarbons over zeolite catalysts. *J. Catal.* **47**, 249–259 (1977). doi:10.1016/0021-9517(77)90172-5

40. Z. Liu, J. Liang, Methanol to olefin conversion catalysts. *Curr. Opin. Solid State Mater. Sci.* **4**, 80–84 (1999). doi:10.1016/S1359-0286(99)80015-1

41. S. Lin, Y. Zhi, W. Chen, H. Li, W. Zhang, C. Lou, X. Wu, S. Zeng, S. Xu, J. Xiao, A. Zheng, Y. Wei, Z. Liu, Molecular routes of dynamic autocatalysis for methanol-to-hydrocarbons reaction. *J. Am. Chem. Soc.* **143**, 12038–12052 (2021). doi:10.1021/jacs.1c03475 Medline

42. B. Eren, D. Zherebetskyy, L. L. Patera, C. H. Wu, H. Bluhm, C. Africh, L. W. Wang, G. A. Somorjai, M. Salmeron, Activation of Cu(111) surface by decomposition into nanoclusters driven by CO adsorption. *Science* **351**, 475–478 (2016). doi:10.1126/science.aad8868 Medline

43. R.-P. Ye, L. Lin, L.-C. Wang, D. Ding, Z. Zhou, P. Pan, Z. Xu, J. Liu, H. Adidharma, M. Radosz, M. Fan, Y.-G. Yao, Perspectives on the active sites and catalyst design for the hydrogenation of dimethyl oxalate. *ACS Catal.* **10**, 4465–4490 (2020). doi:10.1021/acscatal.9b05477

44. K. Ma, Y. Tian, Z.-J. Zhao, Q. Cheng, T. Ding, J. Zhang, L. Zheng, Z. Jiang, T. Abe, N. Tsubaki, J. Gong, X. Li, Achieving efficient and robust catalytic reforming on dual-sites of Cu species. *Chem. Sci.* **10**, 2578–2584 (2019). doi:10.1039/C9SC00015A Medline

45. R. Ouyang, J.-X. Liu, W.-X. Li, Atomistic theory of Ostwald ripening and disintegration of supported metal particles under reaction conditions. *J. Am. Chem. Soc.* **135**, 1760–1771 (2013). doi:10.1021/ja3087054 Medline

46. Q. Wan, F. Wei, Y. Wang, F. Wang, L. Zhou, S. Lin, D. Xie, H. Guo, Single atom detachment from Cu clusters, and diffusion and trapping on CeO_2(111): Implications in Ostwald ripening and atomic redispersion. *Nanoscale* **10**, 17893–17901 (2018). doi:10.1039/C8NR06232C Medline

47. T. W. Hansen, A. T. Delariva, S. R. Challa, A. K. Datye, Sintering of catalytic nanoparticles: Particle migration or Ostwald ripening? *Acc. Chem. Res.* **46**, 1720–1730 (2013). doi:10.1021/ar3002427 Medline

48. Y. X. Zhao, Z. Y. Li, Z. Yuan, X. N. Li, S. G. He, Thermal methane conversion to formaldehyde promoted by single platinum atoms in $PtAl_2O_4^-$ cluster anions. *Angew. Chem. Int. Ed.* **53**, 9482–9486 (2014). doi:10.1002/anie.201403953 Medline

49. Z. Yuan, Z. Li, Z. Zhou, Q. Liu, Y. Zhao, S. He, Thermal reactions of $(V_2O_5)_nO^-$ (n=1−3) cluster anions with ethylene and propylene: Oxygen atom transfer versus molecular association. anions. *J. Phys. Chem. C Nanomater. Interfaces* **118**, 14967–14976 (2014). doi:10.1021/jp5040344

50. L. Qi, M. Babucci, Y. Zhang, A. Lund, L. Liu, J. Li, Y. Chen, A. S. Hoffman, S. R. Bare, Y. Han, B. C. Gates, A. T. Bell, Propane dehydrogenation catalyzed by isolated Pt atoms in ≡SiOZn–OH nests in dealuminated zeolite Beta. *J. Am. Chem. Soc.* **143**, 21364–21378 (2021). doi:10.1021/jacs.1c10261 Medline

51. G. Busca, Acid catalysts in industrial hydrocarbon chemistry. *Chem. Rev.* **107**, 5366–5410 (2007). doi:10.1021/cr068042e Medline

52. Y. Liu, Z. Liu, Y. Hui, L. Wang, J. Zhang, X. Yi, W. Chen, C. Wang, H. Wang, Y. Qin, L. Song, A. Zheng, F.-S. Xiao, Rhodium nanoparticles supported on silanol-rich zeolites

beyond the homogeneous Wilkinson's catalyst for hydroformylation of olefins. *Nat. Commun.* **14**, 2531 (2023). doi:10.1038/s41467-023-38181-6 Medline

53. Q. Wu, X. Meng, X. Gao, F.-S. Xiao, Solvent-free synthesis of zeolites: Mechanism and utility. *Acc. Chem. Res.* **51**, 1396–1403 (2018). doi:10.1021/acs.accounts.8b00057 Medline

54. G. Kresse, J. Furthmüller, Efficiency of ab-initio total energy calculations for metals and semiconductors using a plane-wave basis set. *Comput. Mater. Sci.* **6**, 15–50 (1996). doi:10.1016/0927-0256(96)00008-0

55. G. Kresse, J. Furthmüller, Efficient iterative schemes for ab initio total-energy calculations using a plane-wave basis set. *Phys. Rev. B* **54**, 11169–11186 (1996). doi:10.1103/PhysRevB.54.11169 Medline

56. I. Bönicke, W. Kirstein, S. Spinzig, F. Thieme, CO adsorption studies on a stepped Cu(111) surface. *Surf. Sci.* **313**, 231–238 (1994). doi:10.1016/0039-6028(94)90044-2

57. A. Alavi, P. Hu, T. Deutsch, P. L. Silvestrelli, J. Hutter, CO oxidation on Pt(111): An ab initio density functional theory study. *Phys. Rev. Lett.* **80**, 3650–3653 (1998). doi:10.1103/PhysRevLett.80.3650

58. Y. Lou, Y. Cai, W. Hu, L. Wang, Q. Dai, W. Zhan, Y. Guo, P. Hu, X.-M. Cao, J. Liu, Y. Guo, Identification of active area as active center for CO oxidation over single Au atom catalyst. *ACS Catal.* **10**, 6094–6101 (2020). doi:10.1021/acscatal.0c01303

59. F. Studt, F. Abild-Pedersen, J. B. Varley, J. K. Nørskov, CO and CO_2 hydrogenation to methanol calculated using the BEEF-vdW functional. *Catal. Lett.* **143**, 71–73 (2013). doi:10.1007/s10562-012-0947-5

60. R. Dronskowski, P. E. Bloechl, Crystal orbital Hamilton populations (COHP): Energy-resolved visualization of chemical bonding in solids based on density-functional calculations. *J. Phys. Chem.* **97**, 8617–8624 (1993). doi:10.1021/j100135a014

61. V. L. Deringer, A. L. Tchougréeff, R. Dronskowski, Crystal orbital Hamilton population (COHP) analysis as projected from plane-wave basis sets. *J. Phys. Chem. A* **115**, 5461–5466 (2011). doi:10.1021/jp202489s Medline

62. S. Maintz, V. L. Deringer, A. L. Tchougréeff, R. Dronskowski, LOBSTER: A tool to extract chemical bonding from plane-wave based DFT. *J. Comput. Chem.* **37**, 1030–1035 (2016). doi:10.1002/jcc.24300 Medline

63. D. B. Clarke, D. K. Lee, M. J. Sandoval, A. T. Bell, Infrared studies of the mechanism of methanol decomposition on Cu/SiO_2. *J. Catal.* **150**, 81–93 (1994). doi:10.1006/jcat.1994.1324

64. S. Porter, A. Ghosh, C. H. Liu, D. Kunwar, C. Thompson, R. Alcala, D. P. Dean, J. T. Miller, A. DeLaRiva, H. Pham, E. Peterson, A. Brearley, J. Watt, E. A. Kyriakidou, A. K. Datye, Biphasic Janus particles explain self-healing in Pt–Pd diesel oxidation catalysts. *ACS Catal.* **13**, 5456–5471 (2023). doi:10.1021/acscatal.3c00360

65. B. Tang, W. Dai, X. Sun, N. Guan, L. Li, M. Hunger, A procedure for the preparation of Ti-Beta zeolites for catalytic epoxidation with hydrogen peroxide. *Green Chem.* **16**, 2281–2291 (2014). doi:10.1039/C3GC42534G